STUDY OF EARTHQUAKE FAULT ZONE STRUCTURES BY AFTERSHOCK LOCATION AND HIGH-FREQUENCY WAVEFORM MODELING

Hongfeng Yang, M.S.

An Abstract Presented to the Graduate Faculty of
Saint Louis University in Partial Fulfillment
of the Requirements for the Degree of
Doctor of Philosophy

2010

Abstract

In this study, I analyzed high frequency waveforms of local earthquakes to map crustal faults and to investigate fine structures of fault zone (FZ). In order to determine the fault plane of the 18 April 2008 Illinois earthquake, I first developed a sliding-window cross-correlation (SCC) detection technique and applied the technique to continuous waveforms recorded by the Cooperative New Madrid Seismic Network stations. The technique detected more than 120 aftershocks down to ML 1.0 in the 2 week time window following the mainshock, which is three times more than the number of aftershocks reported by the seismic network. Most aftershocks happened within 24 hrs of the mainshock. I then relocated all events by the double-difference relocation algorithm. Accurate P- and S-wave differential arrival times between events were obtained by waveform cross correlation. After relocation, I used the L1 norm to fit all located events by a plane to determine the mainshock fault plane. The best-fit plane has a strike of $292^\circ \pm 11^\circ$ and dips $81^\circ \pm 11^\circ$ to the northeast. This plane agrees well with the focal mechanism solutions of the mainshock and four largest aftershocks. By combining the aftershock locations and focal mechanism solutions, I concluded that the 18 April earthquake occurred on a nearly vertical left-lateral strike-slip fault orienting in the west-northwest-east-southeast direction. The fault coincides with the proposed left-stepping Divide accommodation zone in the La Salle deformation belt and indicates reactivation of old deformation zone by contemporary stresses in the Midcontinent.

To investigate fine structures of the San Jacinto fault zone and the Calico fault zone in southern California, I used P- and S-wave travel times and waveforms of local earthquakes recorded by temporary arrays across the faults. In the San Jacinto fault zone study, I developed a method to determine the depth extent of the

low-velocity zone (LVZ) associated with a FZ using S-wave precursors. The precursors are diffracted S waves around the edges of LVZ and their relative amplitudes to the direct S waves are sensitive to LVZ depth. I applied the method to data recorded by three temporary arrays across three branches of the San Jacinto fault zone. The FZ dip was constrained by differential travel times of P waves between stations at two side of the FZ. Other FZ parameters (width and velocity contrast) were determined by modelling waveforms of direct and FZ-reflected P and S waves. I found that the LVZ of the Buck Ridge fault branch has a width of $\sim$150 m with a 30–40 per cent reduction in V_p and a 50–60 per cent reduction in V_s. The fault dips 70° to southwest and its LVZ extends only to 2$\pm$1 km in depth. The LVZ of the Clark Valley fault branch has a width of $\sim$200 m with 40 per cent reduction in V_p and 50 per cent reduction in V_s. The Coyote Creek branch is nearly vertical and has a LVZ of $\sim$150 m in width and of 25 per cent reduction in V_p and 50 per cent reduction in V_s. The LVZs of these three branches are not centred at the surface fault trace but are located to their northeast, indicating asymmetric damage during earthquakes.

In the Calico fault zone study, I performed a systematic analysis of travel times from earthquakes located on the northeastern and southwestern sides of the fault. The FZ width and velocity contrast were determined by modeling waveforms of direct and FZ-reflected waves. The FZ dip was constrained by arrival times of earthquakes from both sides of the Calico fault. Arrival time advances at southwestern stations for two northeastern events were used to constrain the LVZ depth. I found a 1.3-km-wide LVZ with 40 per cent reduction in V_p and 50 per cent reduction in V_s of the Calico fault. The fault dips 70° to northeast and its LVZ extends only to $\sim$4 km in depth. The LVZ is not centred at the surface fault trace, but is shifted to southwest.

STUDY OF EARTHQUAKE FAULT ZONE STRUCTURES BY AFTERSHOCK LOCATION AND HIGH-FREQUENCY WAVEFORM MODELING

Hongfeng Yang, M.S.

A Dissertation Presented to the Graduate Faculty of
Saint Louis University in Partial Fulfillment
of the Requirements for the Degree of
Doctor of Philosophy

2010

© Copyright by
Hongfeng Yang
ALL RIGHTS RESERVED

2010

COMMITTEE IN CHARGE OF CANDIDACY:
Associate Professor Lupei Zhu, Chairperson and Advisor

Professor Robert B. Herrmann

Associate Professor Keith D. Koper

Dedication

This dissertation is dedicated to my parents, Mingshen Yang and Xiujuan Liu, and my wife, Aihua Yan.

Acknowledgments

First, I must gratefully and sincerely thank my academic advisor, Dr. Lupei Zhu, for his generous help and guidance during my study at Saint Louis University. It is him who has supported and supervised me for nearly five years. He guides me into the world of seismology and inspires me to do scientific research. I learned a lot from him such as skills of programming, tons of Linux commands, style of scientific writing, and so on. Without his help, I could not finish the dissertation and get my work published. In addition, he is not only a perfect advisor on research but also a nice friend in daily life.

I also thank my committee members, Dr. Robert B. Herrmann and Dr. Keith Koper for their careful review and valuable comments on my dissertation. I like to point out that Dr. Herrmann is the person who taught me Linux commands from the very beginning that helped me to start research in seismology. Dr. Herrmann is also the person who answered lots of questions for me in different fields, e.g. Google Earth, Linux trick, and even fax machine. I enjoy collaborations with Dr. Koper in a few class projects and appreciate his help in my paper and dissertation preparations. I benefited a lot from discussions with Dr. John Encarnación from general geology questions to my specific scientific work, either in office or in bar. I must mention that the wonderful scientific departmental field trips, in which a lot of students learned field geology and got to know other people, were almost always leaded by John and Dr. David Kirschner, who explained geology, took care of every student, and slept on the floor (unless there were available beds) in order to let students have a good sleep. I also thank other faculty members of the Department of Earth and Atmospheric Sciences, especially Dr. David J. Crossley, Dr. Brian J. Mitchell, and Dr. Zaitao Pan. A special thank goes to Dr. William Dannevik, our department chair, who always supports us in sharing costs of attending conferences

and intramural games. All the faculty members in the department have taught me the necessary knowledge in seismology, geophysics, and geology. Without them, I could not have reached this achievement.

I cannot forget the department staff, Eric J. Haug, Bob Wurth, Cynthia Wise, and Laurie Hausmann. They gave me much help on technical issues, traveling, and course registration. Moreover, I would give special thank to Cynthia Wise for her proof reading on my meeting presentations. I also thank Melanie Whittington who provided me the opportunity to archive data for IRIS.

I am grateful to Dr. Yehuda Ben-Zion and Dr. Frank Vernon for their offering the San Jacinto fault zone waveform data, and to Dr. Elizabeth Cochran for providing the Calico fault zone data. I benefit from discussions with Dr. Yehuda Ben-Zion of the rupture propagation and damage zone and thank him for answering my questions. The work in this dissertation has been supported by the U.S. National Science Foundation under grant no. EAR-0609969.

I give my gratitude to Risheng Chu, Yanlai Xu, and Ying Ye for their help when I first came to the United States. I thank here my classmates, Hongyi Li, Felipe Leyton, Ali Fatahi, Youngsoo Jean, and Zuihong Zou, and all graduate students of the EAS department for their friendship during these years. I also want to say "thank you" to my intramural soccer teammates for our wonderful times in the games.

I really appreciate the continuous support and encouragement from my parents throughout my education. In the end I would thank my beloved wife Aihua Yan for her love, sacrifices, and kindness.

Table of Contents

List of Tables

List of Figures

Chapter 1: Introduction

A crustal fault is a fracture or zone of fractures that separates different blocks of crust and accumulates aseismic strain subjected to large stress concentrations. When the energy associated with the accumulated strain is suddenly released, an earthquake occurs on the fault. Therefore, mapping faults and studying fault zone material properties are important for seismic hazard analysis and for understanding earthquake physics.

Studies of faults exposed on the surface indicate that a fault is usually not a simple plane but is characterized as a narrow zone of intense damage and deformation. The zone has a finite width and is called a fault zone (FZ). A FZ usually includes a fault core (tens of centimeters to several meters in width) composed of clay, cataclasites, and ultracataclasites that accommodates most of the slip [*Chester and Logan*, 1986; *Chester et al.*, 1993; *Schulz and Evans*, 1998; *Sammis et al.*, 2009]. Surrounding the fault core is the damage zone (hundreds of meters to several kms in width) (Fig. 1.1). The damage zone is generated by earthquakes in different times and is seismically characterized as a low velocity zone (LVZ) composed of highly fractured materials, breccia, and pulverized rocks [e.g. *Chester and Logan*, 1986; *Schulz and Evans*, 1998, 2000; *Sammis et al.*, 2009].

Cracks in the damage zone may contain and transport fluids which play an important role on fault zone strength related to earthquake generation and rupture distribution [*Eberhart-Phillips et al.*, 1995]. Experimental studies of off-fault damage point out that the LVZ can have strong effects on earthquake rupture propagation and rupture velocity [*Sammis et al.*, 2009]. Moreover, the LVZ material may result in asymmetric damage patterns during an earthquake [e.g. *Ben-Zion and Shi*, 2005; *Dor et al.*, 2006] and could amplify the ground motion by a factor of 30 with realistic parameters [*Ben-Zion and Aki*, 1990]. Studies of damage zone healing after

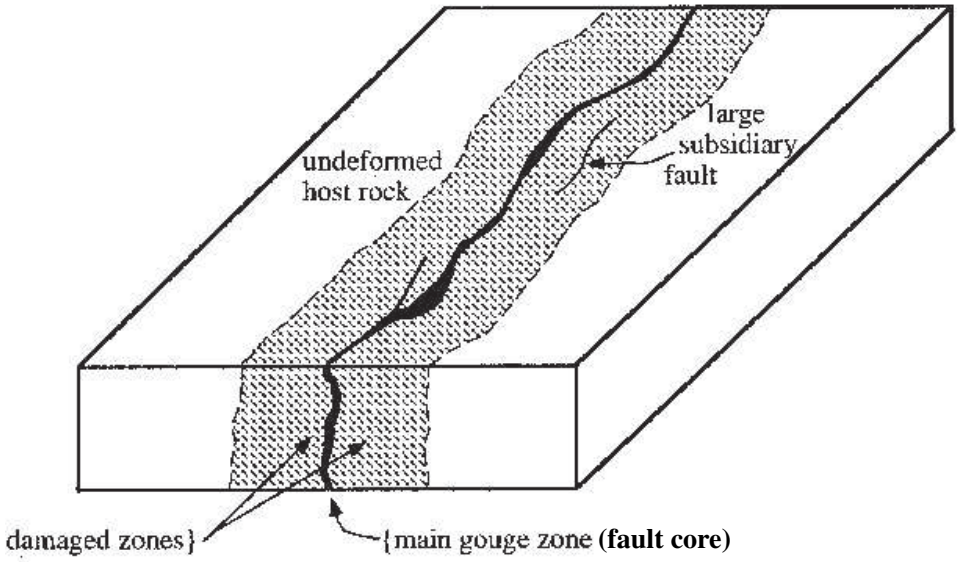

Figure 1.1: A schematic plot of a typical fault zone. A fault zone usually has a fault core surrounded by damaged zones [*Chester and Logan*, 1986].

a large earthquake highlight its importance to understanding earthquake cycle and evolution of fault systems [*Li et al.*, 1998; *Vidale and Li*, 2003]. Complex structure (geometrical and material properties) of the FZ may control the earthquake rupture process and slip localization and is important to understand the earthquake physics [e.g. *Aki*, 1979; *Scholz*, 1990; *Kanamori*, 1994; *Kanamori and Brodsky*, 2004]. Unfortunately, it is extremely difficult to determine FZ properties at seismogenic depths [*McGuire and Ben-Zion*, 2005; *Ben-Zion and Sammis*, 2009].

Many fundamental questions concerning the mechanics, structure and evolution of FZ remain unanswered despite the considerable research effort that scientists have made in the last few decades [*McGuire and Ben-Zion*, 2005; *Ben-Zion and Sammis*, 2009]. For instance, the width, degree of damage (seismic velocity drop), and depth extent of the LVZ are often studied for different fault zones using different techniques. Previous results show that the derived parameters differ significantly from one fault to another. Moreover, there has been a debate on the LVZ depth, in

which one group insisted on a down-to-seismogenic-depth (15–20 km) LVZ structure [*Li et al.*, 1997; *Li and Vernon*, 2001] while another group argued that the LVZ was only 3–5 km deep [*Ben-Zion and Sammis*, 2003; *Lewis et al.*, 2005]. In this dissertation, I will focus on addressing these questions for different fault zones using aftershock location and high-frequency local earthquake waveform modeling.

This dissertation starts in Chapter 2 with a literature review of previous geological and geophysical studies on fault zones including different methods and their advantages and limitations. Then a newly developed technique to determine fine FZ structures is introduced and will be used in the study of this dissertation.

Chapter 3 focuses on a study of 2008 Mt. Carmel, Illinois earthquake. In this chapter I developed a sliding-window cross-correlation (SCC) technique to detect small magnitude earthquakes and applied the technique to continuous waveforms recorded by the Cooperative New Madrid Seismic Network stations following the mainshock. I then relocated all events by the double-difference relocation algorithm to determine the fault plane of the mainshock by combining with focal mechanism solutions obtained using "Cut and Paste" method [*Zhu and Helmberger*, 1996].

Chapter 4 gives a systematic analysis of local earthquake travel time and waveform data recorded by temporary arrays across the San Jacinto fault zone in southern California. I described how to constrain the FZ dip using travel time data and earthquake locations. Then I used the new technique to determine the FZ width and velocity contrast to the host rock. More importantly, I found an interesting feature in the waveforms and identified it as the LVZ diffracted waves. Subsequently, I used it to determine the LVZ depth extent and estimated the uncertainties by performing synthetic tests.

In Chapter 5 the local earthquake data recorded by a dense array across the Calico fault zone in southern California were analyzed and modeled. I used the same technique to determine the LVZ width and velocity contrast. I then

determined the LVZ dip and depth of the Calico fault zone by travel time analysis for earthquakes located on both sides of the FZ.

This dissertation ends in Chapter 6 with discussion on asymmetric damage pattern observed in this study, uncertainty of the LVZ depth, and possible future work. Finally I summarized the work in conclusions.

Chapter 2: Review of Previous Fault Zone studies

The geometrical complexity and material heterogeneities of FZs make quantification of FZ properties and understanding its evolution process extremely challenging [*Ben-Zion and Sammis*, 2003, 2009]. After decades of geological and geophysical investigation of FZ structures, many questions concerning with the mechanics, structure and evolution of fault zone still remain unanswered.

2.1 Geological measurements and drilling

Field study of earthquake ruptured faults or exhumed faults can provide direction information of FZ parameters [*Chester and Logan*, 1987; *Chester et al.*, 1993; *Sieh et al.*, 1993; *Johnson et al.*, 1994; *Chester and Chester*, 1998; *Chester et al.*, 1998]. Based on geological measurements, the FZ has a fault core (or fault gouge), with a width from a few centimeters to meters, in which most of slip is localized during earthquakes. The fault core is usually composed of cataclasite and ultracataclasite and has significantly low strength, elastic moduli, and permeability relative to the surrounding rocks [*Chester and Logan*, 1986, 1987]. On either side of the fault core is a damage zone with a width from tens of meters to normally hundreds of meters [*Chester et al.*, 1993; *Ben-Zion and Sammis*, 2003]. The damage zone is generated by repeated earthquakes in geological time and composes of large number of fractures. Analysis of distribution of fractures in the damage zone can provide the geometrical and evolution information of the FZ [*Schulz and Evans*, 1998; *Savage and Brodsky*, 2010]. Interaction between fluids in fractures and rocks can alternate their chemical composition and consequently change the FZ strength [*Evans and Chester*, 1995]. In general, study of geological measurements and geochemical analysis of FZ rocks give a damage zone width range from 10 to 500 m, base upon different observation sites and different type of measurements.

For example, an analysis of distribution of micro-fractures along the Punchbowl fault, southern California, showed that the FZ consists of a roughly 40-m-thick damaged zone. However, the geochemically defined FZ in the same site is only less than 10 m wide [*Schulz and Evans*, 1998].

Although it can directly sample FZ materials, the geological studies of FZs are generally limited to the surface. The other way to directly get FZ information is to drill down to a few kilometers, e.g. the San Andrews Fault Observatory at Depth (SAFOD) in California and the Taiwan Chelungpu Fault Drilling Project (TCDP). The SAFOD experiment revealed a 200-m-wide LVZ associated with the San Andreas fault (SAF) at Parkfield with ∼30% reduction in V_p and ∼20% reduction in V_s from the well log data [*Hickman et al.*, 2007]. The material of the LVZ has a low resistivity as well. Borehole log data from TCDP shows a ∼150 m wide LVZ associated with the Chelungpu fault, with a 20% S-wave velocity reduction relative to the host rocks [*Ma et al.*, 2007].

2.2 Geodetic study

Due to the existence of large number of fractures, densities of the damage zone material are significantly lower than the host rocks. The damage zone is usually associated with a negative gravity anomaly so that structures of the damage zone can be inferred from gravity survey. Based on modeling Bouguer gravity along the San Jacinto fault in souther California, a 2-5 km wide damaged zone on both sides of the surface trace of the fault was proposed in the region [*Stierman*, 1984]. The anomalously low densities were interpreted due to both fracturing and chemical alteration. *Wang et al.* [1986] reported similar results from a gravity study across the fault in the Bear Valley section of the SAF. However, due to non-uniqueness and the low resolution of modeling gravity data, application of gravity survey on FZ structure determination is considerably limited.

Electromagnetic methods are able to image FZs based on the anomalous resistivity (or conductivity) that may be interpreted in terms of high fluid pressure, clay minerals, and deposited conductive minerals [*Ben-Zion and Sammis*, 2003]. A synthetic test of magnetotelluric imaging of FZ showed that a conductive FZ can be well imaged within the upper 10 km [*Eberhart-Phillips et al.*, 1995]. There were a few cases of imaging FZ structures with electromagnetic methods reported for various sections of the SAF [*Eberhart-Phillips and Michael*, 1993; *Mackie et al.*, 1997; *Unsworth et al.*, 1999]. *Eberhart-Phillips et al.* [1995] reviewed applications of electromagnetic technique on FZ imaging and concluded that the resolution of this technique was on the order of km.

Recently high resolution satellite image data have been used to model FZ structures. Displacements caused by an earthquake can be computed from the Interferometric Synthetic Aperture Radar (InSAR) data before and after the earthquake. Given a shear stress perturbation $\Delta\sigma_t$, the shear modulus G' of FZ and G of the ambient "intact" rocks, the FZ width w can be determined from

$$D = w\Delta\sigma_t(\frac{1}{G'} - \frac{1}{G}), \tag{2.1}$$

where D is the displacements generated by earthquake [*Fialko et al.*, 2002]. By analyzing the InSAR data before and after 1999 M_w 7.1 Hector Mine earthquake, the width of the LVZ associated with the Calico fault zone in southern California was estimated as 1.5-2 km [*Fialko et al.*, 2002; *Cochran et al.*, 2009].

2.3 Seismic reflection and tomography

Seismic reflection and refraction survey are widely used to image sub-horizontal structures but have difficulties imaging very narrow, nearly vertical FZs [*Eberhart-Phillips et al.*, 1995; *Ben-Zion and Sammis*, 2003]. To date, only a few

successful cases of illuminating the shallow part (<4 km) of a FZ have been reported [*Hole et al.*, 2001; *Chavarria et al.*, 2003; *Maercklin et al.*, 2004; *Bleibinhaus et al.*, 2007]. The resolution from seismic reflection/refraction is typically up to 500 m [*Ben-Zion and Sammis*, 2003].

P- and *S*-wave arrival time data from local earthquakes in a FZ or surrounding regions can provide constraints on structure of a FZ. All arrival times carry structural information along the ray paths between the source and receivers and then can be used to resolve subsurface structure by inversion. That is the so-called seismic tomography method. Using this technique, *Aki and Lee* [1976] found a tabular LVZ with 15% reduction in V_p extending down to 5 km along the SAF south of Hollister. Particularly, the SAF in Parkfield was imaged by many tomography results [*Lees and Malin*, 1990; *Eberhart-Phillips and Michael*, 1993; *Thurber et al.*, 2004; *Zhang et al.*, 2007, 2009]. So far results using arrival times from earthquakes and explosions revealed a 1-2 km wide LVZ extending as deep as 7 km [*Zhang et al.*, 2009]. One general issue of regular seismic tomography on a narrow LVZ is that *P* and *S* waves tend to avoid the low velocity structure so that the resolution of tomography is considerably limited. An improvement to the regular tomography may be obtained by including travel-time information of FZ head waves that spend longer time along the FZ [*Ben-Zion and Malin*, 1991; *Ben-Zion and Sammis*, 2003; *McGuire and Ben-Zion*, 2005; *Zhao and Peng*, 2008]. *Ben-Zion et al.* [1992] developed a joint inversion method using FZ head wave and *P*-wave arrival times and found a shallow LVZ (<3 km) with velocity contrast 10-20% in Parkfield.

2.4 Earthquake location

Earthquakes are usually generated by the rapid movement between two blocks of crustal faults and, therefore, spatial distribution of earthquake hypocenters can constrain on the FZ structures. With a sophisticated relative location technique,

e.g. double-difference relocation algorithm, and reasonably good station coverage, accuracies of earthquake locations are on the order of meters or tens of meters [*Got et al.*, 1994; *Shearer*, 1997; *Prejean et al.*, 2002; *Waldhauser and Ellsworth*, 2002; *Thurber et al.*, 2004; *Zhang et al.*, 2007, 2009; *Yang et al.*, 2009]. For instance, earthquakes recorded by seismometers on the surface and in the borehole in SAFOD delineate a very narrow FZ extending vertically to seismogenic depth [*Thurber et al.*, 2004; *Zhang et al.*, 2009]. In particular, locating earthquakes and their aftershocks is an effective way to map faults, especially for faults without surface rupture.

2.5 Modeling FZ trapped waves

So far the most frequently used FZ-imaging technique is to model the FZ trapped waves, which are low frequency wave trains with relatively large amplitude following the S wave. The FZ trapped waves are generated by constructive interference of supercritical reflection of seismic waves within the low-velocity fault zone, therefore they sample the FZ structure directly and can give high-resolution results (on the order of meters to tens of meters). This method has been used on different faults around the world, such as the North Anatolian fault zone in Turkey [*Ben-Zion et al.*, 2003], the Nocera Umbra fault zone in central Italy [*Rovelli et al.*, 2002], the San Andreas fault zone at Parkfield [*Li et al.*, 1990; *Korneev et al.*, 2003; *Li et al.*, 2004; *Li and Malin*, 2008], the Lavic Lake fault zone [*Li et al.*, 2003], the Hector Mine earthquake ruptured zone [*Li et al.*, 2002], the Calico fault zone [*Cochran et al.*, 2009], the Landers fault zone [*Li et al.*, 1994, 1999, 2000; *Peng et al.*, 2003], and the San Jacinto fault zones in California [*Li et al.*, 1997; *Li and Vernon*, 2001; *Lewis et al.*, 2005]. Most FZ trapped wave studies revealed a LVZ ranged from $\sim$75 m to $\sim$350 m in width with shear wave velocity reduced by 20% to 50%.

However, uncertainties of the trapped wave modeling results due to non-uniqueness and trade-off among FZ parameters, especially the FZ width and

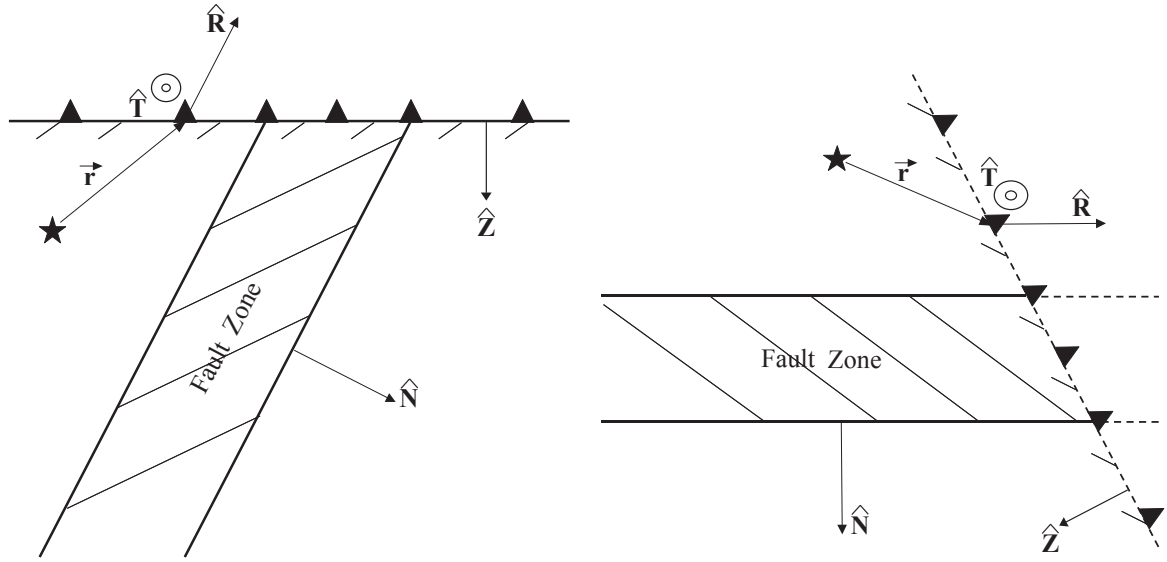

Figure 2.1: Left panel: An arbitrarily-oriented tabular FZ model. Right panel: the rotated FZ model. The star denotes an earthquake and triangles represent stations. Modified after *Li* [2005].

velocity drop, have been noted by previous studies [*Peng et al.*, 2003; *Lewis et al.*, 2005]. Moreover, it is still under debate whether the trapped energy comes from a shallow LVZ structure or deep part [*Li et al.*, 1997; *Li and Vernon*, 2001; *Ben-Zion and Sammis*, 2003; *Lewis et al.*, 2005]. For example, a 15–20-km-deep LVZ of the San Jacinto fault zone (SJFZ) was reported by *Li and Vernon* [2001] while another group using the same dataset argued that it was only 3–5 km deep [*Lewis et al.*, 2005]. A recent numerical analysis of FZ trapped wave pointed out that determination of FZ structure at seismogenic depth requires using higher frequency waveforms than the FZ trapped wave [*Wu et al.*, 2008].

2.6 Modeling FZ-reflected body waves

Recently, we developed a technique to determine high-resolution FZ structure using arrival times and waveforms of high-frequency body waves from local

earthquakes [*Li et al.*, 2007]. The new technique computes arrival times for direct and FZ-reflected P and S waves by generalized ray theory (GRT) [*Helmberger*, 1983], which decomposes a seismogram into responses of many individual generalized rays allowing us to trace and analyze different seismic phases. In order to use the GRT, we need to simplify a 3-D FZ model into a 1-D model. In a tabular FZ model, an arbitrarily-oriented low-velocity layer is embedded in a uniform half-space (Fig. 2.1). We can rotate the tabular FZ model into a horizontally layered 1-D model. Using two vectors, $\hat{N}$ (the fault normal direction), and $\vec{r}$ (the direction pointing from the source to the receiver), we can derive two mutually perpendicular unit vectors:

$$\hat{T} = \frac{\hat{N} \times \vec{r}}{|\hat{N} \times \vec{r}|}, \tag{2.2}$$

$$\hat{R} = \hat{T} \times \hat{N}. \tag{2.3}$$

The three vectors, $\hat{R}$, $\hat{T}$, and $\hat{N}$, form a right-hand orthogonal vector base. In this coordinate system, the FZ normal direction $\hat{N}$ points downward. $\hat{R}$ is the radial direction at the station and $\hat{T}$ is the transverse direction [*Li et al.*, 2007].

Fig. 2.2 shows a synthetic waveform record section for an earthquake located west of a hypothetic FZ. We set up the FZ model with a width of 300 m and velocity drop of 40% in both V_p and V_s. The FZ has a N-S orientation and the seismic array is perpendicular to the strike. Because of the low-velocity FZ, the direct P and S arrivals at the eastern stations are delayed starting from station located at offset 0 m to station at 300 m (Fig. 2.2). Besides the direct P and S waves, multiple internal P and S reflections from boundaries of the FZ are also shown in Fig. 2.2. Their corresponding ray paths are shown on the left-hand side. Here we label them as P^2, S^2, P^4, S^4 and so on, where the superscript indicates the number of additional ray path legs in the FZ. For stations located outside the FZ,

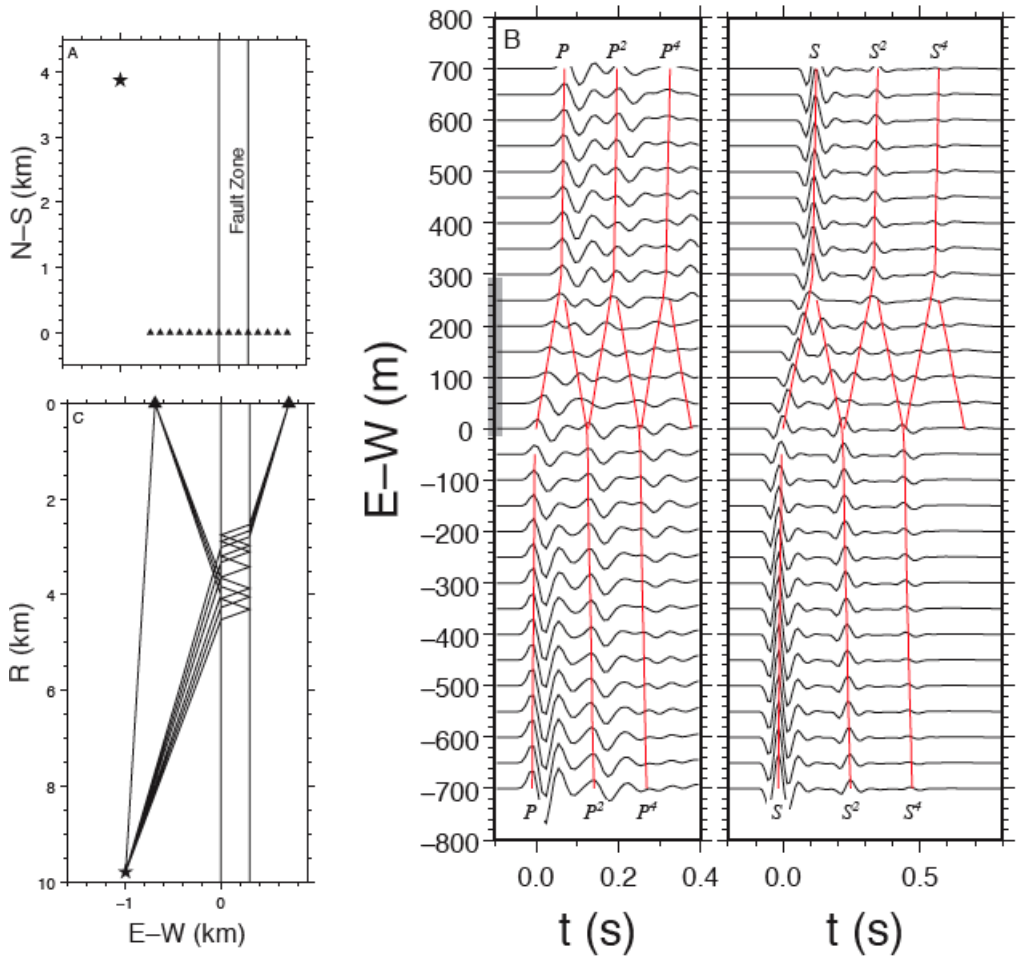

Figure 2.2: (a) Location of a linear seismic array (triangles) across a 300-m-wide FZ. The earthquake (star) is located 1 km west to the western FZ boundary. (b) The vertical (left-hand panel) and fault-parallel (right-hand panel) components of seismograms o f the linear array. The grey bar represents location of the FZ. Red lines show arrival times of major body-wave phases. Their ray paths to two stations are shown in (c). After [*Li et al.*, 2007].

the multiple reflections show little moveout relative to the direct arrivals. For stations located within the FZ, the forward and backward reflections at the boundaries of the FZ have the opposite travel time moveouts, forming a characteristic "V"-shaped pattern (Fig. 2.2).

In contrast, the travel time pattern for an earthquake located in the FZ is drastically different. Fig. 2.3 shows a record section for an event located in the

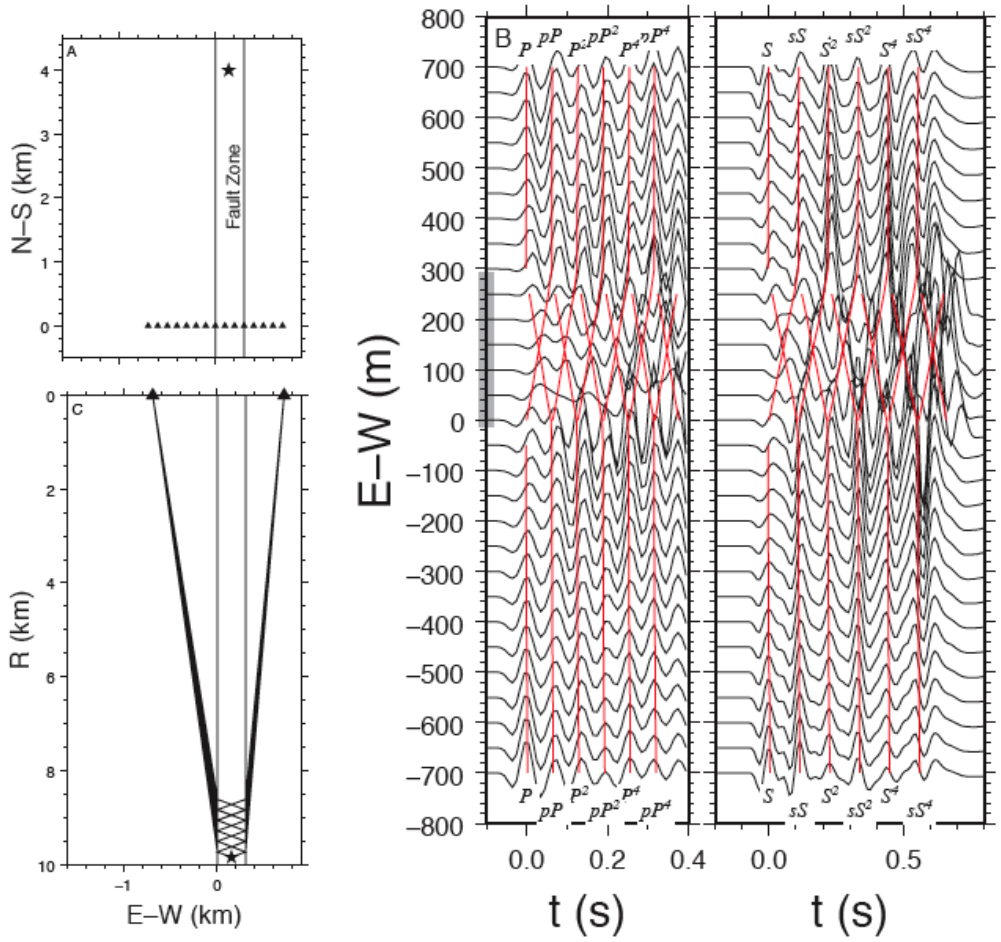

Figure 2.3: Same to Fig. 2.2. The earthquake is located in the FZ. After [*Li et al.*, 2007].

hypothetical FZ. For stations in the FZ, the direct P and S arrivals are delayed and the delays from the opposite reflections by the FZ boundaries have the opposite moveouts, forming a distinctive "X"-shaped pattern. In both cases, the delays of the direct P and S arrival times start from stations at the FZ boundaries. Therefore, we can constrain the width of the LVZ directly. The differential arrival times between the direct and FZ-reflected P and S waves (labeled P^2 and S^2 in Fig. 2.2) are used to determine the velocity drops of the LVZ compared to the host rock. Therefore, the trade-off between the FZ width and velocity contrast is greatly reduced (Fig. 2.4).

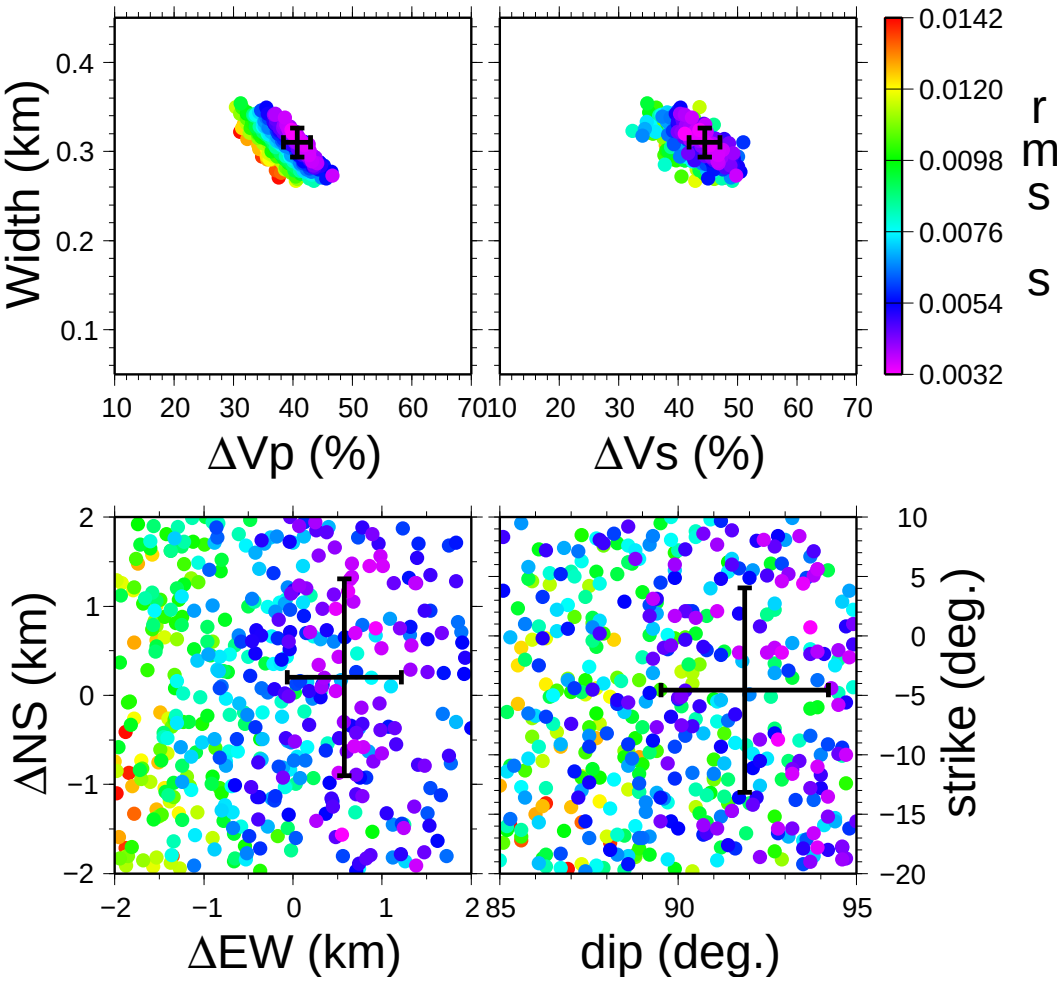

Figure 2.4: FZ width and P and S velocity drops as determined by least-squares inversion of arrival times of the direct and FZ-reflected P and S phases. The inversion is repeated 500 times while randomly perturbing the event location, FZ strike and dip. Black cross denotes the weighted average value of all acceptable solutions with its length equal to one standard deviation. After [*Li et al.*, 2007].

Application of this technique on a dataset of waveforms from local aftershocks following the 1992 Landers M_w 7.3 earthquake revealed a ∼300-m-wide LVZ with 35-60% reduction in P and S velocities relative to the host rock. The LVZ was estimated to extend to a depth of ∼7 km [*Li et al.*, 2007]. In this dissertation, I will analyze high frequency body wave waveforms of local earthquakes recorded by temporary arrays across the San Jacinto fault zone (SJF) and the Calico fault zone in southern California and determine their fine structures.

Chapter 3: Fault-Plane Determination of the 18 April 2008 Mt. Carmel, Illinois, Earthquake

On April 18, 2008, 09:37:00 UTC, a moderate earthquake (M_w 5.4) occurred in Mount Carmel, southeastern Illinois, and caused minor structural damage in the surrounding area. It was felt over a wide range of the central United States (U.S.) as far west as Kansas, as far north as Michigan, and as far south as Georgia. An automatic earthquake location program from U.S. Geological Survey quickly located it at 87.89°W 38.45°N, with a focal depth 11.6 km. The magnitude of the earthquake was first determined as M_w 5.2 and later updated to M_w 5.4 [*USGS*, 2008]. A near real-time moment tensor solution of the earthquake showed an almost pure strike-slip focal mechanism (Fig. 3.1) [*Herrmann et al.*, 2008].

The earthquake was followed by numerous aftershocks in the next two weeks, including two events with magnitudes of M_w 4.6 and 4. Moreover, aftershocks continued to happen till three months after the mainshock including several M_w ~3.0 events. This series of earthquakes occurred within the Wabash Valley Seismic Zone (WVSZ), which covers a large area of southeastern Illinois and southwestern Indiana and is an important source of hazard in the central U.S. [*Nuttli*, 1979; *Ault and Sullivan*, 1982; *Ault et al.*, 1985].

3.1 Seismicities and tectonics in the Wabash Valley Seismic Zone

In the past 40 years, several moderate earthquakes have occurred in the WVSZ. The largest event was the November 9, 1968 earthquake with an m_b of 5.5 which was felt as far as St. Louis and Chicago. *Stauder and Nuttli* [1970] located it at 88.48°W, 37.95°N with a focal depth of 25 km. Its focal mechanism solution showed that it was due to a north-trending thrust motion [*Stauder and Nuttli*, 1970; *Herrmann*, 1973]. The June 10, 1987 earthquake with an m_b of 4.9 [*Taylor et al.*,

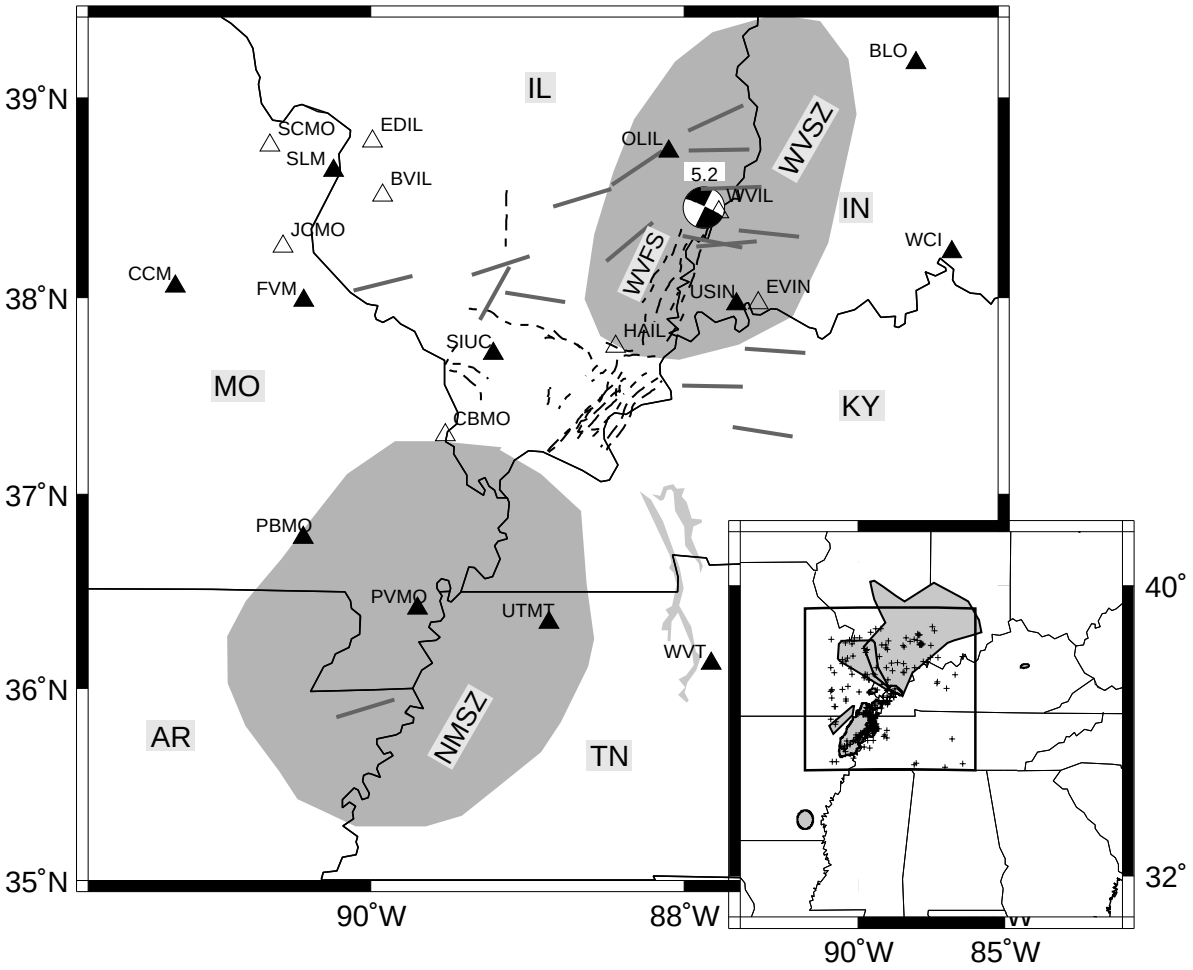

Figure 3.1: The beach ball represents the epicenter of the April 18, 2008 Mt. Carmel earthquake, Illinois. The shaded areas are the Wabash Valley Seismic Zone (WVSZ) and New Madrid Seismic Zone (NMSZ), from *Gomberg and Schweig* [2002]. Dashed lines represent faults and graben structures in southern Illinois, from *ISGS* [1995]. Line segments show the stress orientation in the region [*Heidbach et al.*, 2008]. Black triangles denote broadband seismic stations of Cooperate New Madrid Seismic Network and open triangles denote strong motion stations. Inset: black box is the study area. Black crosses represent seismicity in the region, from the NEIC catalog (1973-2008) and the catalog of Eastern, Central and Mountain States of U.S. (1534-1986). Shaded areas are liquefaction features in the region, including Wabash Valley liquefaction features, St. Louis-Cape Girardeau liquefaction features, and Western Lowlands liquefaction features [*USGS and ISGS*, 2006]. WVFS: Wabash Valley fault system.

1989; *Langer and Bollinger*, 1991] and the June 18, 2002 earthquake with an m_b of 5.0 [*Kim*, 2003] also caused minor damage. Both events exhibited strike-slip focal mechanisms. A study of liquefaction features in Holocene sediments provided

evidence of large prehistoric earthquakes with m_b of 6.2 $\sim$ 6.7 in the region [*Obermeier et al.*, 1991]. More liquefaction feature studies had documented at least seven and probably eight strong prehistoric earthquakes occurred during the Holocene, and at least one during the latest Pleistocene era [*Munson et al.*, 1995, 1997; *Obermeier*, 1998]. The largest prehistoric event magnitude was estimated as M 7.5. By modeling stress changes caused by the 1811-1812 New Madrid earthquake sequence and using recent earthquake distribution, *Mueller et al.* [2004] suggested that the third event (01/23/1812) in the sequence occurred in the WVSZ, 200 km northeast from the New Madrid seismic zone (NMSZ). The WVSZ and the NMSZ are the dominant sources of hazard in the central and eastern U.S. and therefore it is imperative to map the resulting hazard for purposes of mitigating their effects [*Nuttli*, 1979; *Frankel et al.*, 1996, 2002; *Eagar et al.*, 2006].

Compared to the NMSZ, the WVSZ has so far received far less attention, partly because of the lower seismicity (Fig. 3.1). However, there were 5 earthquakes with magnitude larger than 4.5 that happened in the WVSZ while only 2 earthquakes with similar magnitude happened in the NMSZ in the past 40 years (Fig. 3.2). The main geological feature associated with the WVSZ is the 90-km-long and 50-km-wide Wabash Valley fault system (Fig. 3.1), which consists of a network of NE-SW trending faults [*Ault and Sullivan*, 1982; *Ault et al.*, 1985; *Rene and Stanonis*, 1995; *Woolery*, 2005]. The faults were first discovered by petroleum exploration drilling in the early 1900s and were then widely studied by geological and geophysical investigations [*Pratt et al.*, 1992; *McBride et al.*, 2002; *Duchek et al.*, 2004; *McBride et al.*, 2007]. Previous studies suggested that those faults were high-angle normal faults that formed in late Pennsylvanian or younger and pre-Pleistocene time [*Rene and Stanonis*, 1995; *Woolery*, 2005]. But origins of those faults still remain enigmatic [*Marshak and Paulsen*, 1996; *Wheeler and Ravat*, 2002]. Only a few faults have been associated with known earthquakes. For

example, *McBride et al.* [2007] suggested that the 1968 m_b 5.5 and the 1987 m_b 4.9 earthquakes occurred on pre-existing deformation zones reactivated by contemporary stresses. Seismic reflection study shows that the fault system is within sedimentary rocks of Cambrian through Pennsylvanian in the region [*Rene and Stanonis*, 1995]. There is no fault cutting the Quaternary sediment atop Pennsylvanian strata. Beneath the sedimentary rocks there is inferred to be a granite-rhyolite terrane based on outcrops of rhyolite, dacite, and related granitic plutons in the St. Francois Mountains of southeastern Missouri (where I have been in our petrology field trip). This igneous province stretches from northern Mexico to eastern Québec, Canada [*McBride et al.*, 2007].

Since none of the faults has surface expression, seismic methods have to be applied to investigate the faults down to the seismogenic depth. A near real-time moment tensor solution of the 2008 earthquake showed an almost pure strike-slip focal mechanism [*Herrmann et al.*, 2008]. In addition to the mainshock, we computed moment tensor solutions for the four largest aftershocks by the "Cut and Paste" method [*Zhu and Helmberger*, 1996]. All the five earthquakes have similar strike-slip focal mechanisms indicating that the strike of the fault is either NE-SW or NW-SE. Because of the ambiguity of the fault plane from moment tensor solutions, other information has to be used to determine the true fault plane. Accurate locations of aftershocks can give good constraint on fault plane parameters (strike, dip, and depth). In this chapter, I relocated the mainshock and its aftershocks to determine the fault plane of the mainshock.

3.2 Seismic event detection

In order to delineate the fault plane, we need a large number of aftershocks. The Center for Earthquake Research and Information (CERI) located 30 aftershocks for the Mt. Carmel earthquake series in the first two weeks. Those events were detected

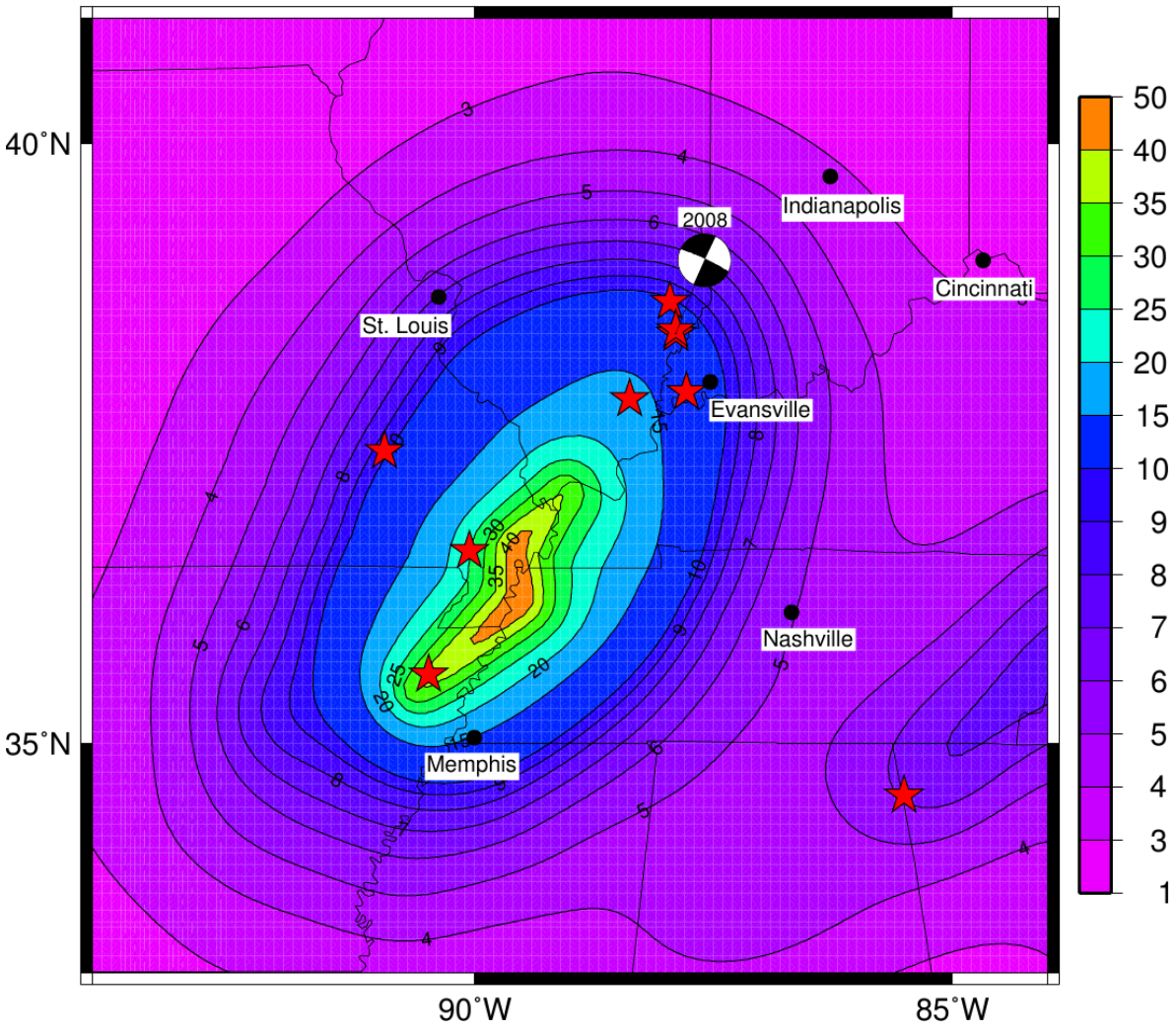

Figure 3.2: Seismic hazard expressed as peak ground acceleration, in %g, expected to be exceeded in a 50-yr period with a probability of 10 percent [*Petersen et al.*, 2008]. Red star denotes earthquakes with magnitude larger than 4.5 since 1960. Focal mechanism solution is shown for the 18 April 2008, Illinois, earthquake.

by the traditional short-term average (STA) over long-term average (LTA) method. This is the so-called STA/LTA power detector originally proposed by *Freiberger* [1963]. This method has been widely used by worldwide seismic networks and has automatically reported most of seismic events happened in the world. However, there is a threshold value, typically 3-4 for the Global Seismic Network, on the magnitude of earthquakes that can be detected. Small events below the threshold were likely missed by this method.

Another way to detect events is to cross-correlate seismic waveform data with waveform records of known events (template events). That is called the matched-signal detector [*van Trees*, 1968; *Whalen*, 1971]. This method has so far received little attention because it requires a template event and the sensitivity of detection highly depends on the similarity between the template and the signal in the incoming waveform data. The matched signal detector is very useful to detect low signal-noise-ratio (SNR) signal and unusual seismic events such as tremor [*Shelly et al.*, 2007a]. With the array-based beam forming technique, this method can detect events with magnitudes as low as -1 [*Gibbons and Ringdal*, 2006].

3.3 Sliding-window cross correlation technique

Let $f(t)$ and $g(t)$ represent two time series, conventional non-normalized cross-correlation of the two is

$$C(t) = f(t) * g(t) = \int_{-\infty}^{\infty} f(t+\tau)g(\tau)d\tau. \tag{3.1}$$

If we assume $f(t)$ is a continuous waveform of ground motion and $g(t)$ is the waveform of a template event with a finite length of T, we can write the above equation as

$$C(t) = f(t) * g(t) = \int_{-T}^{0} f(t+\tau)g(\tau)d\tau. \tag{3.2}$$

Note that only $f(\tau)$ between $t-T$ and t are needed to compute $C(t)$. It is equivalent to "sliding" the template signal, $g(t)$, over the infinitely long waveform $f(t)$. We call it sliding-window cross-correlation (SCC).

If we apply the SCC to the three channels (e.g., BHZ, BHE, or BHN) separately, we face a problem of inconsistent detections by different channels. Different numbers of detections may be obtained on different channels depending on the SNR of the continuous waveform. Even if all the channels successfully detect the same

event, they may not agree with each other on the detection time exactly. To solve the problem, we revised Eq.(3.2) so that the SCC can be applied to three components of waveform data simultaneously. Let $\mathbf{f}(t)$ and $\mathbf{g}(t)$ represent the three-component vectors of the ground motion and the template signal respectively, their inner product is defined as

$$\langle \mathbf{f}|\mathbf{g}\rangle = \int_{-T}^{0} \mathbf{f}(t+\tau)\cdot\mathbf{g}(\tau)d\tau, \tag{3.3}$$

and the normalized cross-correlation coefficient is

$$C(t) = \frac{\langle \mathbf{f}|\mathbf{g}\rangle}{\sqrt{\langle \mathbf{f}|\mathbf{f}\rangle \langle \mathbf{g}|\mathbf{g}\rangle}}. \tag{3.4}$$

One obvious advantage is that there will be only one detection time for each detection. False detections are also reduced because we include all phase information from the three channels.

An example of detection by the SCC using three-component data simultaneously is shown in Fig. 3.3. The three traces on the top represent the three channels of a 5-minute-long seismogram at a broadband seismic station OLIL. The bottom trace is output cross-correlation coefficients of the SCC. We used a 15-second-long waveform of an M_L 3.3 aftershock as the template (Fig. 3.4). Five events were detected in the 5-minute-long waveforms by setting the cross-correlation coefficient threshold value to be 0.6. All detected events have relatively clear S-wave arrivals but only two events (No. 2 and 5) have recognizable P-wave arrivals. Fig. 3.4 shows that the SCC detector can detect low SNR events (e.g., events No. 3, 4, and 6) because it uses all phase information from the three channels. In contrast, the STA/LTA detector is likely to miss those low SNR events, especially since the STA/LTA is normally applied to the vertical channel only. Moreover, the SCC detector can estimate the magnitude of a detected event by using the amplitude

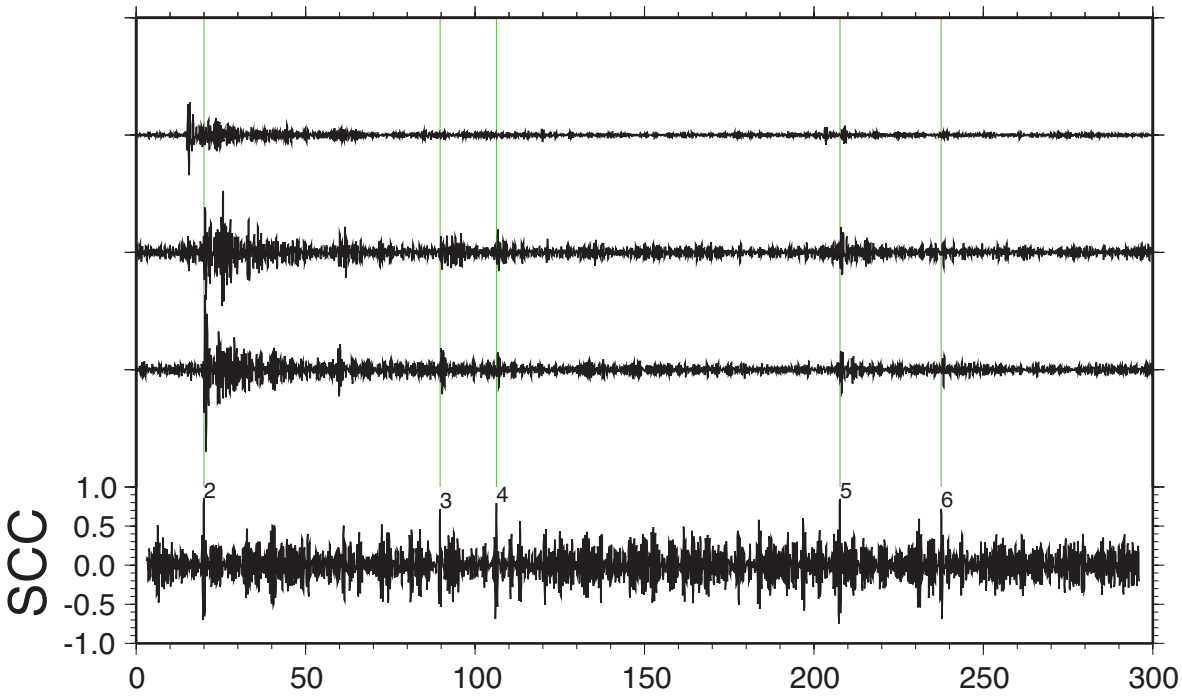

Figure 3.3: An example of sliding-window cross-correlation (SCC) detection. The three traces on the top are channels of velocity recordings of station OLIL. The trace at the bottom is the cross-correlation coefficient of the SCC detection using an M_L 3.3 template event, see Fig. 3.4. Numbers marked on the trace correspond to events detected by the SCC.

ratio A/A_t between the detected event and the template,

$$m = m_t + log(A/A_t), \tag{3.5}$$

where m_t is the magnitude of the template event.

3.4 Data and results

Data used in the aftershocks detection were collected from broadband seismic stations of the Cooperative New Madrid Seismic Network (CNMSN). Three stations have recording sample rates of 40 samples per second and others are 20 samples per second. We retrieved the continuous data from April 16, 2008 to May 2, 2008 and

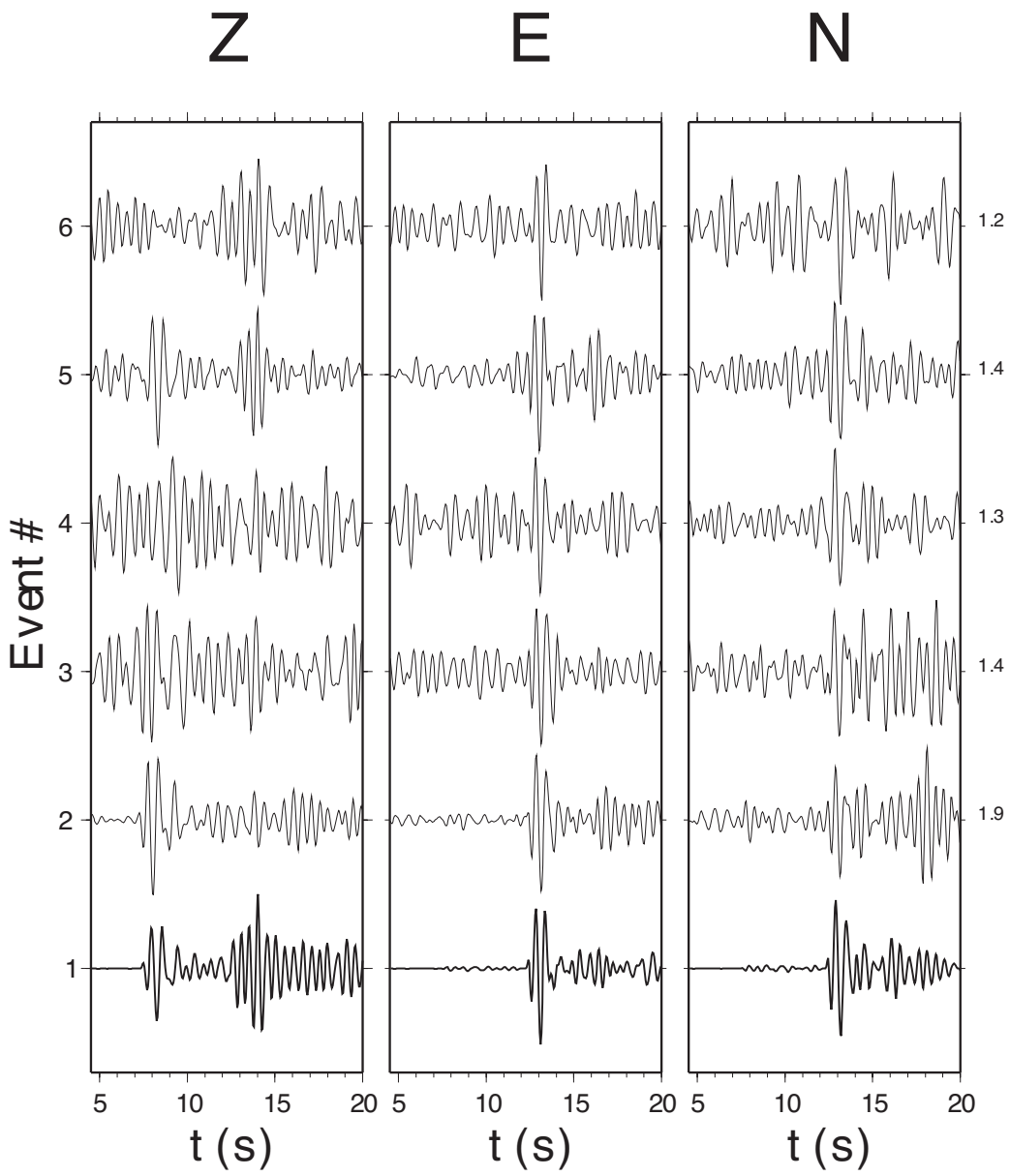

Figure 3.4: Three components (vertical, east, and north) of the template signal (at the bottom) and the SCC-detected events in Fig. 3.3. Numbers on the right show the magnitudes estimated from amplitude ratios of the waveforms to those of the template event.

saved them in one-day long recordings. A band-pass filter from 0.3 to 8 Hz was applied to the waveforms data. Another 8 strong-motion stations (Fig. 3.1) of the SLU network were added in the process of the double-difference relocation to improve the relocation results. Data from the strong motion stations were converted

to velocity records and band-pass filtered from 1 to 6 Hz.

3.4.1 Event detections by the SCC

CERI located 37 events in the 2008 Illinois earthquake sequence, including the April 18 mainshock, 30 aftershocks in the first two weeks, and 6 aftershocks thereafter. We performed waveform cross-correlation among all the events. Based on the waveform similarity, we divided these events into two groups. We selected one event from each group as the template. The two templates have magnitudes of M_L 3.3 and 3.0, respectively. We then calibrated the SCC detection parameters, e.g., the length of the template waveforms and threshold value of the SCC coefficient, by applying the SCC technique to the located events in the catalog. After the calibration, we chose the length of template waveforms to be 4 s (1 s before and 3 s after the S-arrival). The SCC coefficient threshold was set to 0.6. By setting the above parameters, we can detect all events in the catalog by the two templates. In order to detect small-magnitude aftershocks and maximize the number of detections, we only applied the SCC technique to the closest station OLIL, 37 km from the mainshock (Fig. 3.1). We set the smallest magnitude of events to be M_L 1.0 because extremely small events would not have good waveform recordings at further distant stations so that there were not enough P- and S-arrivals to locate them later.

The SCC technique detected 151 aftershocks from April 16 to May 2, 2008 (see SUPPLEMENT material). We only found 3 false detections after visually inspecting the waveforms. We did not find any foreshocks in this earthquake sequence from at least 2 days before the mainshock. Most aftershocks (100) occurred within 24 hours after the mainshock. Decay in the number of aftershocks obeys the Omori's law (Fig. 3.5). The magnitudes of aftershocks varied from M_L 1.0 to 4.6 and the magnitude-frequency distribution follows the Gutenberg-Richter power law with a b-value of 0.6 (Fig. 3.5). Fig. 3.5 also shows the magnitude-frequency distribution

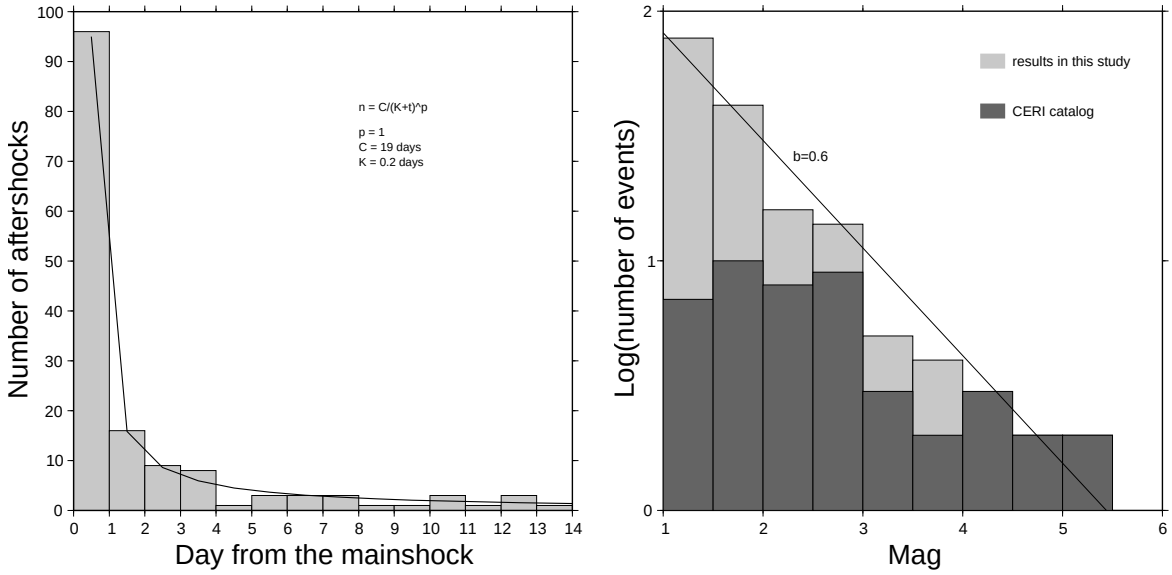

Figure 3.5: Left, temporal distribution of aftershocks in the first two weeks after the mainshock. Right, magnitude-frequency distribution of the April 18, 2008 Illinois earthquake sequence.

based on the events detected by the regional seismic network. It shows that regional network earthquake catalog becomes incomplete at M_L∼4. The largest aftershock that was missed by the catalog is an M_L 3.7 event. It occurred 4 minutes after the mainshock so that its signals were buried in the coda of the mainshock.

3.4.2 Double-difference relocations

Locating earthquake is a classic but still active research subject. Accuracy of location results depends on several factors, such as the station coverage, the number of available phases, and the velocity model used [*Pavlis*, 1986]. Relative location methods can effectively reduce the uncertainties due to structure and thus give more reliable results [*Pavlis*, 1992; *Waldhauser and Ellsworth*, 2000]. For example, double-difference relocation algorithm is a sophisticated relative earthquake location technique and has been widely applied to different tectonic regions around the world [*Waldhauser and Ellsworth*, 2000, 2002; *Hauksson and Shearer*, 2005]. This method inverts differential travel times (P- and S-wave) at the same station

Table 3.1: Velocity model used in the double-difference relocation [*Herrmann*, 1979].

Depth, km	V_p, km/s	V_s, km/s
0.0	5.00	2.89
1.0	6.10	3.52
10.0	6.40	3.70
20.0	6.70	3.87
40.0	8.15	4.70

between two events and uses a 1 dimensional velocity model on which relative locations of spatially close events are not strongly dependent [*Waldhauser and Ellsworth*, 2000; *Hauksson and Shearer*, 2005]. Therefore, we use the double-difference relocation algorithm to locate all the detected events.

Twenty stations of the CNMSN and the SLU networks were used. Two stations, including OLIL, are within 40 km of the mainshock. Station coverage is fairly good in azimuth (Fig. 3.1). We first estimated the origin times of detected events based on the detection times at OLIL, calculated their theoretical P-wave arrival times at all stations, and extracted their waveforms. We then obtained accurate P- and S-wave differential travel times between any two events at each individual station by waveform cross-correlation. The measurement errors of the differential times were estimated to be less than 0.05 s. In total we had 2877 P- and 7054 S-wave differential time measurements.

Before we tried to relocate all the detected events, we tested the relocation algorithm with synthetic data to determine how reliably the observed differential travel times can locate the events. We put 151 artificial events randomly along a ring centered at the mainshock location on an arbitrarily oriented fault plane. We then generated synthetic differential travel times using a velocity model for the central U.S. (Table 3.1) [*Herrmann*, 1979]. We added random noise of up to 0.1 s to the synthetic differential times. We found that the minimum number of observed differential times of event pairs (the minimum number of links) is critical for reliably

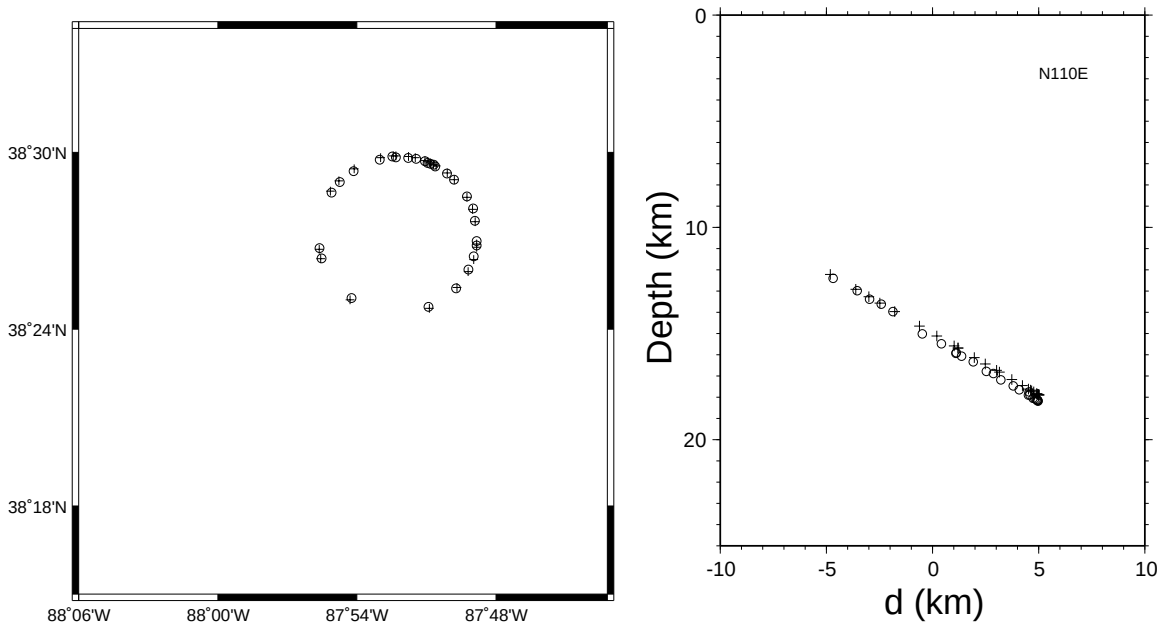

Figure 3.6: Relocation test on the basis of synthetic differential arrival times. Crosses are initial locations and circles are double-difference results. On the left is map view and on the right is the cross section.

locating events. For our synthetic data, some events would be located with large errors if the number is less than 6. By requiring the minimum number of links to be 6, only 28 events are considered to be connected to form a cluster so that their locations can be solved by the double-difference method (Fig. 3.6). Other events were discarded in the relocation process because they did not have enough differential travel-time observations to join in the cluster.

We then used the observed differential times to locate all the 28 aftershocks. It took 10 iterations to reduce the rms of travel time residuals from 1.7 s to 0.06 s, a 96% rms reduction. The uncertainties of final locations of the 28 events are about 100 m in both horizontal and vertical directions.

Relocation results are plotted in Fig. 3.7. All these events occurred within a narrow NW-SE trend, approximately 5 km in length. Our results agree with aftershock locations of *Horton et al.* [2008], who located more than 150 aftershocks using 14 temporary instruments deployed in the vicinity of the mainshock. We

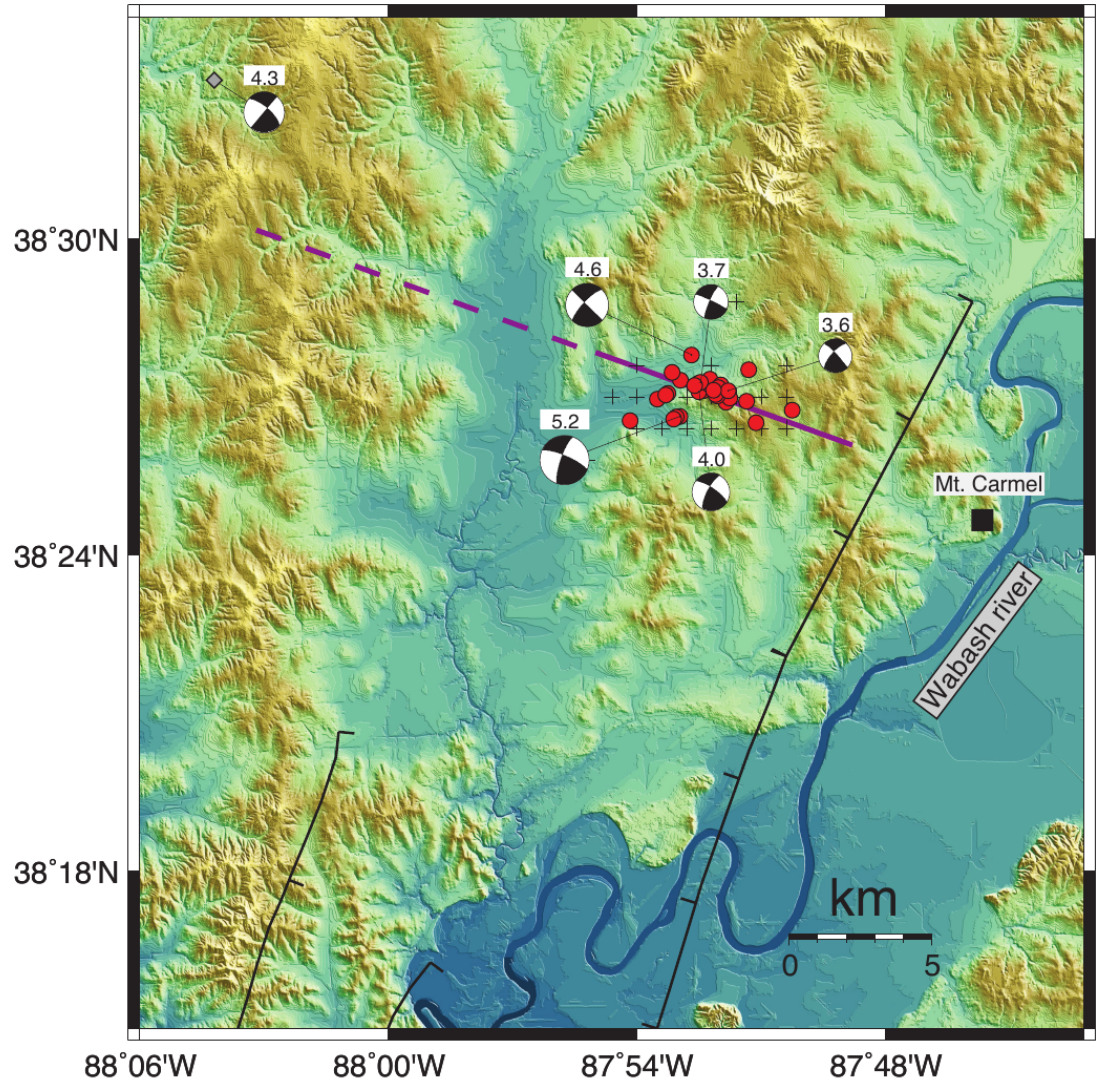

Figure 3.7: Red dots show locations of earthquakes located in this study. The straight line represents the estimated fault orientation (292°) from the locations. Black crosses are event locations in the CERI catalog. Mapped normal faults of the area are shown as black traces [*ISGS*, 1995]. The gray diamond represents the location of an M_w 4.3 earthquake occurred in 1974.

computed the fault plane parameters by fitting all event locations with a plane by minimizing the L1 norm of the distances of events to the plane. The best-fit plane has a strike of 292°±11° and is dipping to the NE by 81°±7°. Event distribution suggests that the fault extends from ∼10 km to ∼18 km in depth(Fig. 3.8).

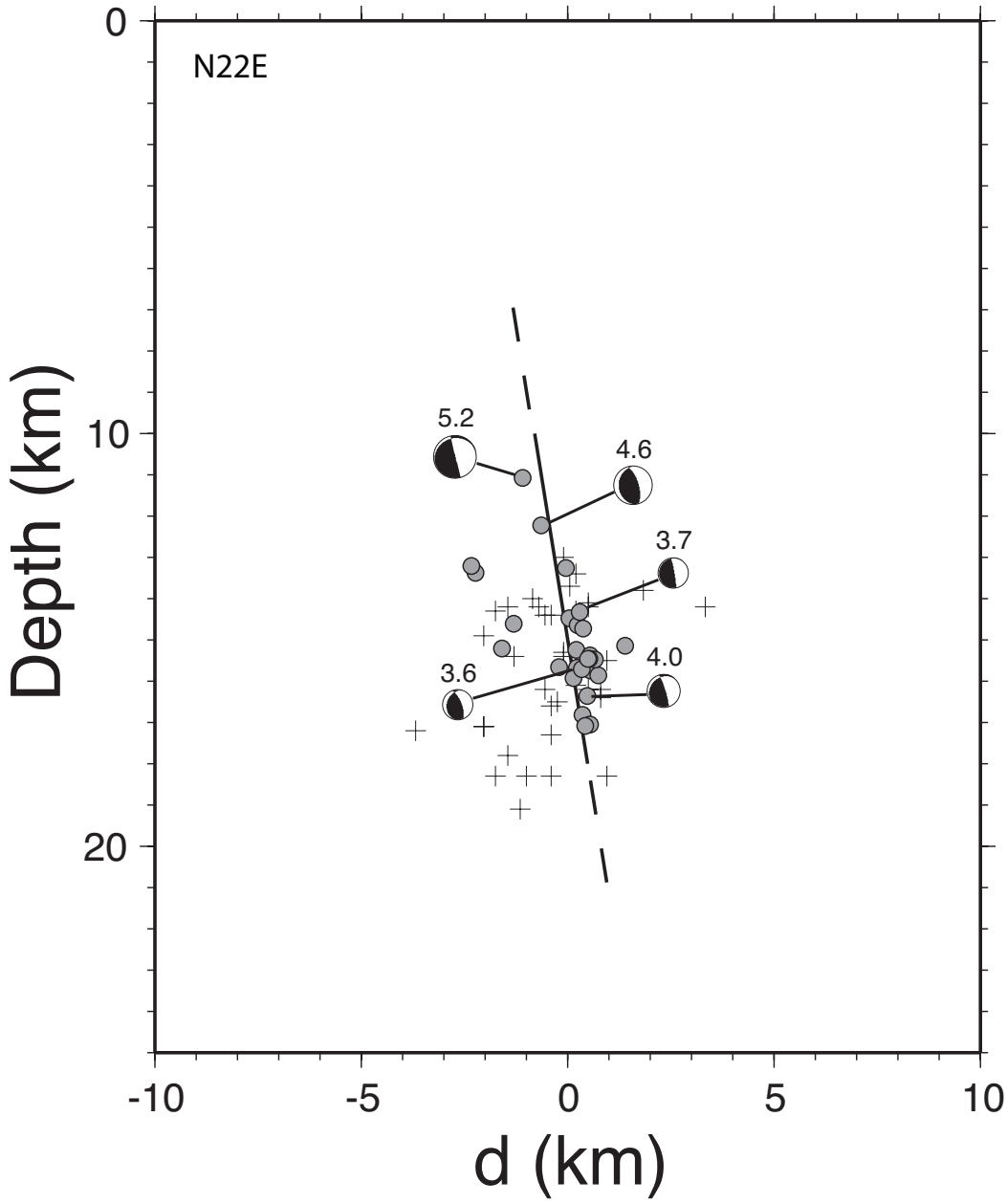

Figure 3.8: A vertical cross-section oriented N22°E across the fault. Grey dots show event locations determined in this study. Black line represents the fault plane inferred from the locations. Black crosses are locations in the CERI catalog.

3.4.3 Moment tensor solutions

Moment tensor solutions were computed for the mainshock and four largest aftershocks by the "Cut and Paste" method [*Zhu and Helmberger*, 1996]. This

Table 3.2: Moment tensor solutions for the mainshock and four largest aftershocks.

date	hr,min,sec	M_w	strike°	dip°	rake°
20080418	093700	5.2	295	76	14
20080418	151416	4.6	314	90	15
20080421	053829	4.0	304	74	18
20080425	173100	3.7	295	85	10
20080605	071314	3.6	316	82	18

method decomposes seismograms and uses amplitude information in different time windows (e.g., *Pnl*/surface wave) to increase the stability and resolution of focal mechanism solution. The Green's functions were computed using a Haskell propagator matrix method [*Zhu and Rivera*, 2002] and a velocity model for central US [*Herrmann*, 1979] (Table 3.1). An example of the focal mechanism inversions is shown in Fig. 3.9.

We used the broadband waveform data from the CNMSN stations and applied a bandpass filter from 0.5 to 5 s. Table 3.2 lists the focal mechanism solutions of the mainshock and four largest aftershocks. All these events have nearly vertical strike-slip focal mechanisms (Fig. 3.7). The strike of one of the fault planes agrees with the strike of the fault plane determined from aftershock locations. By combining the moment tensor solutions and the relocation results, we conclude the fault causing the April 18, 2008 earthquake is a WNW-ESE-trending left-lateral strike-slip fault.

3.5 Discussion

The SCC method is very effective in detecting low SNR signals of small events, about one magnitude lower than the STA/LTA detector [*Gibbons and Ringdal*, 2006]. It has been applied in exploration geophysics and in nuclear test monitoring by screening out well-known sources (e.g., quarry explosions) [*Harris*, 1991]. Recently, it is also used to detect low-frequency earthquakes and non-volcanic

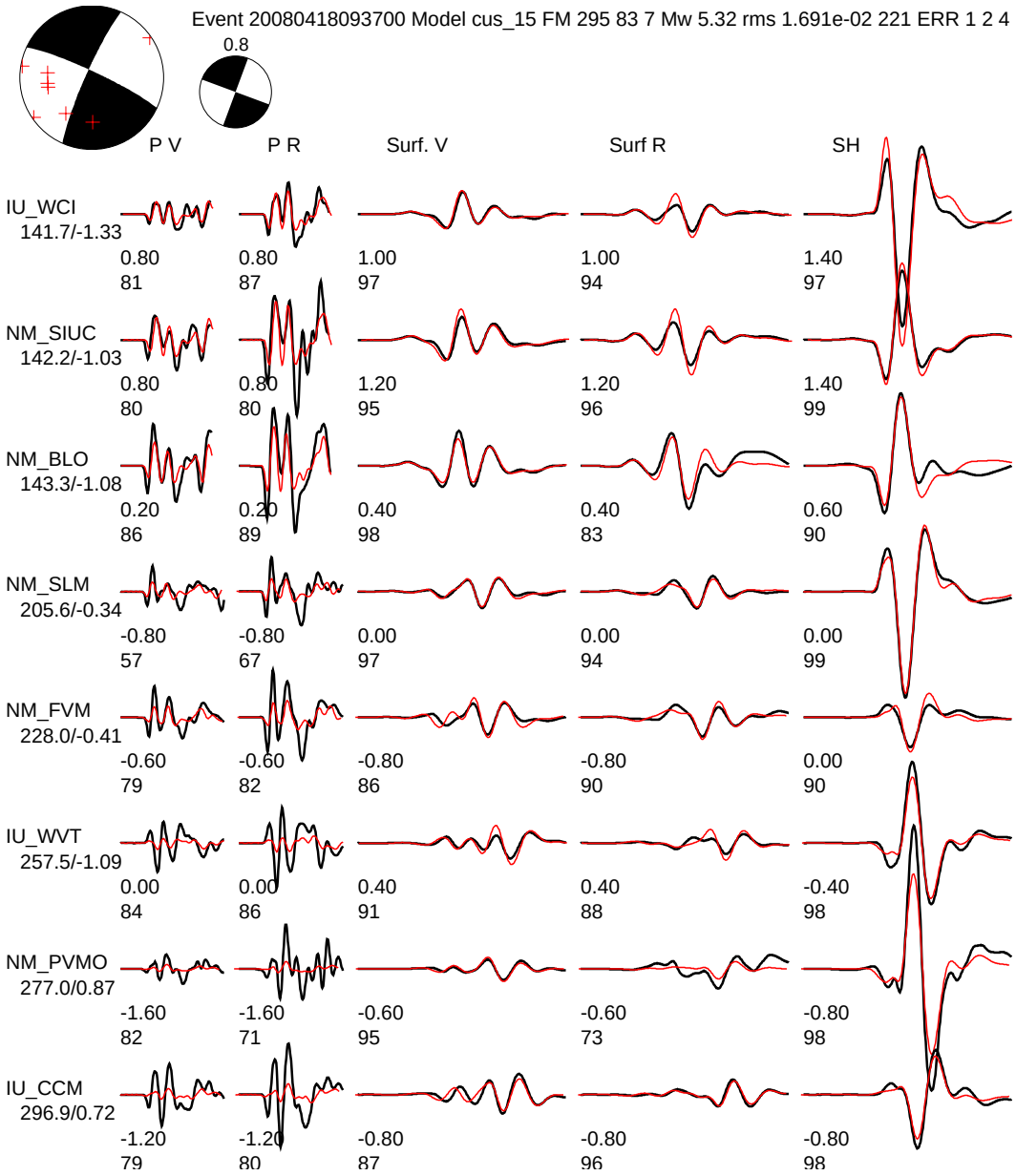

Figure 3.9: Event name, model name, focal mechanism solution, moment magnitude, and residuals are shown on the top. Station name is on the left following by data (black) and synthetic (red) seismograms for different components.

tremors [*Shelly et al.*, 2007a, b]. This study shows that this technique is suitable for detecting aftershocks because they have similar focal mechanisms and occurred in the vicinity of the mainshock. In particular, it can be efficiently used to detect aftershocks immediately following the mainshock, which are usually difficult to

detect and to locate with a conventional STA/LTA because of large background noise and overlapping arrivals from multiple events clustered in time. Here we found an M_L 3.7 earthquake missing in the catalog because it was buried in the coda of the mainshock.

Detection by waveform cross-correlation depends on the similarity of the template signal and waveform data which is controlled by focal mechanisms, propagation paths, and magnitudes of events. In general, aftershocks that occur on or near the mainshock fault plane have similar focal mechanisms. Separations between events in the aftershock cluster are small so that the propagation paths to seismic stations are nearly identical. The duration and complexity of the source time functions are mainly controlled by the event magnitude. In this study we band-pass filtered waveform data between 0.3 and 8 Hz, which are lower than the corner frequencies of earthquakes smaller than M_L 5. Therefore, the influences of event magnitudes on waveform shapes were avoided.

In order to detect events as small as possible, we only applied the SCC technique to the closest station. False detections were greatly reduced by applying the SCC to three-channel recordings simultaneously. Technically, the detection threshold and false detections can be further reduced by combining detection results from multiple stations, but lower signal-to-noise ratios at distant stations may reduce their contribution. We can stack the SCC coefficients of all stations to produce an "array" correlation beam [*Gibbons and Ringdal*, 2006]. However, such kind of array technique requires a dense network, especially for small aftershocks. This aspect will be investigated in future studies.

Our relocation results and moment tensor solutions suggest that the April 18, 2008 earthquake occurred on a left-lateral, strike-slip fault with an orientation of 292°. The newly discovered fault lies southwest of Mt. Carmel, IL (Fig. 3.7). Although its orientation differs significantly from the known NE-SW trend of

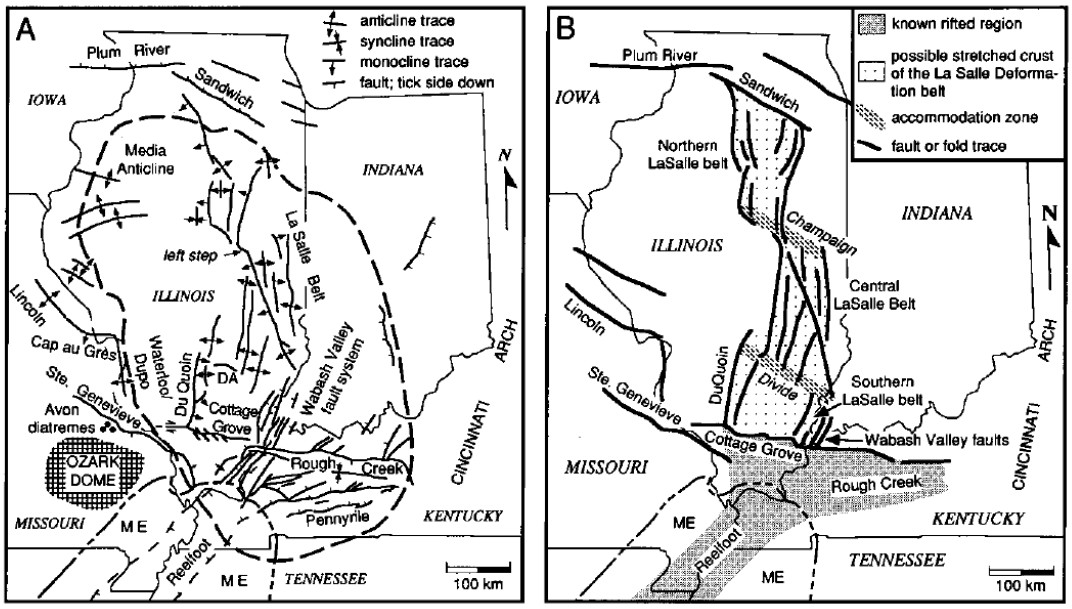

Figure 3.10: A: Simplified geologic map of Illinois basin region showing positions of principal structures. Heavy dashed line shows approximate edge of Illinois basin. ME: Mississippi embayment. B: Speculative map La Salle deformation belt, and its southern continuation, resembles map geometry of low-strain zone of crustal extension. Proposed left-stepping accommodation zones (Divide; Champaign) separate belt into three segments. After [*Marshak and Paulsen*, 1996].

normal faults in the region, the left-lateral strike-slip faulting is consistent with the E-W compressional stress field in the region [*Heidbach et al.*, 2008] (Fig. 3.1). *Marshak and Paulsen* [1996] proposed two NW-trending, left-stepping accommodation zones that divided the NE-trending La Salle deformation belt into the northern, central, and southern parts (Fig. 3.10). Our newly discovered fault coincides with the southern accommodation zone (Divide). In addition, we speculate that the earlier April 3, 1974 M_w 4.3 earthquake also occurred on this fault. Its focal mechanism [*Herrmann*, 1979] is similar to the moment tensor solutions of the April 18, 2008 earthquake sequence (Fig. 3.7). The seismicity on the fault indicate reactivation of old deformation zone by contemporary stresses.

3.6 Summary

In summary, we have developed a reliable and efficient method to detect small magnitude earthquakes using template events and waveform cross-correlation. We found more than 120 aftershocks in the first two weeks following the April 18, 2008, Mt. Carmel earthquake, more than three times the number reported by the permanent network with the traditional STA/LTA detector. We relocated 28 events by the double-difference relocation algorithm and found that these events were located on a nearly vertical plane striking WNW-ESE. By combining the relocation results with focal mechanism solutions, we conclude that the fault responsible for the April 18 earthquake is a left-lateral, strike-slip fault with an orientation of 292° and a dip angle of 81°. The fault coincides with one of the proposed left-stepping accommodation zones (Divide) in the La Salle deformation belt and indicates reactivation of old deformation zone by contemporary stresses in the Midcontinent.

Chapter 4: Shallow Low-Velocity Zone of the San Jacinto Fault from Local Earthquake Waveform Modelling

4.1 Geological settings of the San Jacinto fault zone

The San Jacinto fault is the most seismically active strand of the San Andrews fault system in southern California (Fig. 4.1), with successive occurrence of moderate earthquakes since 1890 [*Sykes and Nishenko*, 1984; *Sanders and Kanamori*, 1984]. No earlier large events were reported so far, but the historic catalog may be incomplete. At least 10 $M \geq 5.5$ earthquakes occurred on the SJF according to the Southern California Earthquake Center (Fig. 4.1). *Sanders and Kanamori* [1984] did an excellent review on estimating magnitudes and locations of the historic earthquakes in the region. The spatial distribution of these large earthquakes and instrumentally recorded small earthquakes defined a 20-km aseismic section near Anza, which is considered to be a seismic gap [*Thatcher et al.*, 1975]. The length of the Anza seismic gap implies potential for an M 6.5 event, similar to sizes of historic earthquakes in the region [*Sanders and Kanamori*, 1984].

The southern portion of the SJF near Anza is composed of three branches: the Buck Ridge fault (BRF); the Clark Valley fault (CVF); and the Coyote Creek fault (CCF). The geometries indicate a southeast-northwest narrowing of the fault zone from 11 km wide across the active BRF, CVF, and CVF to 1.5 km near Anza (Fig. 4.1). Study of sedimentary rocks in the Borrego Badlands, southern California, shows that the SJF was formed in the Pleistocene era, 1.0–1.1 Ma ago [*Lutz et al.*, 2006]. Geologic studies showed significant late Cenozoic right-lateral displacements implying the SJF played an important role in regional tectonics. The average slip rate on the SJF is approximate 12–15 mm/yr based on studies of Pleistocene and Holocene alluvial fans and fluvial deposits, Bautista deposits, and the modern GPS measurements [*Sharp*, 1967; *Rockwell et al.*, 1990; *Becker et al.*, 2005].

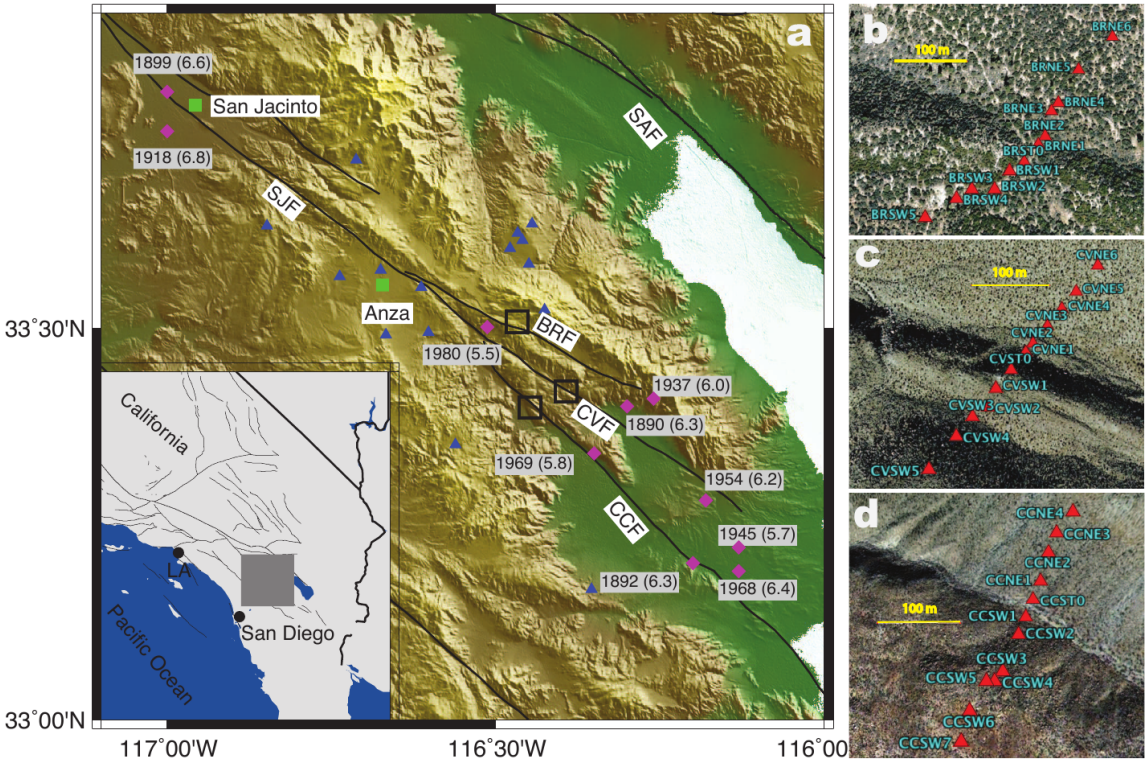

Figure 4.1: a: Map showing the San Jacinto fault zone (SJFZ) and locations of nearby major historic earthquakes (diamonds, with year and magnitude indicated). The southern segment of the fault splits into three branches: the Buck Ridge branch (BRF), Clark Valley branch (CVF), and Coyote Creek branch (CCF). Three linear seismic arrays were deployed across these branches as shown by black squares. Blue triangles represents seismic stations of the Anza network. The inset map shows location of study area (shadowed area) and major faults in California (black lines). b: A closeup view of geometry and local topography of the BRF array obtained from GoogleEarth. c: the CVF, and d: the CCF array.

By modelling FZ trapped waves a 150–200-m-wide LVZ of the SJF was proposed with 25–40 per cent V_s reduction [*Li et al.*, 1997; *Li and Vernon*, 2001; *Lewis et al.*, 2005]. However, the depth extent of the LVZ is still under debate. A 15–20-km-deep LVZ of the SJF was reported by *Li and Vernon* [2001] while another group using the same dataset argued that it was only 3–5 km deep [*Lewis et al.*, 2005].

4.2 The 1999 San Jacinto fault zone seismic experiment

In 1999, three linear seismic arrays were deployed across the three fault strands (Fig. 4.1). Each array was 350 m in length and consisted of 12 three-component L22 2 Hz short-period instruments. The profiles were approximately perpendicular to the surface trace of the fault (Fig. 4.1). Array A across the CVF and array B across the BRF lasted for 2 months while array C across the CCF was deployed for 4 months in the field. Waveforms of ∼1500 small earthquakes were recorded by the arrays during operation period. More details of the experiment were described in *Li and Vernon* [2001].

4.3 Data analysis and results

4.3.1 FZ dip based on P-wave arrival times

We selected events that were relocated by *Shearer et al.* [2005]. We required that events were within 10 km in epicentral distance of the seismic array and were recorded by at least 7 stations of the arrays. There were 52 such events for the BRF array, 41 for the CCF array, and only 5 for the CVF array. We removed instrument responses and band-pass filtered the ground velocity waveforms between 1 and 15 Hz. We then hand picked direct P- and S-wave arrival times for each event.

Fig. 4.2 shows three-component seismograms from one earthquake recorded by the BRF array. The event is located southwest of the surface fault trace (Fig. 4.3a). Usually the LVZ associated with a fault zone causes the P and S waves to arrive later at stations on the other side of the fault. However, Fig. 4.2 shows that the direct P and S waves arrived earlier at northeastern stations than at the southwestern stations. This indicates that the LVZ is not vertical but dips to the southwest so that the event is actually located on the northeastern side of the LVZ (Fig. 4.3b).

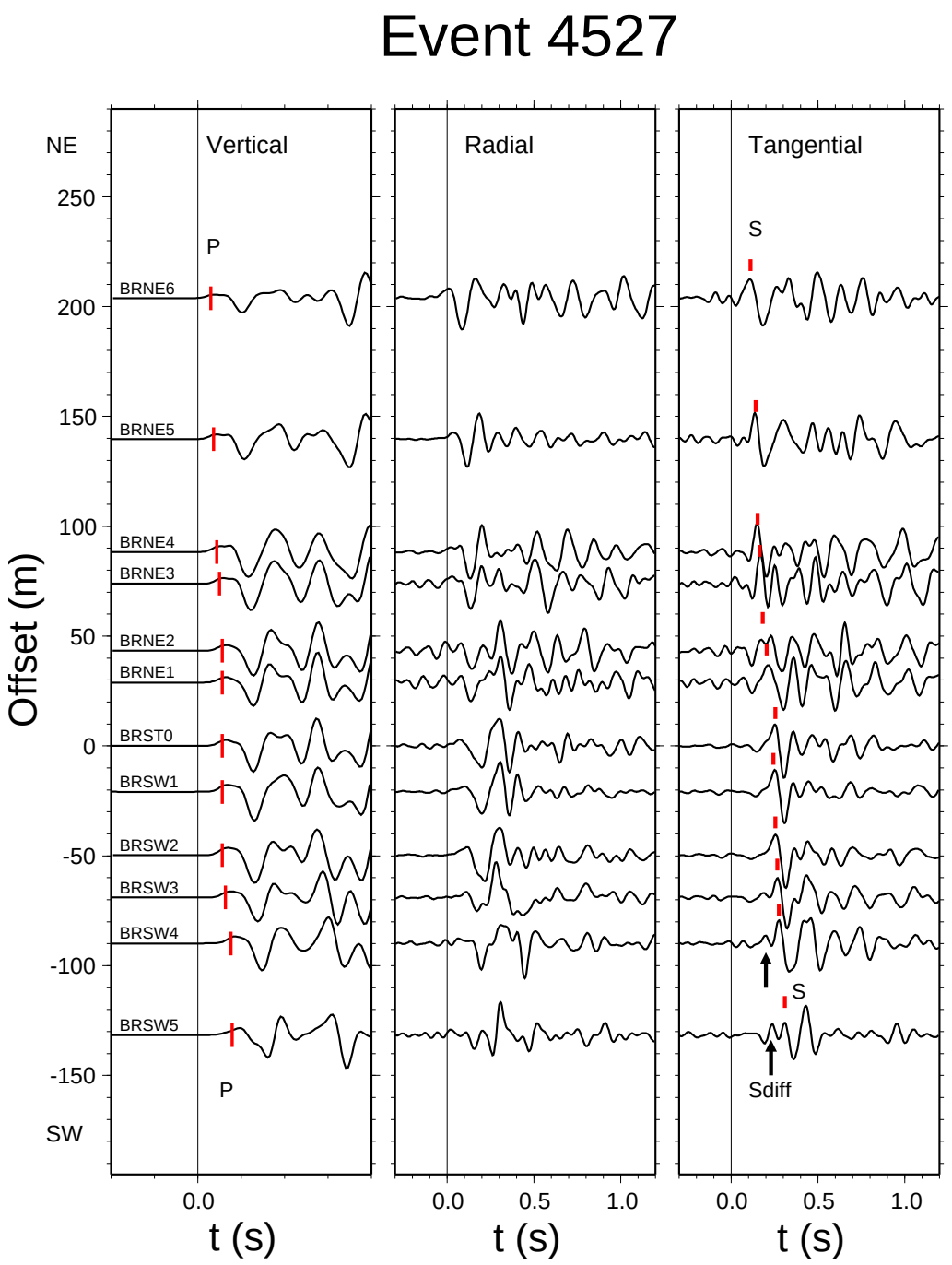

Figure 4.2: Three-component seismograms of event 4527 recorded by the seismic array across the BRF. From left to right are vertical component in P window, radial, and horizontal components in S window. The Y axis stands for the offset from the central station of the array from southwest to northeast. Red bars represent the hand-picked P- and S-wave arrival times. Black arrows point to the diffracted S-wave phases before the direct S waves.

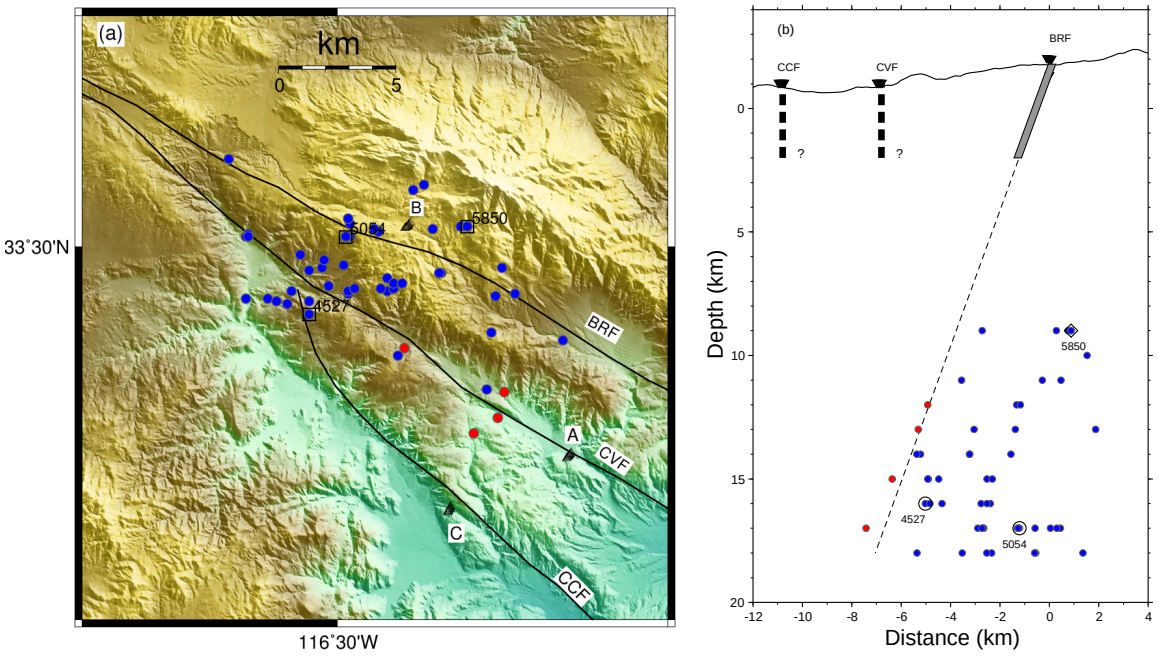

Figure 4.3: Map view (a) and cross-section (b) of locations of events recorded by the BRF array. Blue and red colors represent positive and negative P-wave travel time differences between the northeastern-most and southwestern-most stations of the array, respectively. For those events whose waveforms are shown in the paper, event numbers are marked on their locations. The grey bar represents the extent of LVZ of BRF. Thick dashed lines stand for LVZs of the CCF and the CVF.

In Fig. 4.3 we show event locations and the P arrival time differences between the northeastern-most and southwestern-most stations of the BRF array. Out of 52 events, only four events located south of the array show early P arrivals at southwestern stations, i.e., on the southwestern side of the LVZ. The rest are located on the northeastern side of the LVZ. This allowed us to determine the dip of the LVZ in the cross-section perpendicular to the strike of the BRF (Fig. 4.3b). The best-fit plane shows that BRF dips 70° to the southwest. Using the same analysis we found that CCF is nearly vertical. The dip of CVF could not be determined due to lack of events.

Since we constrained the LVZ dip by the spatial locations of earthquakes, the uncertainty of event locations must be considered in determination of the LVZ dip. In this study, most event locations have relatively small uncertainties both laterally

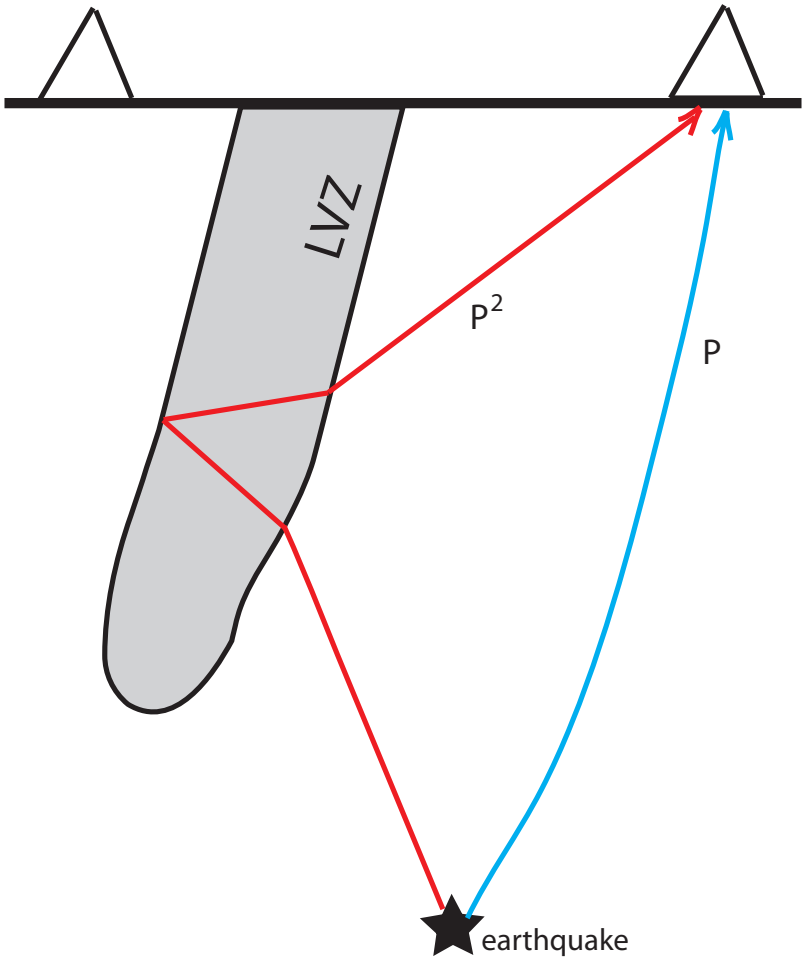

Figure 4.4: A sketch showing the direct (blue) and the LVZ-reflected (red) P waves from an earthquake (star) to station (triangle). LVZ: low velocity zone.

and in depth, usually less than 1 km [*Shearer et al.*, 2005]. We applied 1 km perturbation to event locations and found the uncertainty of the corresponding LVZ dip was less than 5°. Therefore, we concluded that the BRF dips 70±5° to the southwest.

4.3.2 FZ widths and velocity drops

Recently, we developed a technique to determine high-resolution FZ structure using arrival times and waveforms of FZ transmitted and reflected P and S body waves from local earthquakes [*Li et al.*, 2007]. As shown in Fig. 4.4, a LVZ that

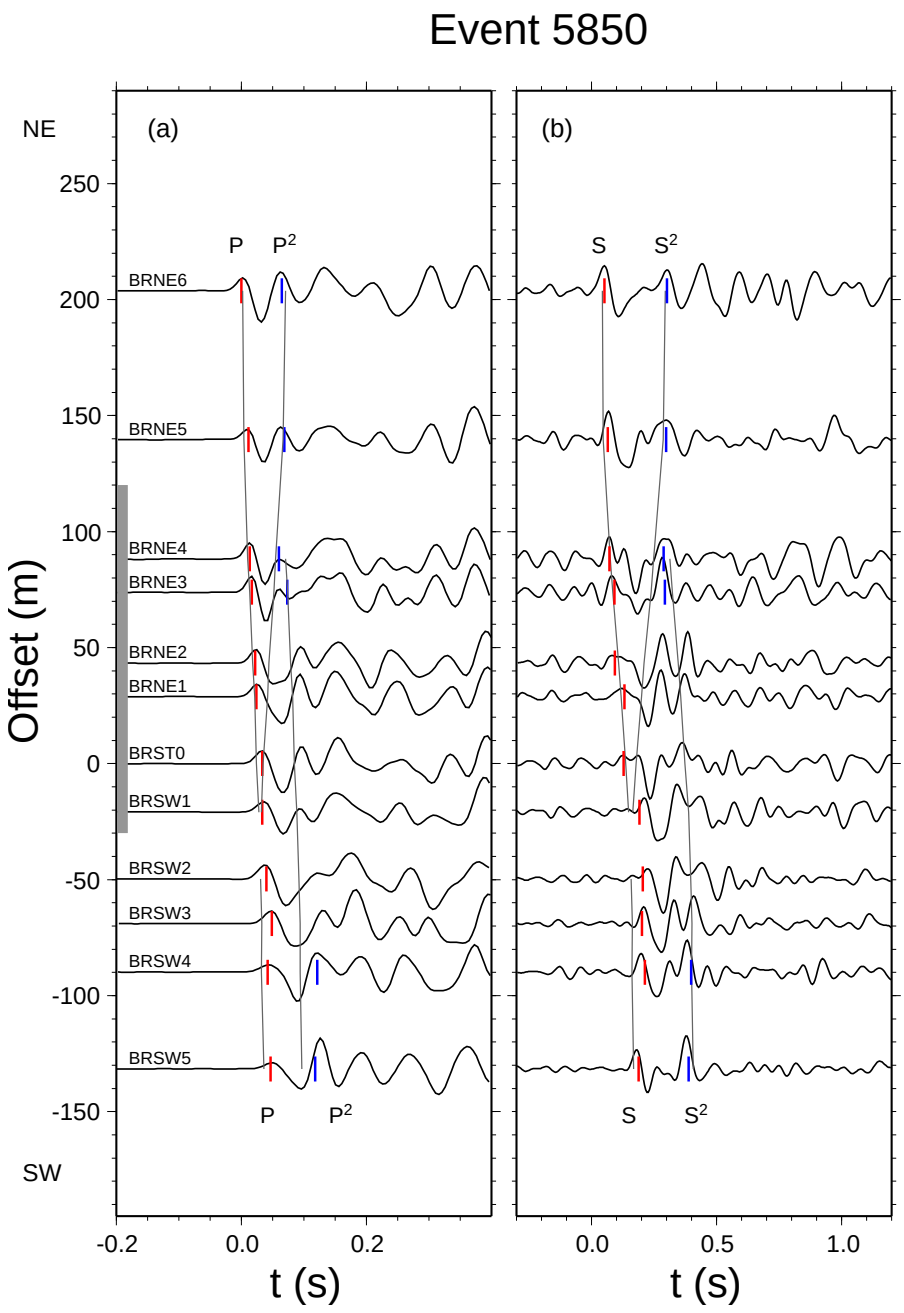

Figure 4.5: Waveform record section of, from left to right, the FZ radial component in P window and the FZ parallel component in S window for event 5850 located in the east of the BRF (Fig. 4.3). The horizontal axes show time after P arrival at station BRST0 for the radial component and after S arrival for the FZ parallel components. Red vertical bars represent direct P- and S-wave arrival times and blue bars denote available FZ-reflected-wave arrivals (P^2 and S^2). The lines represent predicted arrival times of direct P or S wave and its multiple FZ reflected phases. Vertical grey bar represents location of the LVZ.

embedded into a uniform half space can generate the LVZ-reflected body waves for an event near the FZ. When the event is close to the FZ, the differential times between the direct and LVZ-reflected P and S waves can be expressed as:

$$P^n - P = nw\sqrt{V_p^{-2} - p^2}, \tag{4.1}$$

$$S^n - S = nw\sqrt{V_s^{-2} - p^2}, \tag{4.2}$$

where p is the ray parameter and n is the number of ray legs of the multiple reflection in the FZ. This technique has been successfully applied to the Landers fault zone using aftershock data of the 1992 Landers earthquakes. Using the new technique, the trade-off between the FZ width and velocity drops is greatly reduced as we have shown in a Monte Carlo experiment in which we applied perturbation to event location, FZ strike, and FZ dip [*Li et al.*, 2007]. However, limitations of this technique have to be pointed out as well. We have to ignore the depth-dependent variations for host rock and the LVZ since we compute synthetics by generalized ray theory [*Helmberger*, 1983] using a 1-D model. In order to constrain on the LVZ depth, we need to use the finite-difference technique.

We first rotated three component seismograms into the FZ radial, FZ normal, and FZ parallel directions (see details in *Li et al.* [2007]) using the FZ dip determined above and FZ strike following the surface trace (Fig. 4.3). Fig. 4.5 shows a waveform record section from an earthquake located on the northeastern side of the BRF fault trace. A notable feature of the record section is that arrival times of direct P and S waves are delayed by ∼0.05 s and ∼0.2 s, respectively, from the northeastern-most to the southwestern-most stations. The delay starts near station BRNE4 and ends near BRSW1, over a distance of ∼150 m, indicating existence of a LVZ with its northeastern boundary near BRNE4 and southwestern boundary near BRSW1 that allows us to constrain the LVZ width to be 150 m. The LVZ is not

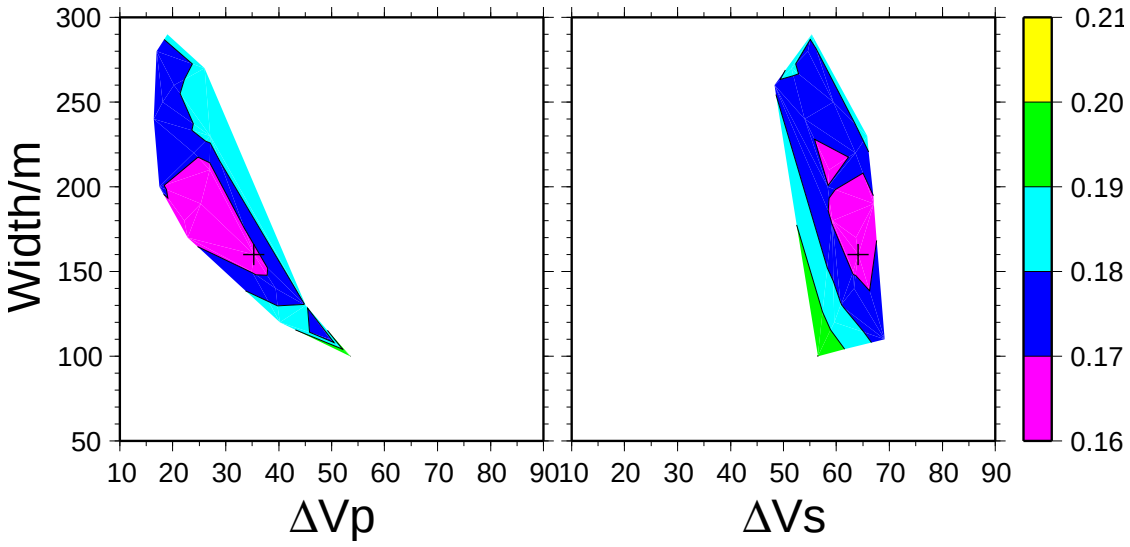

Figure 4.6: FZ width and P- and S-wave velocity drops as determined by least-square inversions of direct and FZ-reflected P and S waves for event 5850. Travel time residuals are shown by color contour and black crosses represent minimum points.

centered at the surface trace (location of station BRST0), but is shifted to the northeast by ∼50 m. In addition, we identified the FZ-reflected P and S waves at some stations (labeled P^2 and S^2 in Fig. 4.5). The time delays of the FZ-reflected waves relative to the direct arrivals were used to determine the velocity drops of the LVZ compared to the host rock. We fixed the V_p of host rock to be 6.3 km s^{-1} and the V_s to be 3.6 km s^{-1}. The best-estimated LVZ P-wave velocity drop is 30–40 per cent and S-wave velocity drop is 50–60 per cent using a least-square inversion of direct and FZ-reflected P and S arrival times (Fig. 4.6). The predicted arrival times of the direct and FZ-reflected waves using the best LVZ model are shown in Fig. 4.5.

4.3.3 Constrain on LVZ depth by S_{diff} waves

One interesting feature we found in Fig. 4.2 is a precursor before the direct S wave. It only appears at stations on the southwest side of the array and its amplitude decreases at stations close to the FZ (Fig. 4.2). From FZ wave synthetic tests in the Lander FZ study [*Li et al.*, 2007], we showed that the precursors are

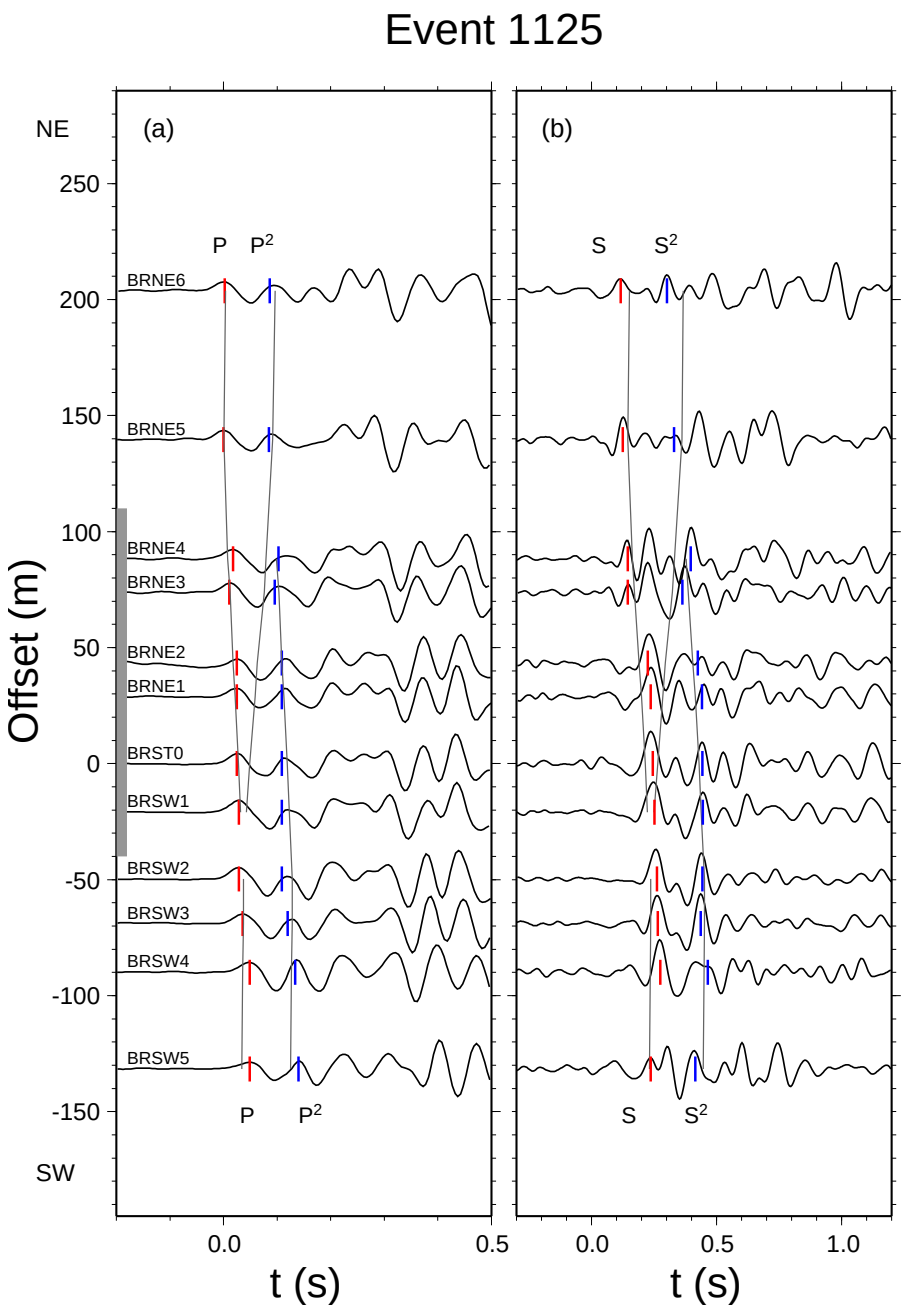

Figure 4.7: Same to Fig. 4.5.

diffracted S waves (S_{diff} hereafter) (Fig. 4.8). We also found that the occurrence and amplitudes of LVZ-diffracted wave depend on the LVZ depth [*Li et al.*, 2007]. Therefore, it could be used to constrain the LVZ depth. In this section we show the possibility of determining the LVZ depth by modelling the S_{diff} waves.

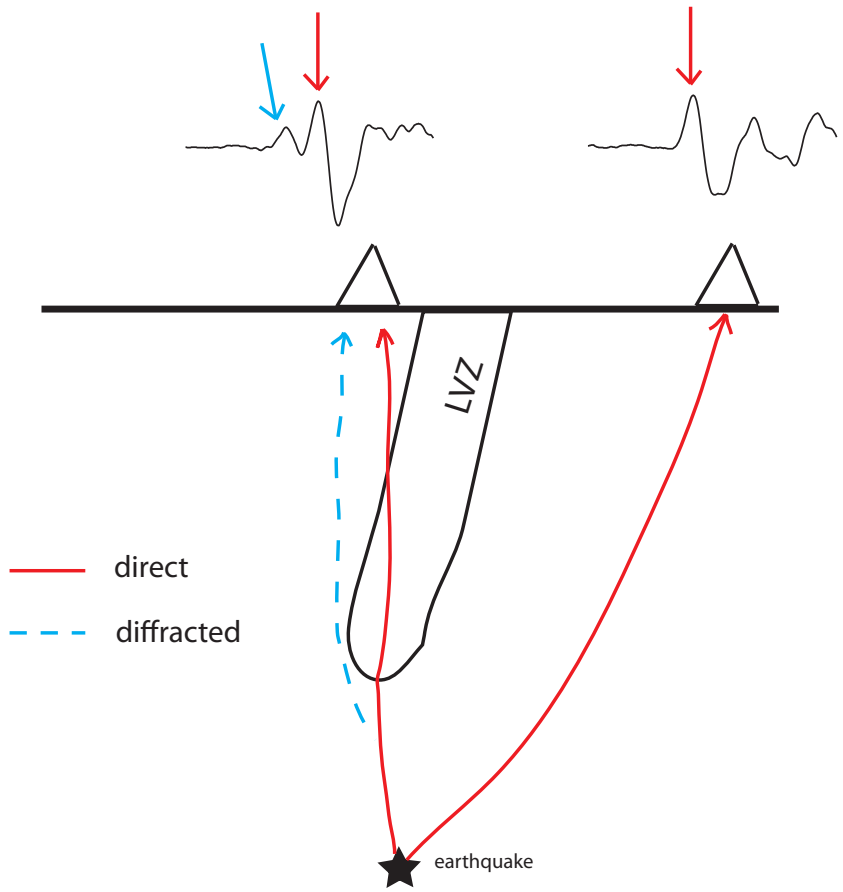

Figure 4.8: Direct (red) and diffracted (blue) waves from an earthquake (star) arrive at two stations (triangles). Two seismograms are shown on the top of stations with red and blue arrows pointing to the direct and diffracted waves. LVZ denotes a low velocity zone embedded into a half space.

First we set up a hypothetical array of 500-m-long with a 20-m spacing across a 200-m-wide LVZ. The LVZ has a north-south orientation and dips 70° to the west (Fig. 4.9a&b). It extends down to a depth of 2 km and has a 50 per cent reduction in V_s and a 40 per cent reduction in V_p. The western boundary of the LVZ is located 40 m west of the center station. Attenuation in the LVZ is set as Q_s=10 and Q_p=40 (model 1 in Table 4.1). The earthquake is located 2.5 km west of the center station and its depth is 15 km (Location *a* in Fig. 4.9a&b). We computed synthetic waveforms by the finite-difference technique with a grid size of 30 m and time step of 0.002 s. The maximum signal frequency is 12 Hz. Synthetic waveforms of the

transverse component are shown in Fig. 4.9d. S_{diff} waves appear at the western-side stations of the array. Their amplitudes relative to S waves decrease towards the FZ and eventually vanish at stations inside the LVZ (Fig. 4.9d).

We then computed synthetic waveforms for the same event location but for two other different LVZ models of different depths (model 2 and 3 in Table 4.1) to

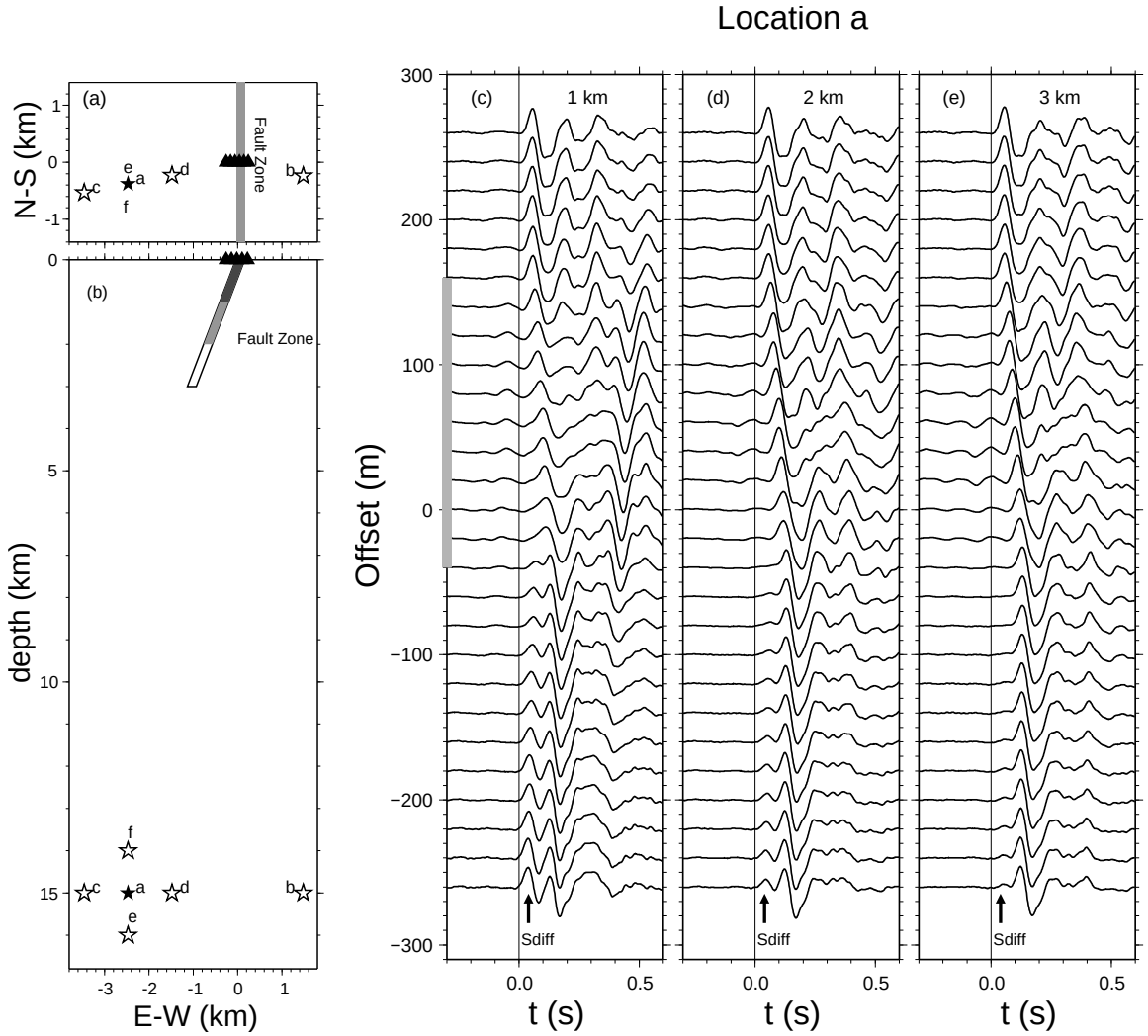

Figure 4.9: (a) Locations of a seismic array (triangles) across a 200-m-wide, N-S oriented, and 20° dipping fault zone. Stars denote possible locations of an earthquake. (b) The cross section perpendicular to the FZ strike. Dark grey, grey, and white bars represent different LVZ depths. (c), (d), and (e) Synthetic waveforms of transverse component seismograms corresponding to fault zone depths of 1 km, 2 km, and 3 km. Black arrows point out the S-diffracted waves. Event locates at a position in (a) and (b).

Table 4.1: Different fault zone models used in synthetic test.

M#	Dip (°)	ΔV_s (%)	ΔV_p (%)	*Depth* (km)	*Width* (m)	Q_p	Q_s
1	110	50	40	2	200	40	10
2	110	50	40	1	200	40	10
3	110	50	40	3	200	40	10
4	110	25	40	2	200	40	10

demonstrate the sensitivity of the S_{diff} to LVZ depth. The two LVZ models have same parameters as the first model but their depths are increased and decreased by 1 km, respectively. We compared synthetic waveforms for different LVZ depths and found that the S_{diff} waveforms changed noticeably (Fig. 4.9c&e). The S_{diff} are visible at the western stations for all the models. However, their amplitudes relative to the S wave are quite different. For the LVZ of 2 km deep, the amplitudes of S_{diff} are slightly smaller than S wave (Fig. 4.9d). When the LVZ depth is decreased from 2 km to 1 km, the S_{diff} are very strong and have larger amplitude than the S wave at most western stations (Fig. 4.9c). In comparison, we only observed very weak S_{diff} when the LVZ depth is 3 km. The S_{diff} are only visible at several stations away from the LVZ (Fig. 4.9e). From these results, we conclude that we are able to resolve the LVZ depth reliably within 1 km, provided that we know the location of the event accurately.

In this study, we selected events located by *Shearer et al.* [2005]. Most event locations have relatively small uncertainties both laterally and in depth, usually less than 1 km. But if combined with uncertainties of other FZ parameters, the event location uncertainties could result in large uncertainties of LVZ depth [*Li et al.*, 2007]. To consider the effect of event location uncertainties, we perturbed the event location by 1 km in depth and epicentral distances (Table 4.2). At each perturbed location, we find the best fit LVZ depth by comparing the "un-perturbed" waveforms and synthetic at the perturbed event location. Fig. 4.10a shows that the best fit for event location f gives a LVZ of 2 km deep, same as the "true" depth.

Table 4.2: Best fit LVZ depth corresponding to event locations.

Eve loc	Δ (km)	θ (°)	h (km)	d (km)
	epicentral distance	back azimuth	event depth	LVZ depth
a[1]	2.5	261	15	2
b	1.5	100	15	N/A
c	3.5	261	15	3
d	1.5	261	15	1
e	2.5	261	16	2
f	2.5	261	14	2

We performed the same procedure for a shallow event depth (location e in Fig. 4.9a&b) and found the the best-fit LVZ depth is also 2 km. Therefore, we believe that the uncertainties of event depths has little effects on the LVZ depth by modelling the S_{diff} waves.

As we applied perturbation on the event epicentral distance, we found that the obtained LVZ depth was more sensitive to the lateral uncertainty of event location. We modeled the LVZ depth with the earthquake epicentral distance increased by 1 km (location c in Fig. 4.9a&b). The best-fit LVZ depth is 3 km (Fig. 4.10b), 1 km larger than the "true" depth. In addition, we found the best-fit LVZ depth is 1 km for the event epicentral distance decreased by 1 km (location d in Fig. 4.9a&b). Therefore, we conclude that uncertainty of LVZ depth using S_{diff} is $\sim$1 km if uncertainties of event locations are $\sim$1 km.

Using the FZ dip, width and velocity reduction determined earlier, we computed synthetic waveforms for LVZ models with different depths by the finite-difference technique. Fig. 4.11 shows waveform fits of the transverse component for two events. The best-fit LVZ depth is 2 km and its uncertainties are estimated as 1 km assuming that uncertainties of event locations are no more than 1 km.

4.4 Discussion

In this study, we investigated the SJFZ structure near Anza, southern California, by modelling local earthquake waveforms recorded by three temporary

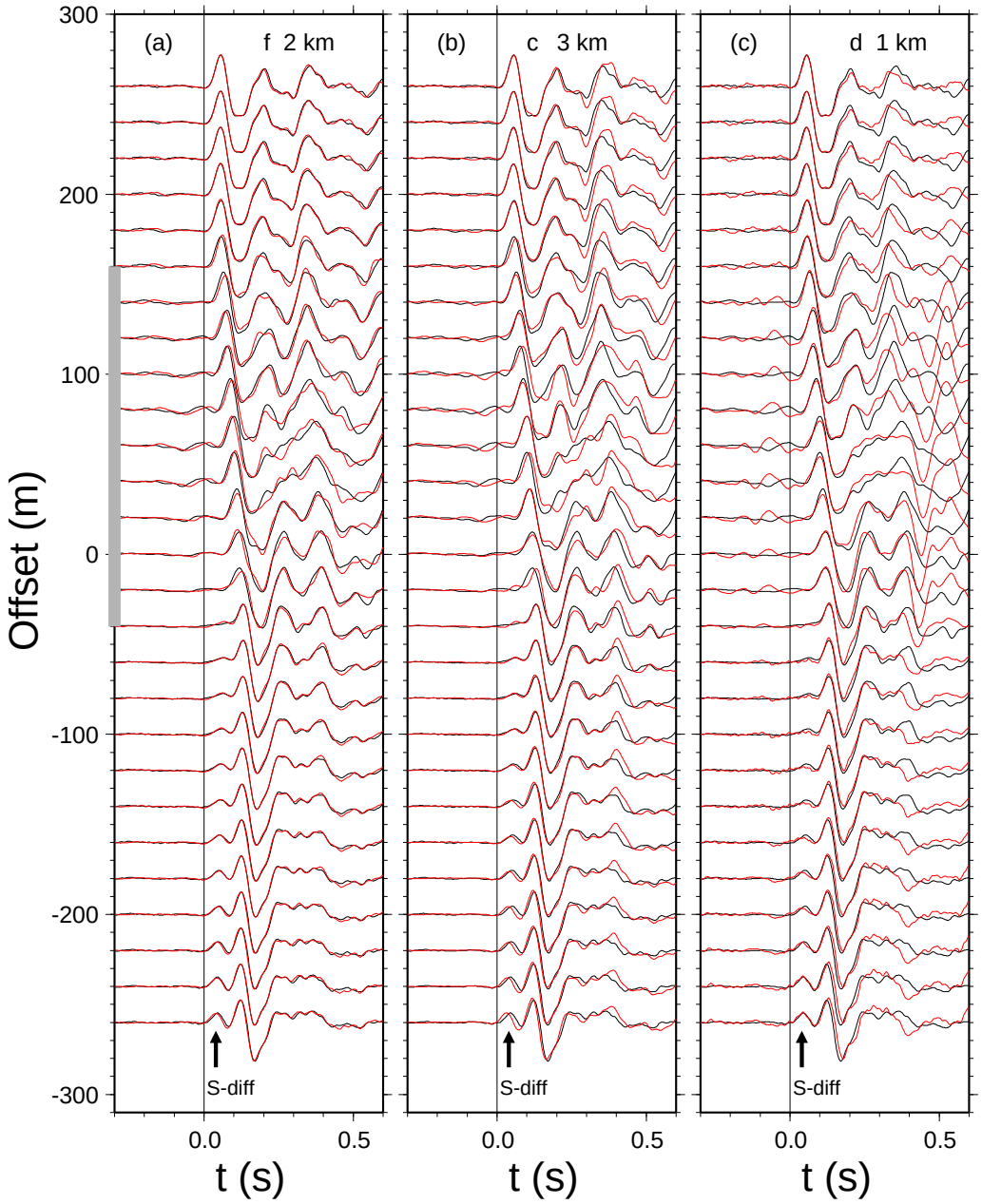

Figure 4.10: Black are synthetic seismograms representing the "data" for an earthquake located at a in Fig. 4.9a&b and the FZ model No. 1 in Table 4.1. Red traces are synthetic seismogram for earthquakes located at (a) f, (b) c, and (c) d in Fig. 4.9a&b. At each location, the best fit LVZ depth is (a) 2 km, (b) 3 km, and (c) 1 km. Black arrows point to the S-diffracted phases.

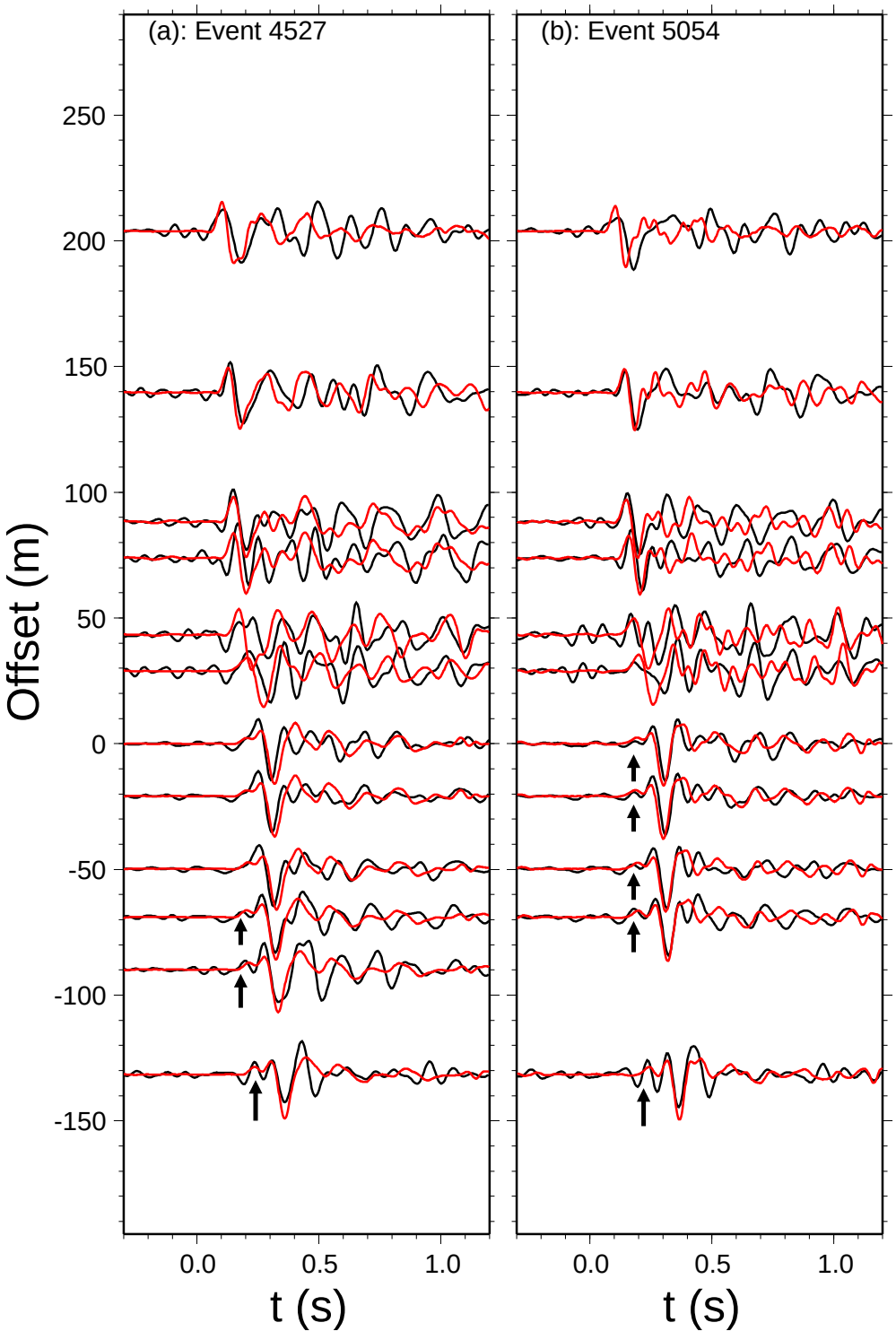

Figure 4.11: S and S_{diff} wave data (black) and synthetic waveforms (red). From left to right, two events, (a) 4527, (b) 5054, recorded by the BRF array. Event locations are shown in Fig. 4.3b. Black arrows point to the S_{diff} phase.

arrays. We found that the LVZ of the BRF has a width of ∼150 m, dips 70° southwestward, is reduced 50–60 per cent in V_s and 30–40 per cent in V_p, and extends ∼2 km in depth. The width is consistent with results of previous studies [*Li et al.*, 1997; *Li and Vernon*, 2001; *Lewis et al.*, 2005]. The FZ dip agrees with results of analyzing locations of earthquakes with FZ trapped waves [*Li and Vernon*, 2001]. The *S*-wave velocity reduction is slightly higher than those from the FZ trapped wave study [*Li and Vernon*, 2001; *Lewis et al.*, 2005]. The LVZ is not centered at the surface trace of the BRF but is shifted to the northeast by ∼50 m, which was also found by the FZ trapped wave study [*Lewis et al.*, 2005]. We interpret the LVZ to be the cumulative damage zone caused by ruptures of repeated earthquakes in the region over geological time. The SJFZ is seismically active; a few moderate to large magnitude earthquakes occurred since 1890. Mechanisms to reduce seismic wave velocities in the damage zone could include intense fracturing and pulverization, brecciation, and fluid saturation [*Chester et al.*, 1993]. Our results show significant higher reduction in V_s than in V_p, suggesting that fluid saturation might be the main mechanism because it affects V_s more than V_p.

A central issue in FZ imaging is the depth extent of the low-velocity waveguide zone. One group suggested that it penetrates down to the base of the seismogenic zone [e.g. *Li et al.*, 1994, 2000; *Li and Vernon*, 2001; *Li et al.*, 2004], while others argued for a shallow trapping structure extending only to a depth of 3–5 km [e.g. *Ben-Zion et al.*, 2003; *Peng et al.*, 2003; *Lewis et al.*, 2005]. A recent numerical analysis of FZ trapped wave pointed out that determination of fault structure at seismogenic depth requires analysis of data at higher frequencies than the FZ trapped wave [*Wu et al.*, 2008]. In this study, we used precursors before the direct *S* waves, the S_{diff} waves, which are sensitive to LVZ depth [*Li et al.*, 2007]. They were used to study some fracture models [*Grad*, 1984], but have not been used to image LVZ depth so far. Our synthetic tests show that the S_{diff} waves are suitable

to determine LVZ depth because their relative amplitudes to the direct S waves are very sensitive to depth of the LVZs. Our modelling results show that the LVZ of the BRF extends 2 km in depth that is consistent with the proposed shallow structure of *Lewis et al.* [2005]. The depth uncertainties are estimated by the synthetic tests in which we believe the uncertainties of FZ depth are in the same order with the uncertainty of event locations (especially in lateral distance). Since most event locations used in this study have uncertainties less than 1 km [*Shearer et al.*, 2005], we believe the uncertainties of the LVZ depth of the BRF is less than 1 km.

During our waveform modelling and synthetic tests, we assumed that the FZ was a simple tabular layer embedded in a half space. The newly developed technique [*Li et al.*, 2007] could take into account the effect of gradational reduction of seismic velocities from host rock to the LVZ. However, it would not significantly affect the waveforms if the velocity gradient happens in a very narrow zone compared to the LVZ itself. In addition, the FZ structure is not variant with depth. However, most FZs are not that simple and their properties are depth dependent. For instance, the Calico fault zone in California has a depth-dependent velocity reduction, 50 per cent reduction in V_s down to 5 km and gradually changed to 25 per cent from 5–10 km [*Cochran et al.*, 2009]. We could not exclude the case that the LVZ of the BRF extends to 2 km in depth with a 50–60 per cent reduction in V_s and extends further down with much smaller velocity contrast or width. For example, *Hong and Menke* [2006] suggested that low shear velocities of 6–8 per cent in the San Jacinto fault zone were observed down to a depth of $\sim$16 km. We performed a synthetic test for a FZ model with 25 per cent reduction in V_s (model 4 in Table 4.1). The model grid size was set to 30 m which corresponds to 15 Hz in signal frequency. We did not observe any diffracted waves. In order to resolve fine structure, we had to compute with smaller grid size to get higher frequency which requires much longer CPU time and larger memory usage.

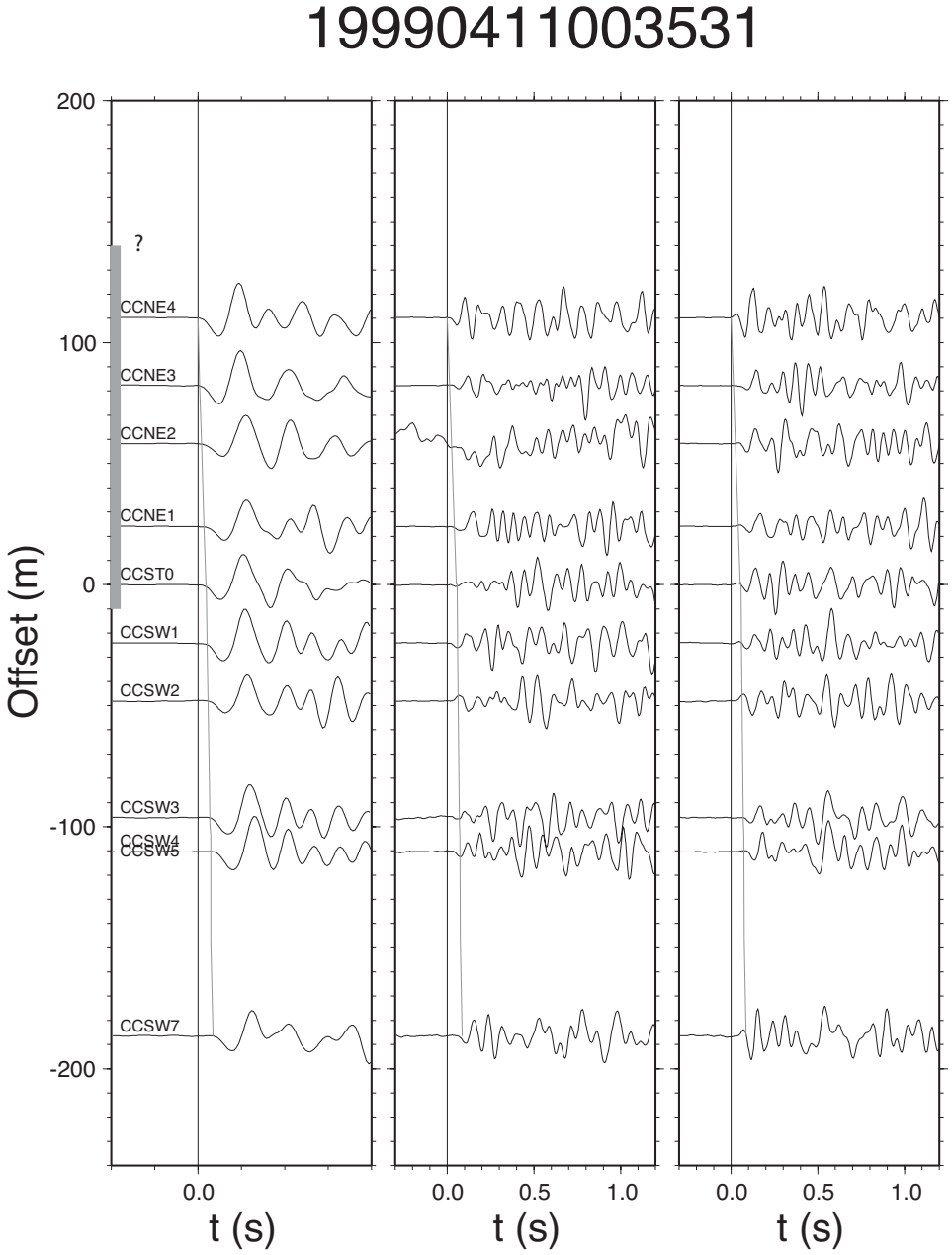

Figure 4.12: Three-component seismograms of event 3531 recorded by the seismic array across the CCF. Same to Fig. 4.5, from left to right are vertical component in P window, radial, and horizontal components in S window. The Y axis stands for the offset from the central station of the array from southwest to northeast. Lines represent predicted arrival times from the obtained model. Thick grey line shows location of the LVZ.

We did not find a clear signature of LVZ-reflected waves for the CVF and the CCF branches (Fig. 4.12). Based on travel time modelling alone, we estimated that the CCF has a LVZ of ∼150 m in width and of 50 per cent reduction in V_s and 25 per cent reduction in V_p. The LVZ of the CVF is ∼200 m in width and has 50 per cent reduction in V_s and 40 per cent reduction in V_p. The results are consistent with the previous studies [*Li and Vernon*, 2001; *Lewis et al.*, 2005]. However, there might be a strong trade off between the LVZ width and velocity drop because we did not have constraint from FZ-reflected waves.

4.5 Summary

In summary, we investigated fine structure of the SJFZ near Anza, southern California, by modelling high frequency body waves. We found that the LVZ associated with the BRF is ∼150 m in width and has a 30–40 per cent reduction of V_p and a 50–60 per cent reduction of V_s. The BRF is dipping 70° southwest and its depth extent is 2±1 km. It is not centered on the surface fault trace but is shifted ∼50 m to the northeast, implying the assymetric damage during earthquakes.

Chapter 5: Seismic Structures of the Calico Fault Zone

5.1 Geologic settings of the Calico fault

The Calico fault is located in the eastern California shear zone (ECSZ) which accounts for 9-14 per cent of the total shear movement along the Pacific-North American transform boundary since ∼10.6 Ma [*Dokka and Travis*, 1990; *McClusky et al.*, 2001]. It is one of a family of dextral faults that traverse the Mojave Desert portion of the ECSZ and has accumulated ∼10 km of dextral slip since its inception [*Oskin et al.*, 2007]. Initiation of movement along the fault likely occurred between ∼10 and 6 Ma, and was probably related to Pacific-North American plate interaction [*Dokka and Travis*, 1990]. A recent study has determined the average slip rate of the Calico fault as 1.4-1.8 mm/yr by mapping Pleistocene alluvial fan deposits and $^{40}Ar/^{39}Ar$ dating [*Oskin et al.*, 2007]. The northern portion of the Calico fault connects to the Blackwater fault and ends in the south of the northeast trending Garlock fault. The southern portion of the Calico fault lies between the ruptured faults of the 1992 M_w 7.3 Landers and the 1999 M_w 7.1 Hector Mine earthquakes (Fig. 5.1). It suffered anomalous strain at least twice as its host rock moved during these two earthquakes [*Fialko et al.*, 2002; *Simons et al.*, 2002].

Compared to the adjacent Landers fault zone and the Hector Mine earthquake ruptured zone, there was much lower seismicity along the Calico fault since 1984 (Fig. 5.1). Moderate to large magnitude earthquakes ($M_w > 4.7$) in southern California can be dated back to 1800 but few events were generated along the Calico fault [*Wang et al.*, 2009]. Paleoseismic study along the Calico fault is sparse and no significant earthquake has been reported to be associated with the fault. A recent study in the northern Calico fault revealed four surface ruptures in which two of them occurred in Pleistocene and the other two were in Holocene [*Ganev et al.*, 2007]. The damage zone (or the LVZ) of the Calico fault zone was estimated to be

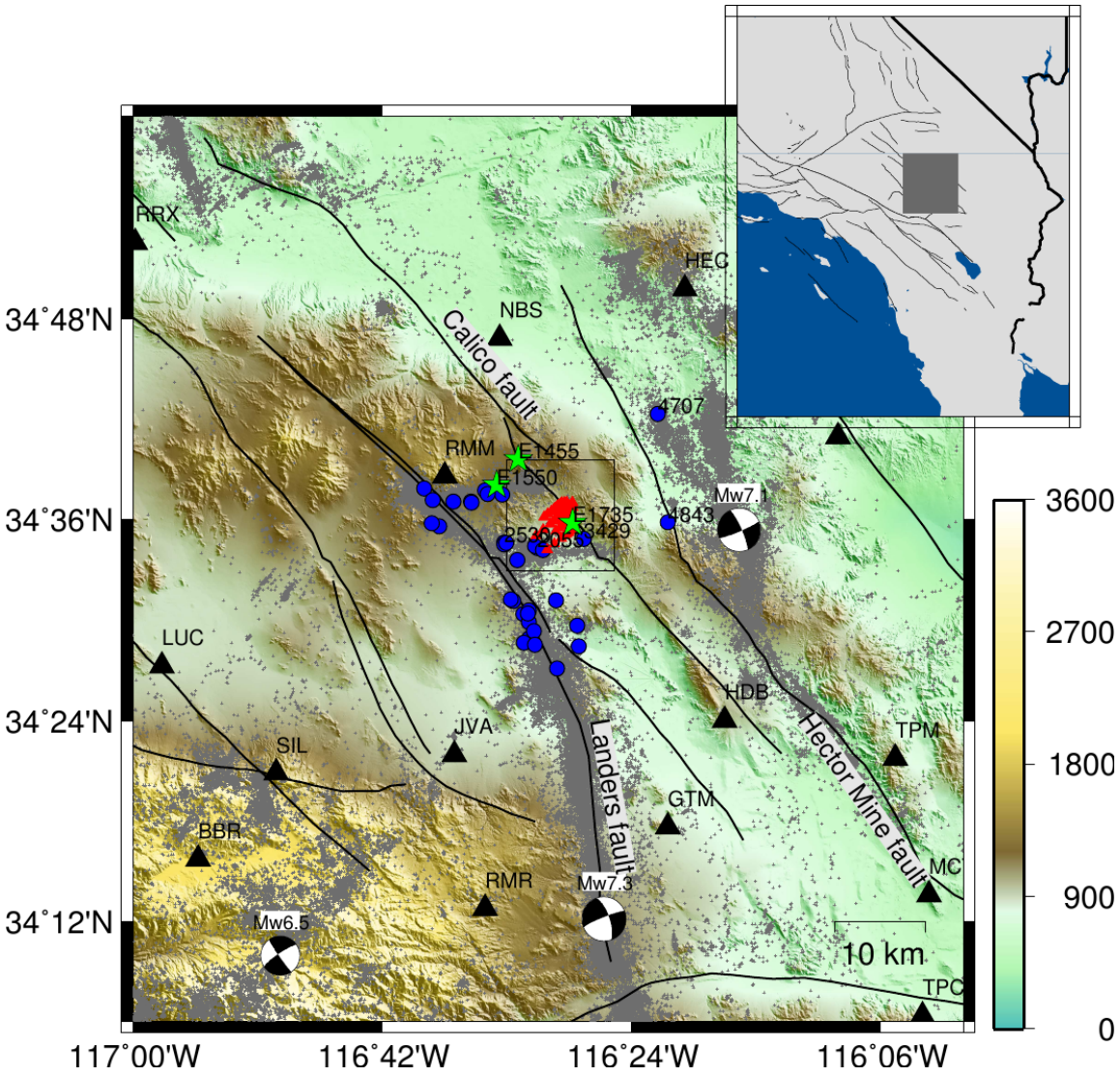

Figure 5.1: Blue dots represent local earthquakes and green stars are shots recorded by the temporary array (red triangles) across the Calico fault zone. Black lines stand for the mapped faults in the region. Black triangles are the southern California earthquake network seismic stations. Color denotes the local topography in meters. Gray crosses are the epicenters from 1981 to 2005. Inset map show locations of study area.

1.5-2 km wide with 50 per cent reduction in S wave velocity and elastic moduli based on FZ trapped wave and high resolution InSAR data [*Cochran et al.*, 2009; *Fialko et al.*, 2002]. The depth extent of the LVZ was constrained as ∼5 km from FZ trapped wave modelling of one single event. However, there is a considerable

trade-off between the width and velocity contrast of the LVZ by FZ trapped wave modelling [*Peng et al.*, 2003; *Lewis et al.*, 2005]. Moreover, it is still under debate whether the trapped energy penetrates down to the seismogenic depth (10–15 km) [*Li et al.*, 1994, 2000; *Li and Vernon*, 2001; *Li et al.*, 2004] or is generated in a shallow (3–5 km) basin-like structure [*Ben-Zion et al.*, 2003; *Peng et al.*, 2003; *Lewis et al.*, 2005]. Here we will use our newly developed technique, which can reduce the trade-offs among FZ parameters and determine the LVZ depth by using high-frequency body waves [*Li et al.*, 2007; *Yang and Zhu*, 2010], to probe fine structure of the Calico fault zone.

5.2 The 2006 Calico fault zone seismic experiment

To investigate the Calico fault zone structures, *Cochran et al.* [2006] installed a dense array of 100 seismometers in June 2006, including 40 intermediate-period (40T) sensors and 60 short-period (L22) sensors, in a 1.5 km $\times$ 5.5 km grid adjacent to the Calico fault (Fig. 5.2). These instruments were deployed along four lines perpendicular to the surface trace of the Calico fault, labeled A, B, C, and D in Fig.5.2. Due to lack of permission, the array did not extend farther northeast. The B profile is $\sim$5.5 km in length, the longest one in the array. The instruments recorded continuously in the field for 6 months. During the first week of deployment they detonated three shots: one in the fault zone within the array, the second in the fault zone approximately 6 km from the array, and the third outside of the fault zone, also about 6 km away (Fig. 5.1). The shot sizes ranged from 500 to 1200 lbs and were detonated at a depth of 90-120 ft. Table 5.1 lists all information for the shots. All the local events, including the shots, were collected for a FZ trapped wave study. Travel times of the regional and teleseismic events were used to model the Calico FZ structure [*Cochran et al.*, 2009].

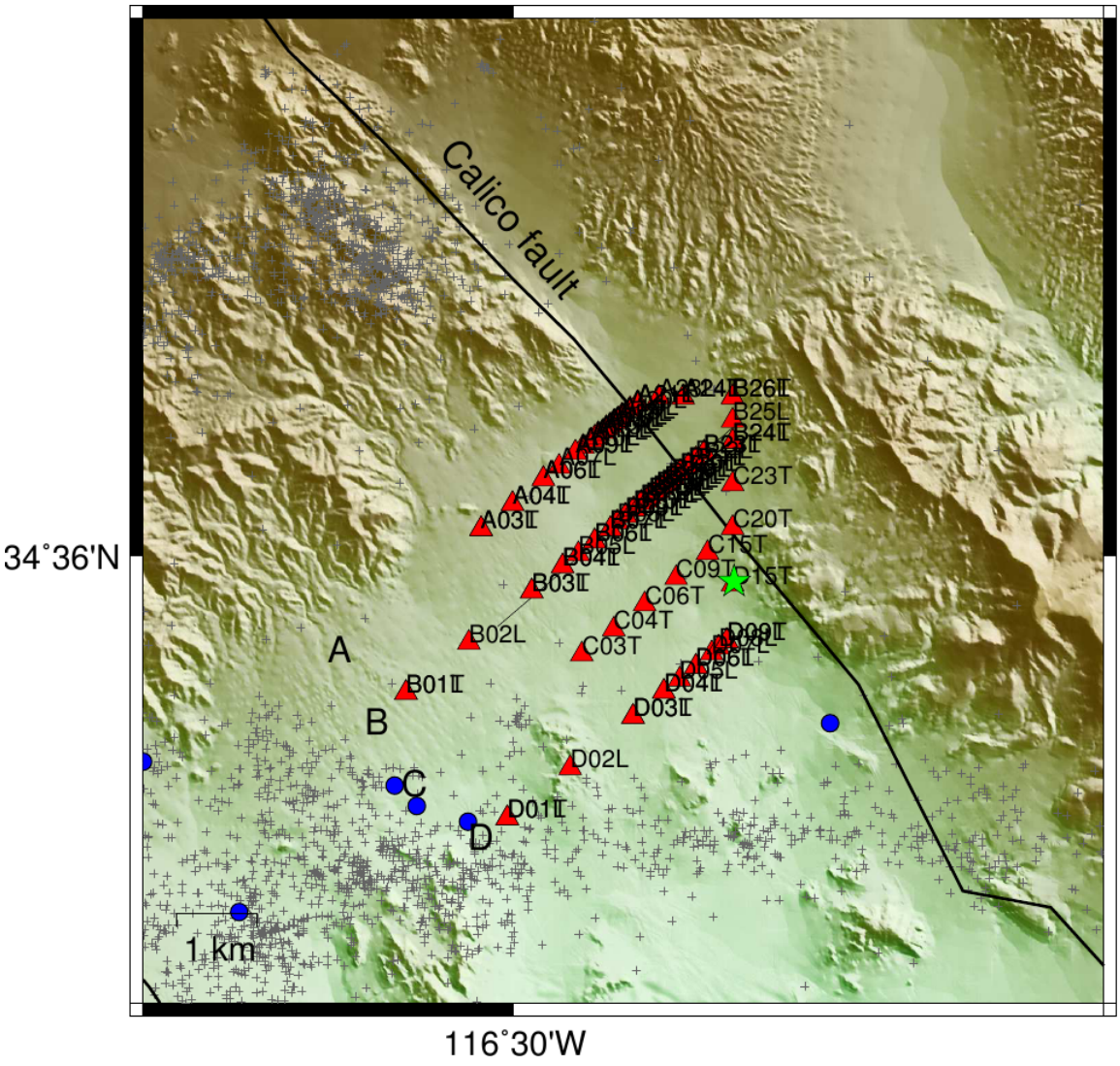

Figure 5.2: Local topography and temporary seismic stations (red triangles) across the Calico fault. Station names are labeled. T: 40T sensor, L: L22 sensor. Star and dots represent a shot and local earthquakes recorded by the array, respectively. Grey crosses show seismicity in the region.

5.3 Data analysis and results

I obtained waveform data of the 3 shots and 33 local earthquakes. Most of the earthquakes are located in the Landers fault zone, two of them are located in the Hector Mine earthquake rupture zone, and only one is located in the Calico fault zone (Fig. 5.1). They are all small magnitude events ranging from 0.7 to 3.0 in the

Table 5.1: Origin times and locations of the shots and some local earthquakes

ID	yr mo day	hr:min:sec.msec	Lat	Lon	Dep (km)	Mag
E1455	20060606	14:55:00.000	34.6605	-116.536	0	
E1550	20060606	15:50:00.000	34.6345	-116.562	0	
E1735	20060606	17:35:00.000	34.5971	-116.47	0	
3429	20060617	13:34:29.220	34.5813	-116.457	8.89	1.1
4707	20060628	13:47:07.860	34.7052	-116.368	9.03	1.0
3025	20060817	13:30:25.330	34.4825	-116.522	8.60	1.6
4843	20060903	18:48:43.340	34.5978	-116.356	12.56	0.7
2530	20060918	16:25:30.180	34.5778	-116.553	8.09	3.1
2055	20061106	17:20:55.920	34.5720	-116.513	12.07	1.7

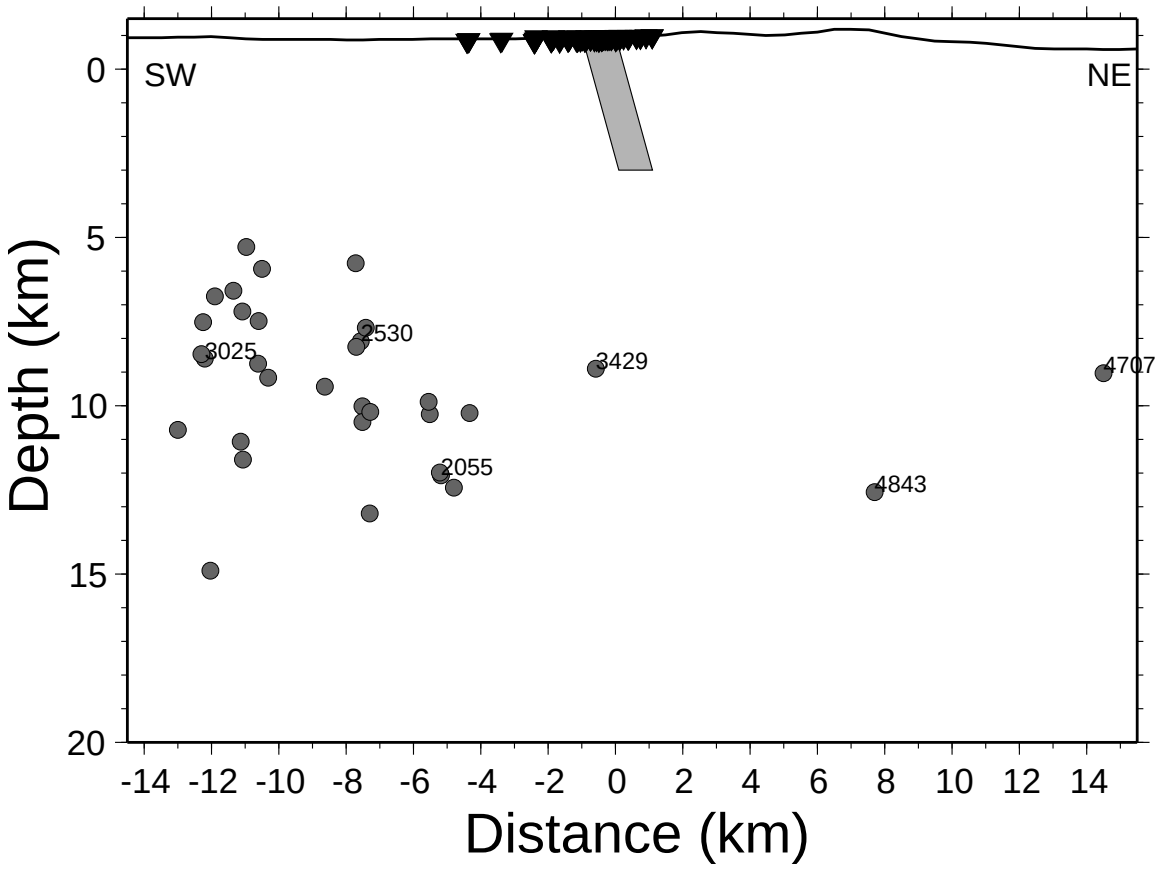

Figure 5.3: Station locations (triangle) and local topography (line) are shown on the top. Gray dots represent event locations (labeled with event number). Green stars denote three shots recorded by the array. Gray bar shows the dip and depth of the low-velocity zone obtained in this study.

Southern California Earthquake Center (SCEC) catalog. I obtained their locations from *Hauksson* [2010], who located earthquakes of southern California using a 3-D velocity model. Uncertainties of event locations are less than 1 km for lateral distance. I further improved the event focal depths using their S-P times at the temporary array (Fig. 5.3).

5.3.1 FZ widths and velocity drops

I removed instrument responses and applied a Butterworth band-pass filter to the ground velocity waveforms between 1 and 10 Hz. I then hand picked P arrival times for the shots and P- and S-wave arrivals for each local earthquake. To study the structures of the Calico fault zone using the newly developed technique of *Li et al.* [2007], I selected the longest profile, B, in the temporary array and set up the coordinate origin at the surface trace station (B20L).

I first analyzed the waveform data of the shots. Fig. 5.4 shows a record section in the P-wave time window of the outside shot located 6 km away from the array (Fig. 5.1). I also computed theoretical P-wave arrivals using a 1-D southern California velocity model [*Hadley and Kanamori*, 1977; *Shearer et al.*, 2005] and compared the model-predicted arrivals (red lines in Fig. 5.4) to the data. The P arrivals are increasingly delayed between station B06 and B19 relative to the 1-D model prediction. The amount of delay is about the same for stations in the northeastern side (B20-B26). This is the characteristic travel time delay pattern for an event located outside a LVZ (e.g. Fig 2.2). Another record section of the shot within the array is shown in Fig. 5.5. The delay increases from station B08 to the maximum near station B13 before disappearing at station B21, also a typical travel time delay pattern for an event inside a LVZ (e.g. Fig 2.3).

I rotated three component seismograms of earthquakes into the FZ radial, FZ normal, and FZ parallel directions (see details in [*Li et al.*, 2007]) using the strike

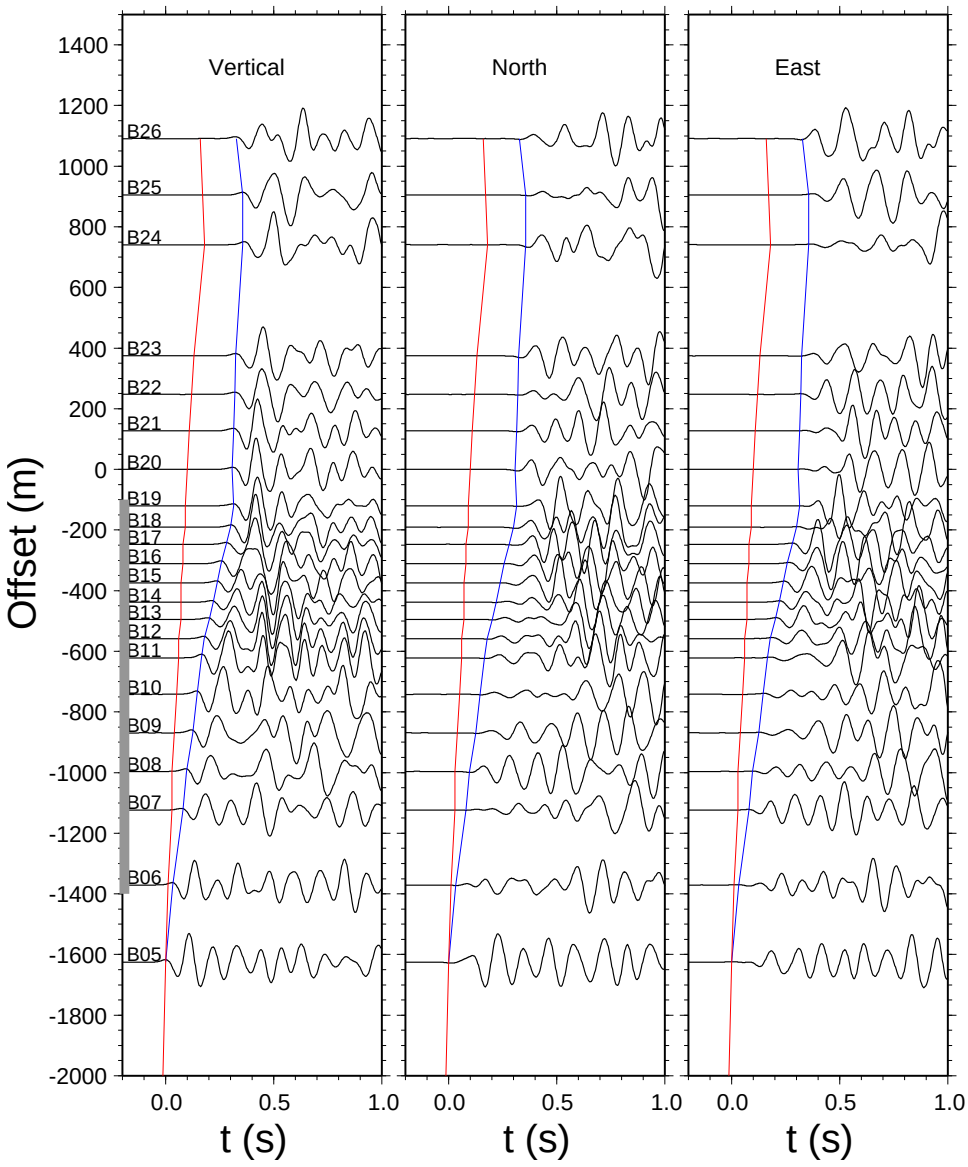

Figure 5.4: From left to right are vertical, north, and east components of waveforms in P wave window from shot E1550 outside the FZ (Fig. 5.1). Blue line shows the hand-picked P-wave arrivals. Red lines represent predicted P-wave arrivals from a 1-D southern California model [*Hadley and Kanamori*, 1977; *Shearer et al.*, 2005].

of the surface fault trace and a vertical FZ [*Cochran et al.*, 2009]. Fig. 5.6 shows a waveform record section from event 3025 located on the southwestern side of the Calico fault trace (Event information is listed in Table 5.1). Both the direct P- and

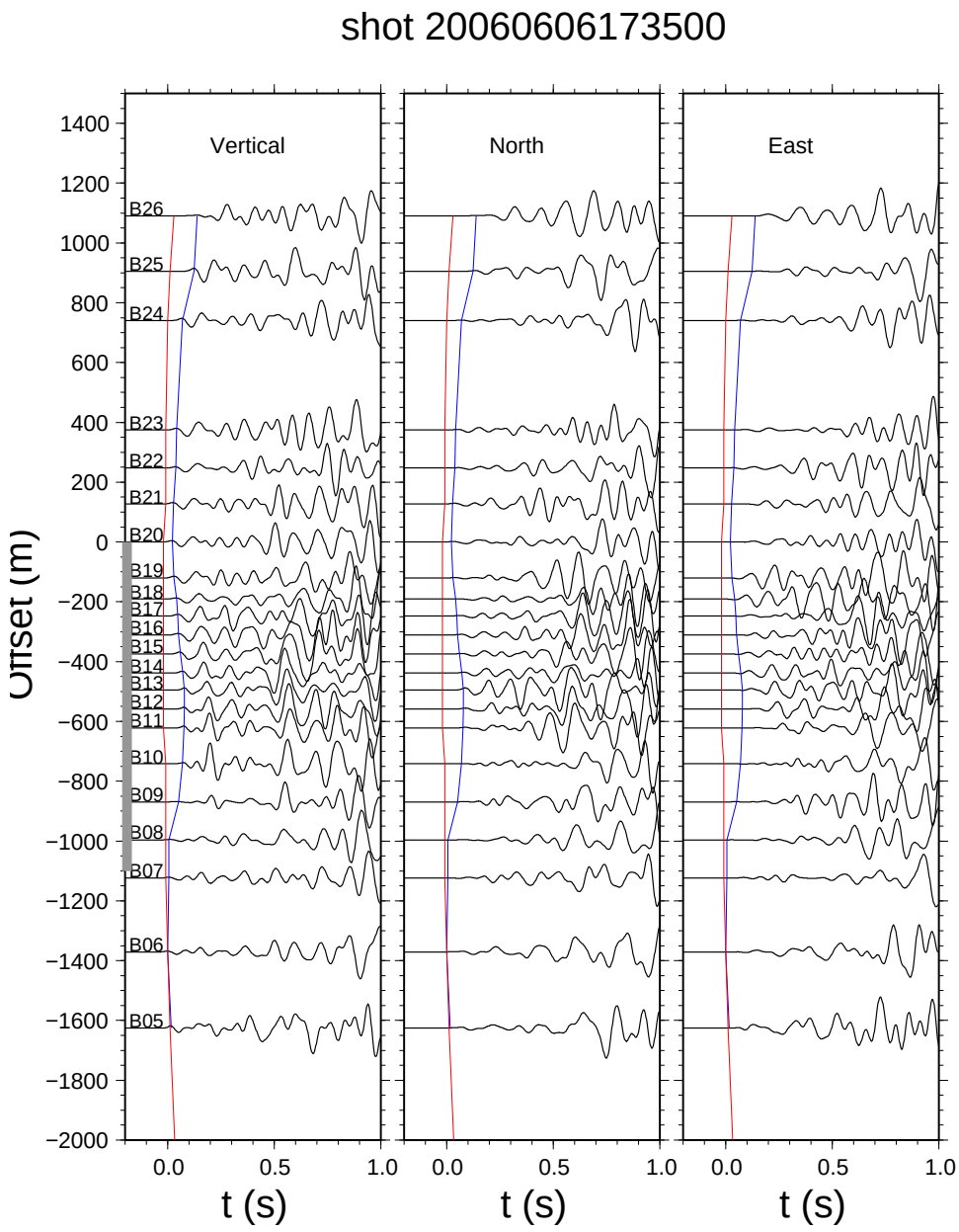

Figure 5.5: Same as Fig. 5.4. But for the shot E1735 in the FZ.

S-wave arrivals are increasingly delayed starting near station B06 and ending near station B17 (Fig. 5.6). The increased delays occur over a distance of ∼1.3 km, indicating existence of a LVZ with its northeastern boundary near B06 and southwestern boundary near B17. This allows us to constrain the LVZ width to be ∼1.3 km. The LVZ is not centered at the surface trace but is shifted to southwest.

Table 5.2: A layered velocity model of southern California

Thickness (km)	V_p (km/s)	V_p/V_s	Q
5.5	5.5	1.730	600
10.5	6.2	1.731	600
16	6.7	1.731	600
0	7.8	1.733	900

More record sections from other earthquakes show a similar travel-time-delay feature (Fig. 5.6 & 5.7). In addition, I identified the LVZ-reflected P and S waves at some stations (Fig. 5.6). The differential travel times between the direct and the LVZ-reflected phases were used to determine the velocity drop of the LVZ relative to the host rock.

I fixed the V_p of host rock to be 6.3 km s^{-1} and the V_s to be 3.6 km s^{-1}. I computed theoretical arrival times of the direct and FZ-reflected waves for a simple 1-D FZ model using the newly developed technique [*Li et al.*, 2007]. The best-estimated LVZ P-wave velocity drop is 40 per cent and S-wave velocity drop is 50 per cent relative to the host rock. The model predicted arrival times of the direct and FZ-reflected waves are shown in Fig. 5.6 & 5.7.

In addition to the arrival time modelling, I improved the FZ parameters by modelling the waveforms. I first computed focal mechanism solutions for all earthquakes using the "Cut and Paste" method [*Zhu and Helmberger*, 1996]. The Green's functions were computed using a Haskell propagator matrix technique [*Zhu and Rivera*, 2002] and a 1-D layered velocity model for southern California (Table 5.2) [*Hadley and Kanamori*, 1977]. I used Q_p=300 and Q_s=100 for the host rock and Q_p=150 and Q_s=50 for the LVZ. By adjusting the LVZ width, velocity contrast, and the western boundary offset, I could match the waveforms of the direct and FZ-reflected P and S waves (Fig. 5.8). The best fit model from waveform modelling is consistent with what I found from travel time modelling. Therefore, I concluded that the LVZ of the Calico fault is ∼1.3 km and its V_p and V_s are reduced

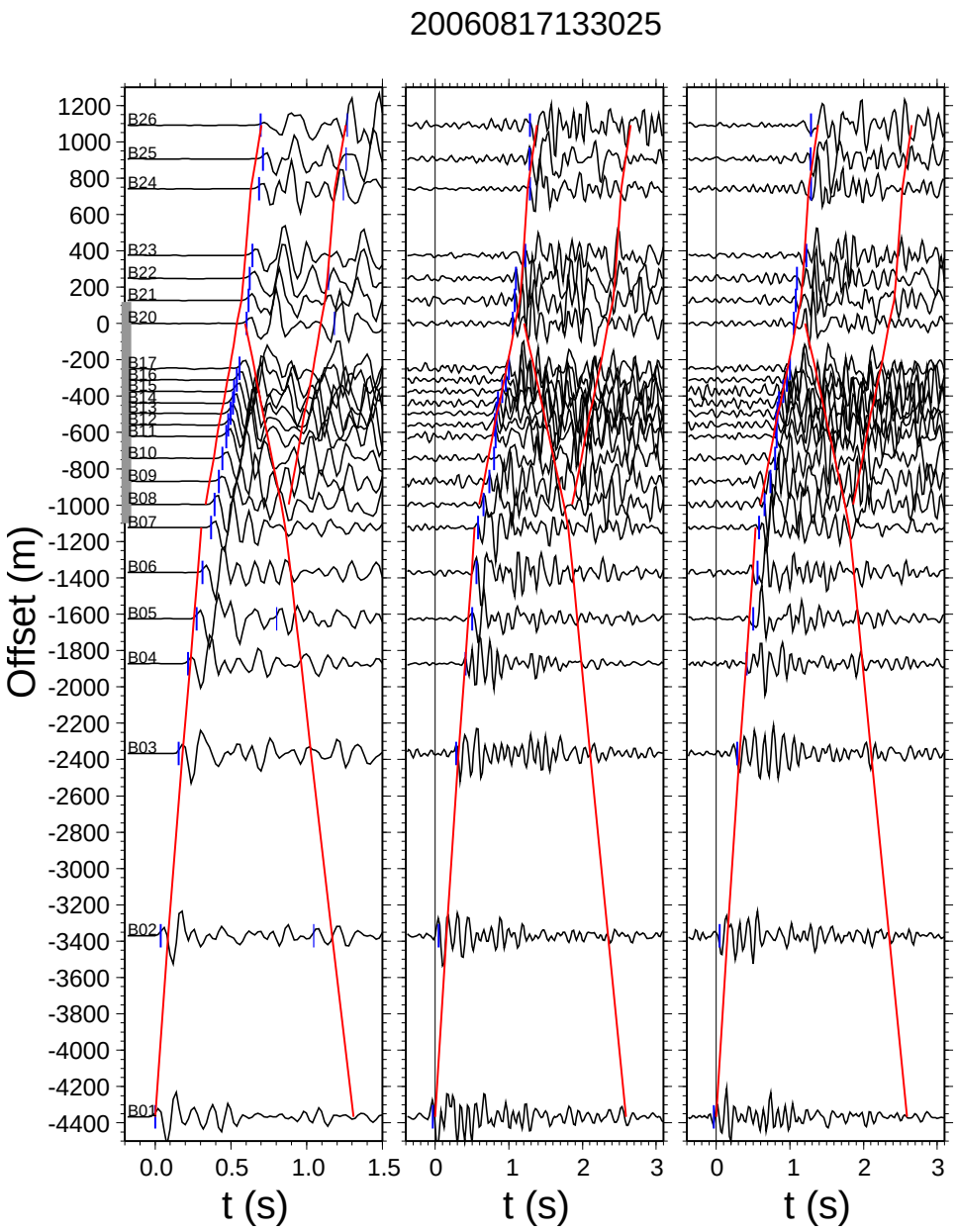

Figure 5.6: From left to right are vertical, radial, and tangential components of waveforms from an event 3025. The vertical component is in the P time window and the radial and tangential components are in the S window. The Y axis stands for the offset from the central station of the array B (Fig. 5.2) from southwest to northeast. Blue line shows the hand-picked direct P- and S-wave arrivals. Blue vertical bars denote the FZ-reflected arrivals. Red lines represent the direct and FZ-reflected P and S arrivals based on FZ model obtained in this study. Grey bar shows location of the LVZ.

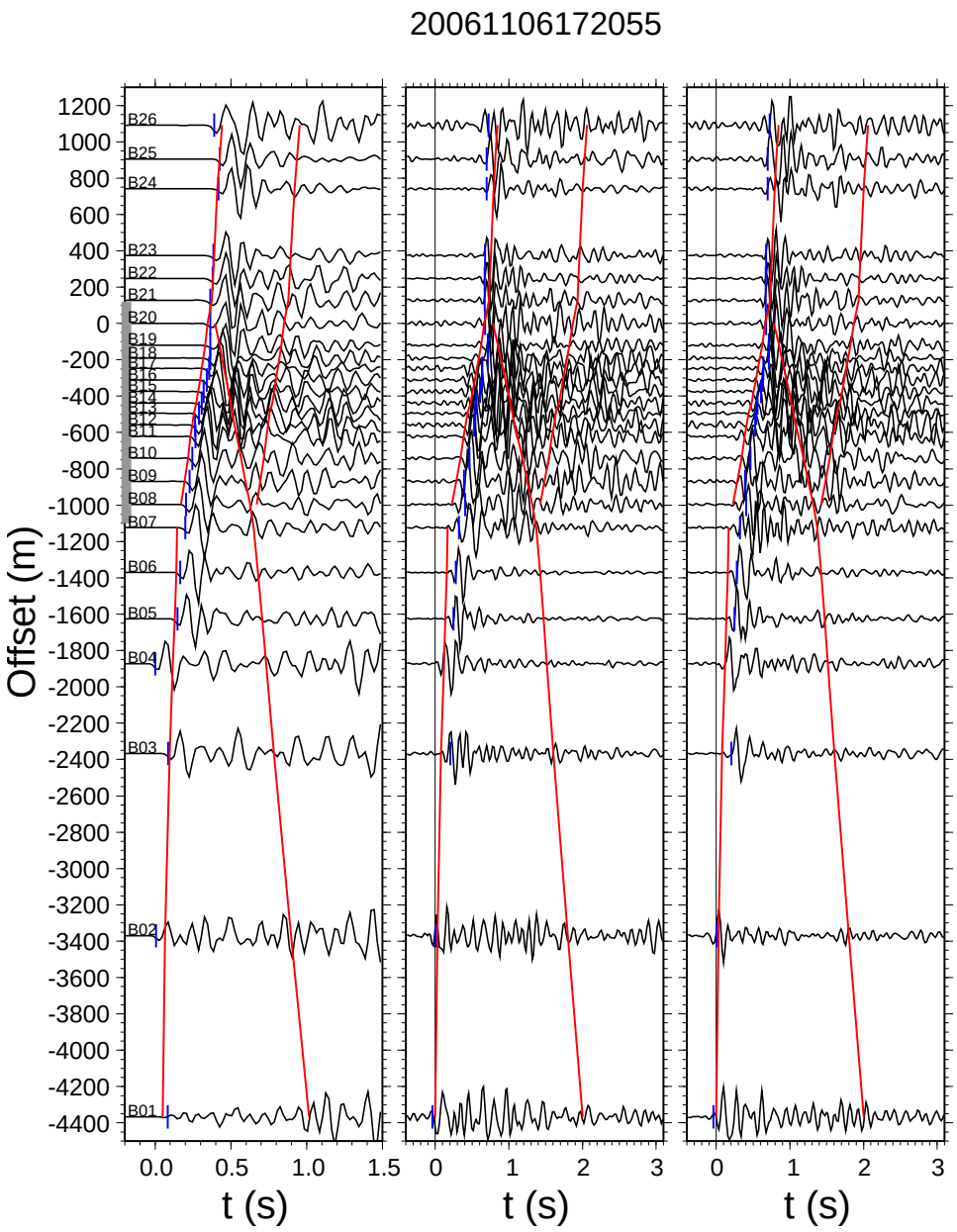

Figure 5.7: From left to right are vertical, radial, and tangential components of waveforms from an event 2055. The vertical component is in the P time window and the radial and tangential components are in the S window. The Y axis stands for the offset from the central station of the array B (Fig. 5.2) from southwest to northeast. Blue line shows the hand-picked direct P- and S-wave arrivals. Red lines represent the direct and FZ-reflected P and S arrivals based on FZ model obtained in this study. Grey bar shows location of the LVZ.

40 per cent and 50 per cent, respectively, compared to the host rock.

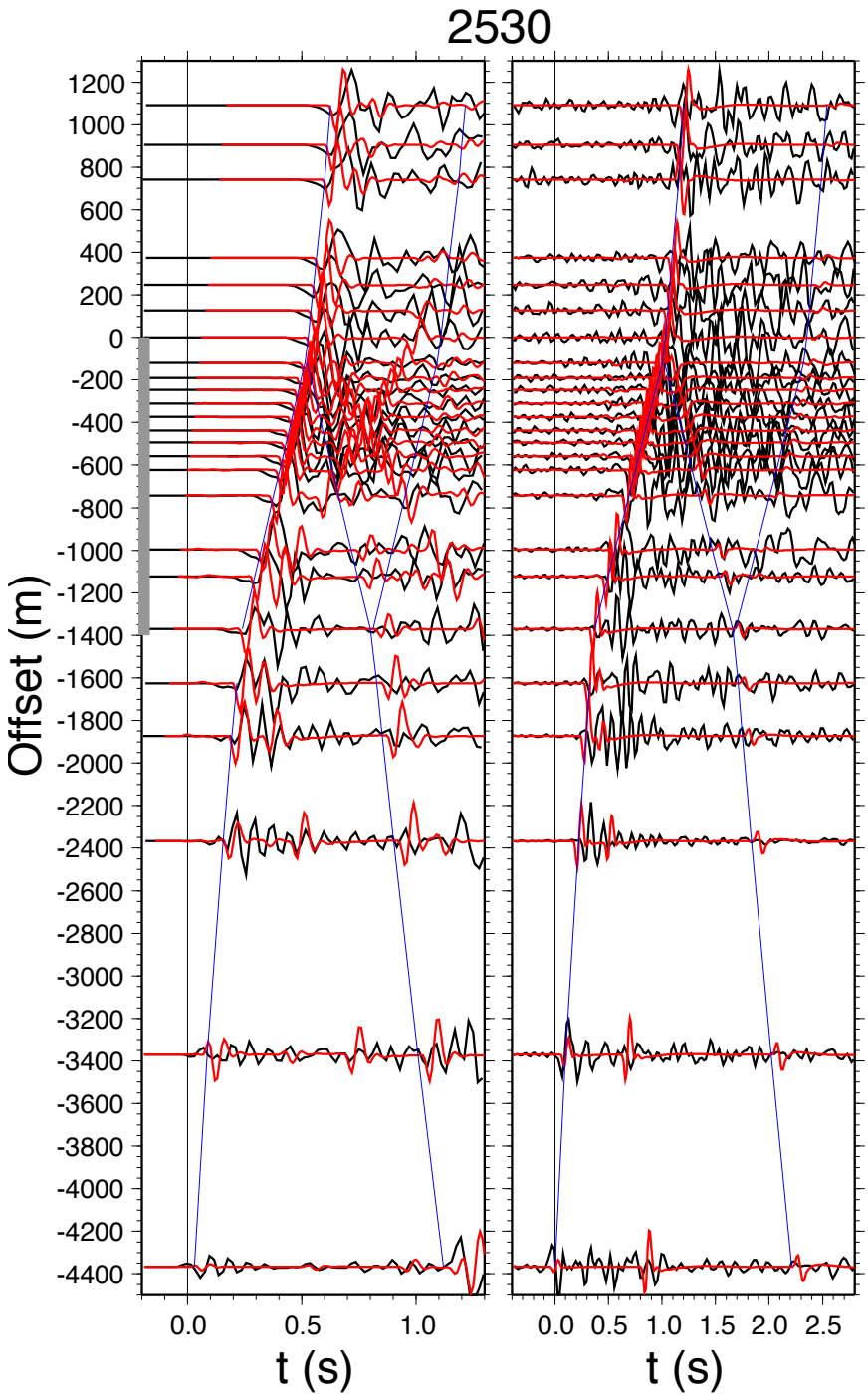

Figure 5.8: Comparison of synthetic waveform (red) and the observed seismograms (black) for event 2530. Horizontal axes show time after the earliest P (left-hand panel) and S arrival (right-hand panel). Blue lines represent predicted arrivals from the best-fit model.

Table 5.3: Different models for the Calico fault

M #	Width (km)	wb location (km)	Dip (°)	ΔV_p (%)	ΔV_s (%)	Depth (km)
1	1.3	-1.5	90	40	50	
2	1.3	-1.5	80	40	50	
3	1.3	-1.5	70	40	50	
4	1.3	-1.5	60	40	50	
5	1.3	-1.5	70	40	50	2
6	1.3	-1.5	70	40	50	3
7	1.3	-1.5	70	40	50	4
8	1.3	-1.5	70	40	50	5
9	1.3	-1.5	70	40	50	6

5.3.2 Constraints on the LVZ dip and depth

In the previous chapter, I determined the dip of the SJF using differential arrival times between the northeastern-most and southwestern-most stations of the array. I could not use the same analysis to constrain the Calico FZ dip because most events are on the southwestern side of the fault. Only two events are located in the northeast (Fig. 5.1 & 5.3). Therefore, I had to start with a vertical FZ suggested by a previous study of the Calico fault zone using trapped waves [*Cochran et al.*, 2009]. Using the vertical FZ, the best-estimated FZ width, and velocity contrasts (model 1 in Table 5.3), the model-predicted direct P and S arrivals agree well with observed arrival times of earthquakes located on the southwestern side of the fault (Fig. 5.6 & 5.7). But there are noticeable differences between the model-predicted and observed arrival times for the two earthquakes located on the northeastern side of the fault and the one event located in the fault zone. Fig. 5.9 shows the waveform record section of the event 3429 located in the Calico fault zone (Fig. 5.1). P and S arrival times are earlier than predicted at stations B08 to B15 but delayed starting from station B20 to B25 by the vertical 1-D model. Fig. 5.10 and Fig. 5.11 show record sections of the event 4707 and 4843 located on the northeastern side of the fault (Fig. 5.1). P and S arrival times are earlier than the 1-D FZ model predicted

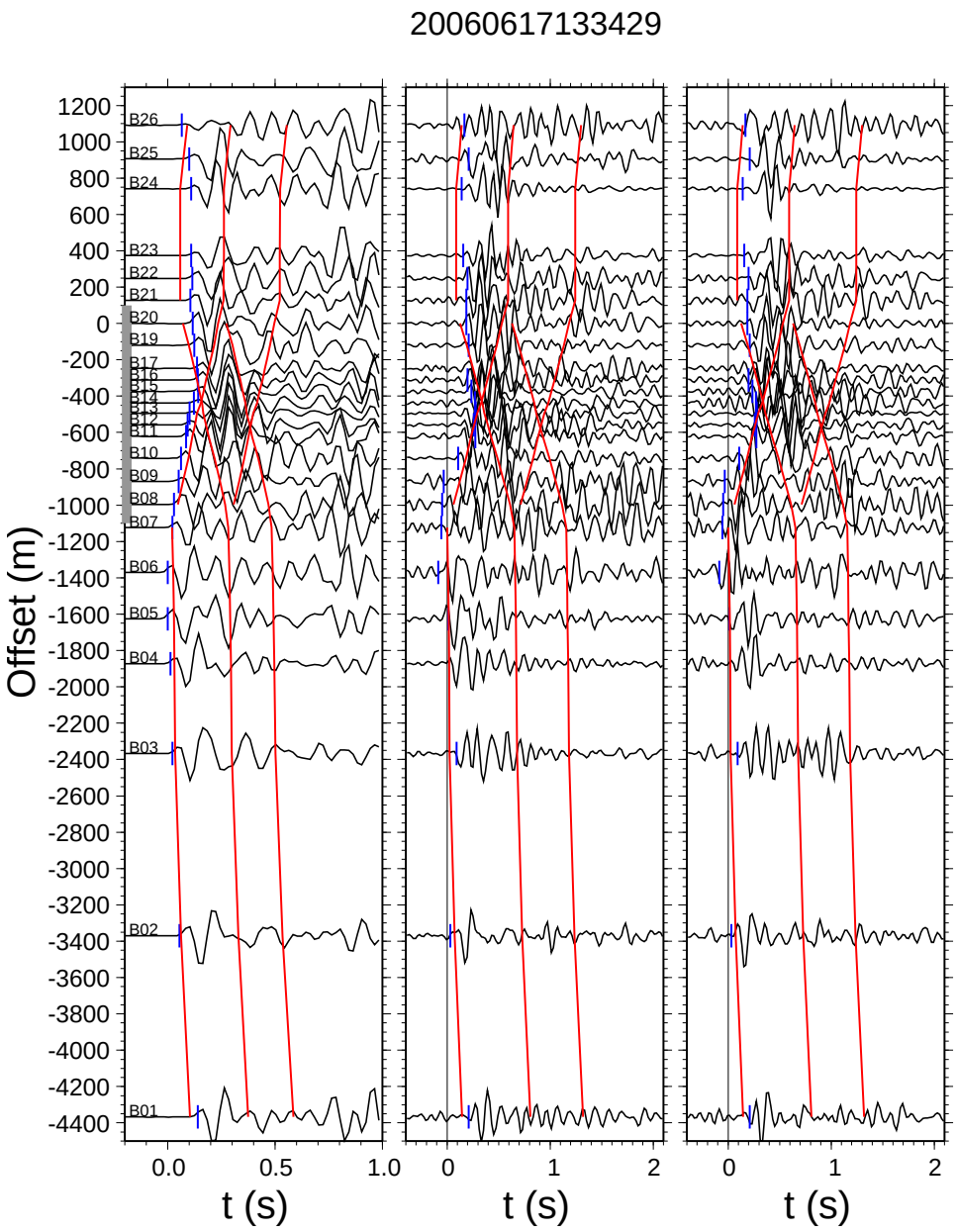

Figure 5.9: From left to right are vertical, radial, and tangential components of waveforms from event 3429. The Y axis stands for the offset from the central station of the array from southwest to northeast. Blue bars represent the hand-picked direct P- and S-wave arrivals. Red lines represent the predicted arrivals from a vertical LVZ model. Grey bar shows location of the LVZ.

arrivals from station B09. This indicates that the depth extent of the LVZ is limited such that P and S waves from the event can arrive at the stations on the other side of the FZ without being delayed by the LVZ.

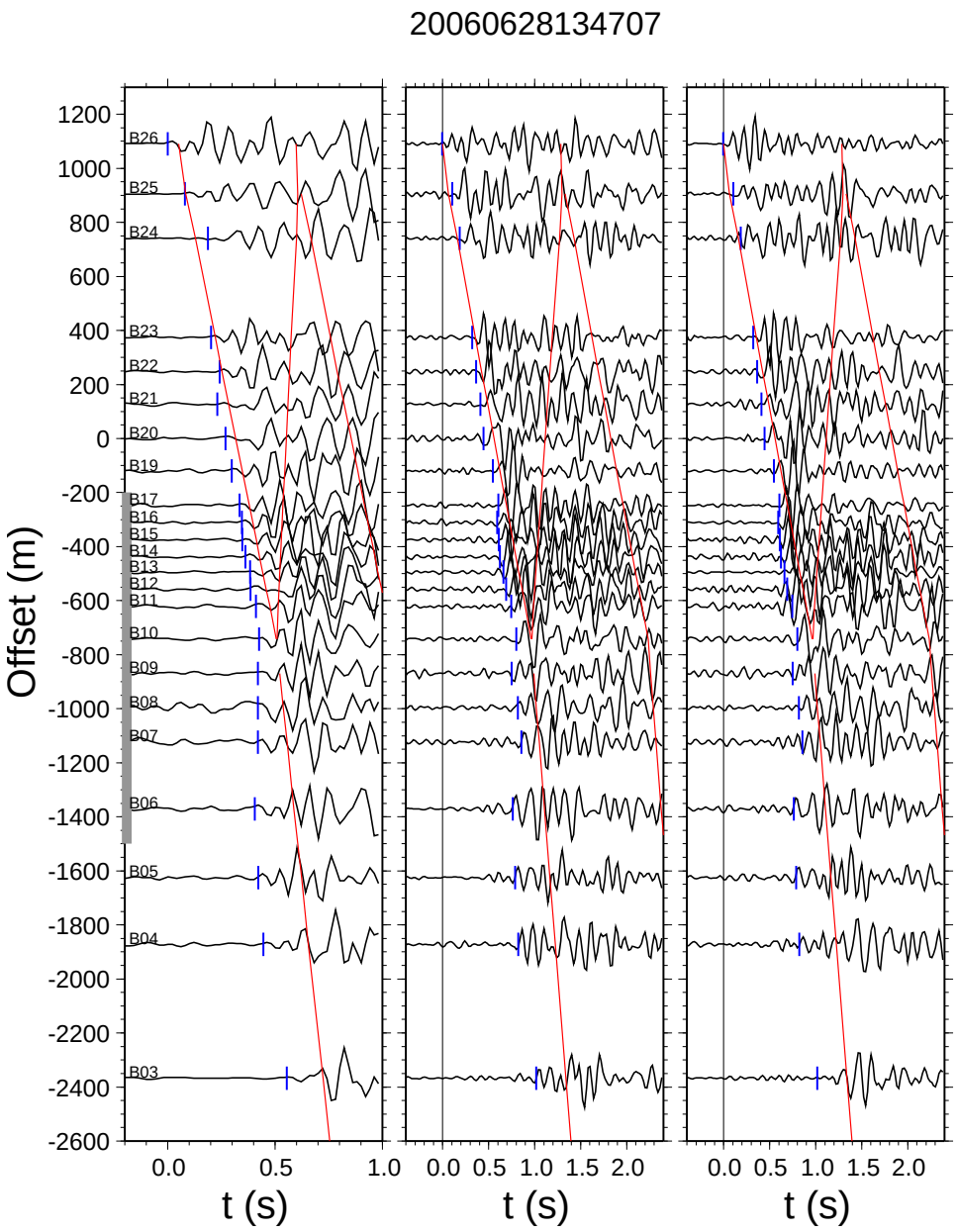

Figure 5.10: From left to right are vertical, radial, and tangential components of waveforms from event 4707. The Y axis stands for the offset from the central station of the array from southwest to northeast. Blue bars represent the hand-picked direct P- and S-wave arrivals. Red lines represent the predicted arrivals from a LVZ model dipping 70° northeast. Grey bar shows location of the LVZ. Same as Fig. 5.9. But the event is located on northeastern side of the FZ.

We tried to constrain the LVZ dip by modelling the direct P arrivals of a 1-D model. Fig. 5.12 shows the direct P-wave arrival times of three events, event 2055

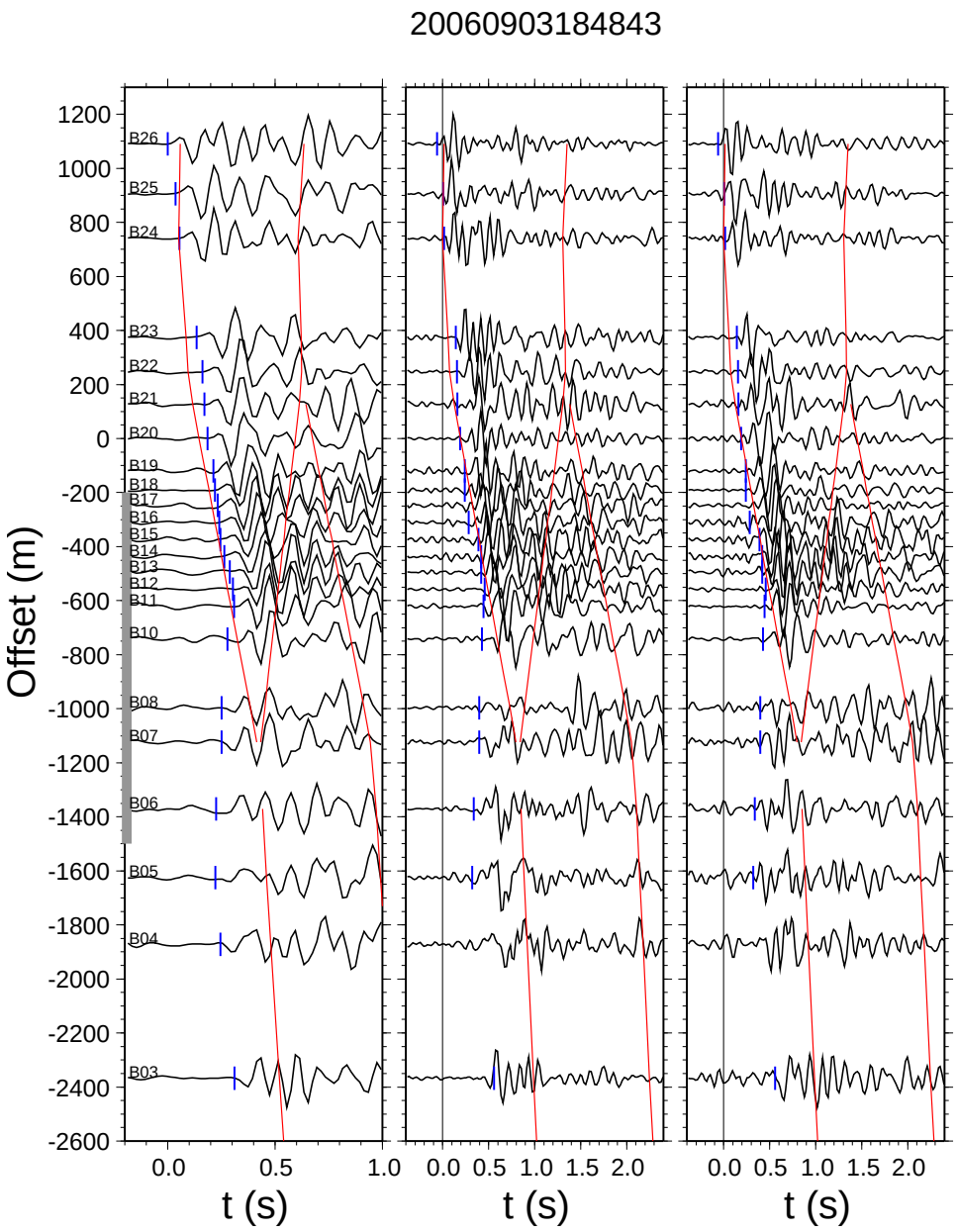

Figure 5.11: Same as Fig. 5.10.

on the southwestern, event 3429 in the central, and event 4843 on the northeastern side of the FZ. Also shown in the figure are the predicted direct P arrival times for different FZs dipping from 60° to 90° (Table 5.3). For the event 2055 on the southwestern side of the FZ, all model predictions agree well with the observed P arrival times. Among the four models, the 70° and 80° are slightly better. For the

event 3429, all model predictions agree well with the data at southwest stations but none of them can fit the data at northeast stations (Fig. 5.12). For the event 4843 on the northeastern side of the FZ, all four models predict similar arrivals that agree with the observed arrival times at northeastern stations only. The earlier-than-predicted P arrival times at stations on the NE side of the FZ for the event 3429 and at stations on the SW side of the FZ for the event 4843 are caused by termination of the LVZ at depth. I used a finite-difference code [*Graves*, 1996] to compute the direct P and S arrival times for a 3-D LVZ model dipping from 60° to 90° with different depths (Table 5.3). All other FZ parameters such as width, velocity contrast, and western boundary were fixed as determined above.

Fig. 5.13 shows comparison of observed P-wave arrivals and the model-predicted arrival times of a vertical LVZ for a southwestern event 2055, a central event 3429, and a northeastern event 4843. The preferred LVZ depth is 2 km for the northeastern event 4843, however, is 6 km for the southwestern event 2055. Therefore, the LVZ is not vertical but dips northeast. I computed different models with LVZ depths from 2 to 6 km and FZ dips from 60° to 80°. The best fit model is a 4-km deep LVZ with dip 70° by comparing observed and the model-predicted arrival times (Fig. 5.14).

5.4 Discussion

In this study, I investigated the Calico fault zone structure by modelling local earthquake waveforms recorded by a temporary array. Using a recently developed technique, I found a 1.3-km-wide LVZ of the Calico fault. Seismic velocities of the LVZ have been reduced 40 per cent in V_p and 50 per cent in V_s, consistent with previous study of the Calico fault using trapped waves [*Cochran et al.*, 2009]. Based on systematic analysis of travel times of events from two sides of the fault, I found the LVZ is not vertical but dips 70° NE. In addition, the LVZ only extends to 3–4

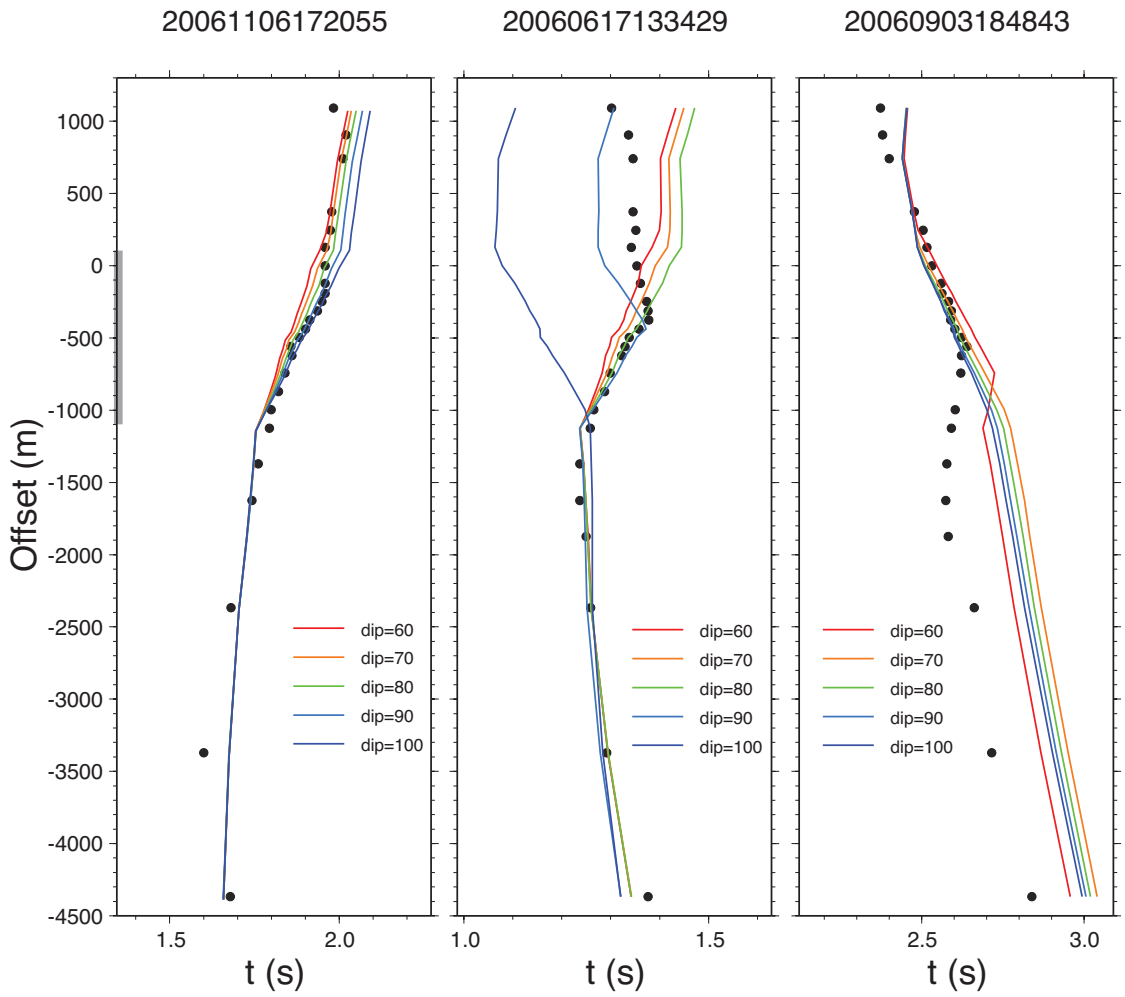

Figure 5.12: P wave arrival times (dots) and different model predictions (lines) for events on the southwestern, the central, and the northeastern side of the FZ. Grey bar shows location of the LVZ.

km in depth, shallower than the previous result 5 km [*Cochran et al.*, 2009]. The LVZ is not centered at the surface fault trace but is shifted to southwest, which has also been observed in previous studies of the San Jacinto fault zone [*Lewis et al.*, 2005; *Yang and Zhu*, 2010] and the Landers fault zone [*Li et al.*, 2007], indicating asymmetric damage pattern during earthquakes [*Dor et al.*, 2006]. I interpret the LVZ to be a region of mechanically damaged rocks related to the cumulative effect of past ruptures. Considering the low modern seismicity and lack of large historic earthquakes along the Calico fault, the damage zone must have persisted for

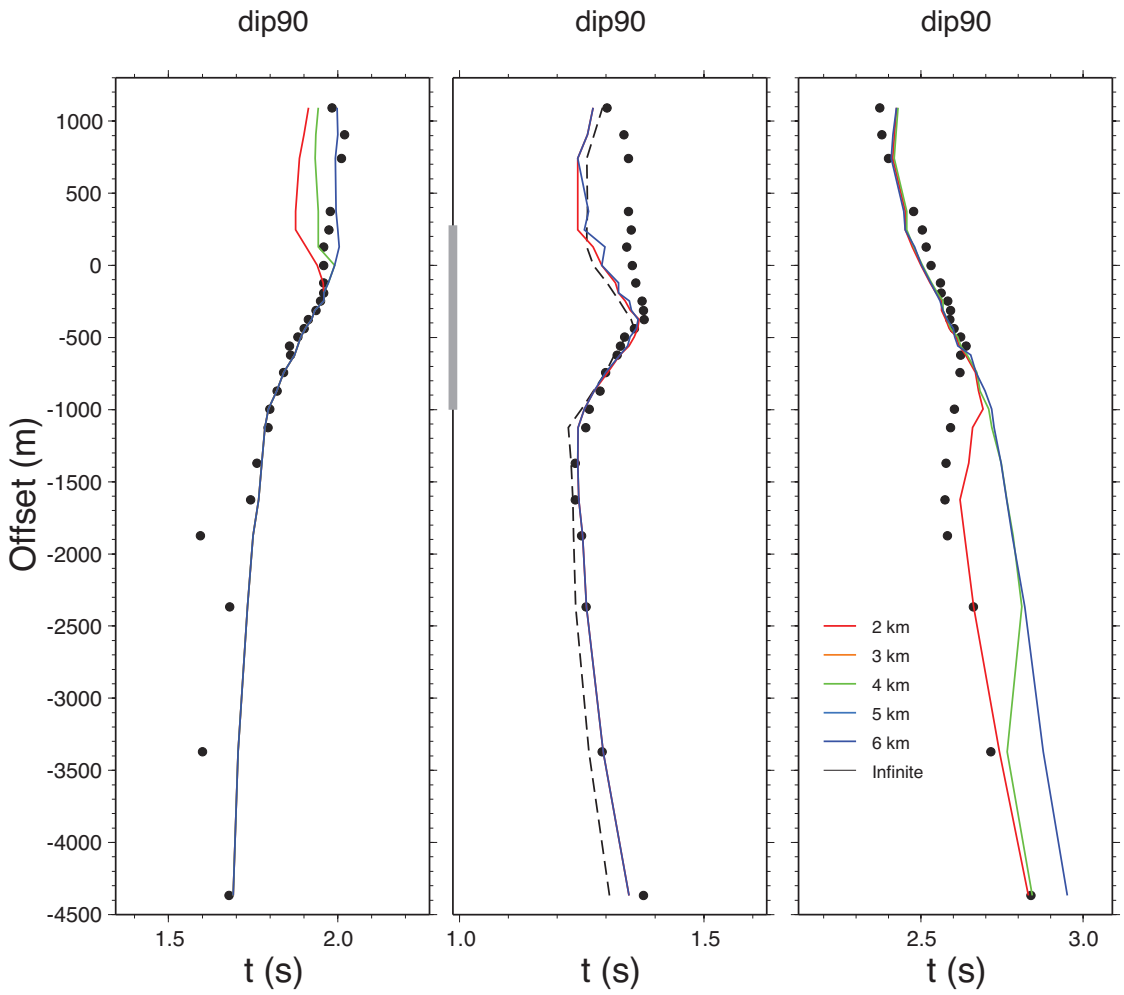

Figure 5.13: Observed (dots) and model-predicted P arrival times (lines) for event 2055, event 3429, and event 4843 for a vertical LVZ. Colors correspond to different LVZ depths.

thousands of years.

The LVZ of the Calico fault is much wider than the neighboring faults, 1.3 km vs 200 m [*Li et al.*, 1994, 2002, 2003; *Peng et al.*, 2003; *Li et al.*, 2007]. The large difference may due to that because the Calico fault is a mature fault, while the Landers and the Hector Mine FZs are relatively new. The low seismicity on the Calico fault indicates the fault has a low strength, as indicated by large coseismic deformations induced by the 1992 Landers and the 1999 Hector Mine earthquakes [*Fialko et al.*, 2002; *Fialko*, 2004]. In comparison, the Landers and the

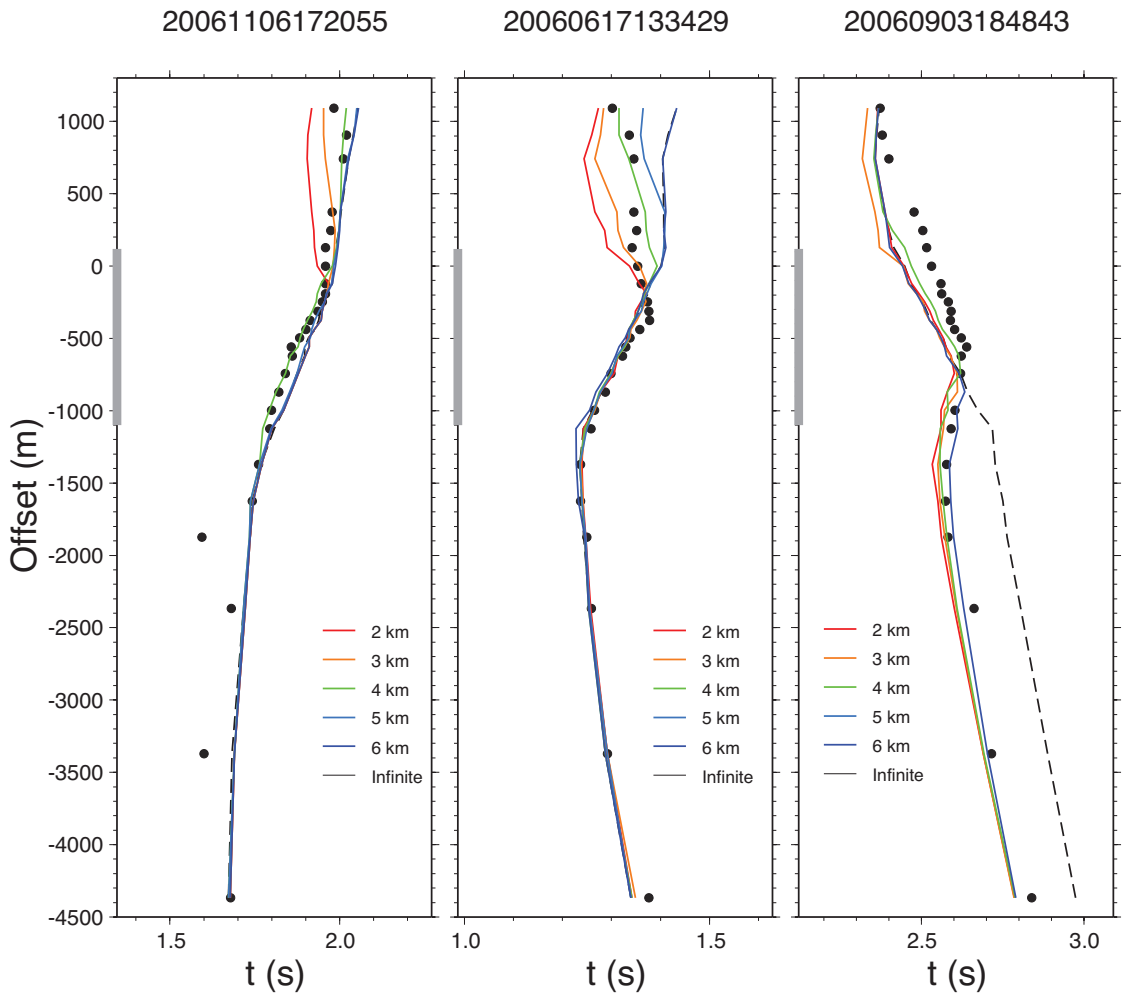

Figure 5.14: Observed (dots) and model-predicted P arrival times (lines) for event 2055, event 3429 and event 4843 for a 70°-dip LVZ. Colors correspond to different LVZ depths.

Hector Mine fault zones are strong so that seismicity is high along the two faults (Fig. 5.1). The wide damage zone of the Calico fault may also result from low normal stress across the fault. Usually a portion of the damaged zone by a large earthquake heals due to stress accumulation after the event, as reported by *Li et al.* [1998] after the 1992 Landers earthquake. But if the normal stress across the fault is low, which might be the case for the Calico fault, there will be less amount of healing and the width of the damaged zone increases with time.

Some seismic studies have suggested that the fault damage zone extends to great

depth. An aftershock waveform study suggested that a 300-m-wide LVZ of the Landers FZ extends to 7 km depth [*Li et al.*, 2007]. A FZ-trapped wave study of the Hector Mine FZ presented a 100-m-wide LVZ with 40–50 per cent reduction in V_s and depth extent of ∼10 km [*Li et al.*, 2002, 2003]. FZ trapped wave studies of the San Jacinto fault suggested a ∼200-m-wide LVZ extending to the seismogenic depth (15–20 km) [*Li et al.*, 1997; *Li and Vernon*, 2001] while another group argued for a shallow energy trapping structure (3–5 km) [*Lewis et al.*, 2005]. In this study, I found a 4-km-deep LVZ along the Calico fault by analysis of arrival time advances at stations on one side of the fault from earthquakes on the other side. During the analysis, I fixed the LVZ strike, dip, velocity contrast and width, and event locations and estimated the depth uncertainty to be ∼1 km. The uncertainty of LVZ depth could be very large considering the combined effect of the uncertainties of FZ parameters. One possible improvement is to analyze such arrival time advances for large number of events from both sides of the fault so that the LVZ dip and depth could be constrained simultaneously. Unfortunately, most local earthquakes recorded in the Calico experiment were from one side (Fig. 5.1).

5.5 Summary

As documented here, I found a 1.3-km-wide LVZ with 40 per cent reduction in V_p and 50 per cent reduction in V_s along the Calico fault, southern California, by modelling high frequency body waves of local earthquakes. The LVZ dips 70° northeast and its depth extent is no more than 4 km. It is not centered at the surface fault trace but is shifted to the southwest, indicating assymetric fault damage during earthquakes.

Chapter 6: Discussion and Conclusions

6.1 Asymmetric Damage

I determined fine structures of the San Jacinto and the Calico fault zone using high-frequency body waves. The LVZ width is very different for the two faults, 150 m vs 1.3 km, probably due to different material properties and local stress that is critical for damage zone healing. However, one common feature of the two faults is that the LVZs are not centered at surface fault trace but are located on one side, e.g. northeast for the SJF and southwest for the Calico fault. This asymmetric damage pattern was observed by various geologic and seismic studies in different FZs, including previous study of the Landers fault [*Flodin and Aydin*, 2004; *Lewis et al.*, 2005; *Dor et al.*, 2006; *Li et al.*, 2007].

Numerical studies of rupture propagation along an interface between two elastic solids with different seismic velocities show that damage would prefer to generate in the stiffer side because that part was in the tensional quadrant of the rupture front while the softer side was under compression [*Ben-Zion*, 2001; *Ben-Zion and Shi*, 2005]. Following this numerical prediction, our observations of asymmetric damage along the Landers, the San Jacinto, and the Calico fault zone indicate velocity contrast of crustal blocks across the faults. The damage zone of the SJF is located on the northeast side of the rupture, implying that the seismic velocity in the northeastern side is faster than the other side which is revealed by a 3-D P wave tomography study in the region [*Scott et al.*, 1994]. I found that the damage zone of the Calico fault is located on the southwest side, indicating a higher seismic velocity in the southwestern block. The local velocity structure of the Calico fault zone was imaged by *Cochran et al.* [2009], who showed that the southwestern side of the fault has faster seismic velocities using FZ trapped waves.

Sammis et al. [2009] reviewed experimental studies of the effects of off-fault

damage on earthquake rupture propagation and concluded that the damage has impact on rupture velocities. Ruptures on an interface between two damaged Homalite plates travel at sub-Rayleigh velocities, indicating that sliding in the off-fault damage zone dissipates energy. This result was also found in a numerical simulation of rupture propagation on a fault bisecting a low-velocity zone [*Harris and Day*, 1997]. In comparison, ruptures on the interface between undamaged and damaged Homalite plates propagate drastically different. The damage zone appears to have little effect on the rupture propagation in the compressional direction but completely suppresses rupture propagation in the tensional direction. These experimental results suggest that the unilateral rupture will be preferred along a fault plane with a damaged zone on one side.

6.2 Determination of the LVZ depth

A central issue in FZ structure imaging is the depth extent of the low-velocity waveguide zone. One group suggested that it penetrates down to the base of the seismogenic zone [e.g. *Li et al.*, 1994, 2000; *Li and Vernon*, 2001; *Li et al.*, 2004], while others argued for a shallow trapping structure extending only to a depth of 3–5 km [e.g. *Ben-Zion et al.*, 2003; *Peng et al.*, 2003; *Lewis et al.*, 2005]. Numerical analysis showed that obvious trapped waves can be observed for seismic sources outside and below a FZ or inside the FZ [*Igel et al.*, 2002; *Jahnke et al.*, 2002]. Their results concluded that the depth extent of LVZ is still unresolved by only using FZ trapped waves. A recent numerical analysis of FZ trapped wave pointed out that determination of fault structure at seismogenic depth requires analysis of data at higher frequencies than the FZ trapped wave [*Wu et al.*, 2008].

In this study, I used high-frequency body waves of local earthquakes to determine the LVZ depth of the SJF and the Calico fault. For the SJF, I found a precursor before the direct S waves, the S_{diff} waves, which are sensitive to LVZ depth [*Li*

et al., 2007]. I also estimated the LVZ depth uncertainties by performing synthetic tests and taking into account of uncertainties of event location. My modelling results show that the LVZ of the BRF extends 2 km in depth that is consistent with the proposed shallow structure of *Lewis et al.* [2005]. Since most event locations used in the SJF study have uncertainties less than 1 km [*Shearer et al.*, 2005], I estimated that the uncertainties of the LVZ depth of the BRF is less than 1 km.

The S_{diff} waves could only be observed under certain geometries of event and station locations, and the LVZ. I did not observe clear S_{diff} waves in the dataset of the Calico fault, therefore I could not use the same technique to constrain the its LVZ depth. Fortunately, the array across the Calico fault is long enough for me to see the arrival time advances at southwestern stations from northeastern earthquakes (Fig. 5.10). Using a 3D finite-difference code [*Graves*, 1996], I fixed all other FZ parameters (FZ dip, strike, velocity contrast, and width) and determined the LVZ depth by modelling the arrival time advances. The LVZ of the Calico fault is estimated as ∼4 km, with a 1 km uncertainty when the FZ dip, velocity contrast and width are fixed. However, there might be a strong trade-off between the LVZ dip and depth.

6.3 Determination of source parameters of local earthquakes

In addition to the travel time modelling, we also modeled waveforms of local earthquakes to probe fine structures of crustal fault zones. In order to perform waveform modelling, we need to know source parameters of the local earthquakes. We used the "Cut and Paste" (CAP) method [*Zhu and Helmberger*, 1996] to determine earthquake focal mechanism solutions in this study. The CAP method decomposes seismograms and uses amplitude information in different time windows (e.g., *Pnl* and surface wave) to increase the stability and resolution of focal mechanism solution. However, it is challenging to determine source parameters for

small-magnitude events because there is little low-frequency energy which is usually used in focal mechanism determinations. *Tan and Helmberger* [2007] developed a new method to determine small earthquake source parameters using short-period (0.5–2 Hz) P waves by implementing a calibration term to stations from well determined source parameters in the region based on the traditional CAP method. They documented a few moment tensor solutions for earthquakes that occurred on the Calico fault and the Hector Mine rupture zone (Fig. 6.1). One of them, an M_w 3.5 earthquake, is on the Calico fault and has a thrust focal mechanism that is inconsistent with the long-term strike-slip fault motion, implying the Calico fault is probably under complicated shear forces. Therefore, accurate focal mechanism solutions for large number of events would help us probe the local stress field and possibly understand the existence of a wide damage structure.

Numerous earthquakes occurred along the Landers and the Hector Mine earthquake rupture zones (Fig. 5.1) and most of them are small-magnitude (M <3) events. The 1992 M_w 7.3 Landers earthquake caused two east-west ruptures connecting the Landers and the Calico fault zone (Fig. 6.1). Some events that happened on the new ruptures were recorded by the Calico fault zone experiment. It could be a future work to determine their source parameters using data from the temporary array by the newly developed CAP method [*Tan and Helmberger*, 2007], to understand the fault kinematics in the region.

6.4 Conclusions

In summary, I analyzed high frequency waveforms of local earthquakes to map crustal faults and to investigate fine structures of fault zones. I have developed a reliable and efficient method to detect small magnitude earthquakes using template events and waveform cross-correlation. I found more than 120 aftershocks in the first two weeks following the April 18, 2008, Mt. Carmel earthquake, more than

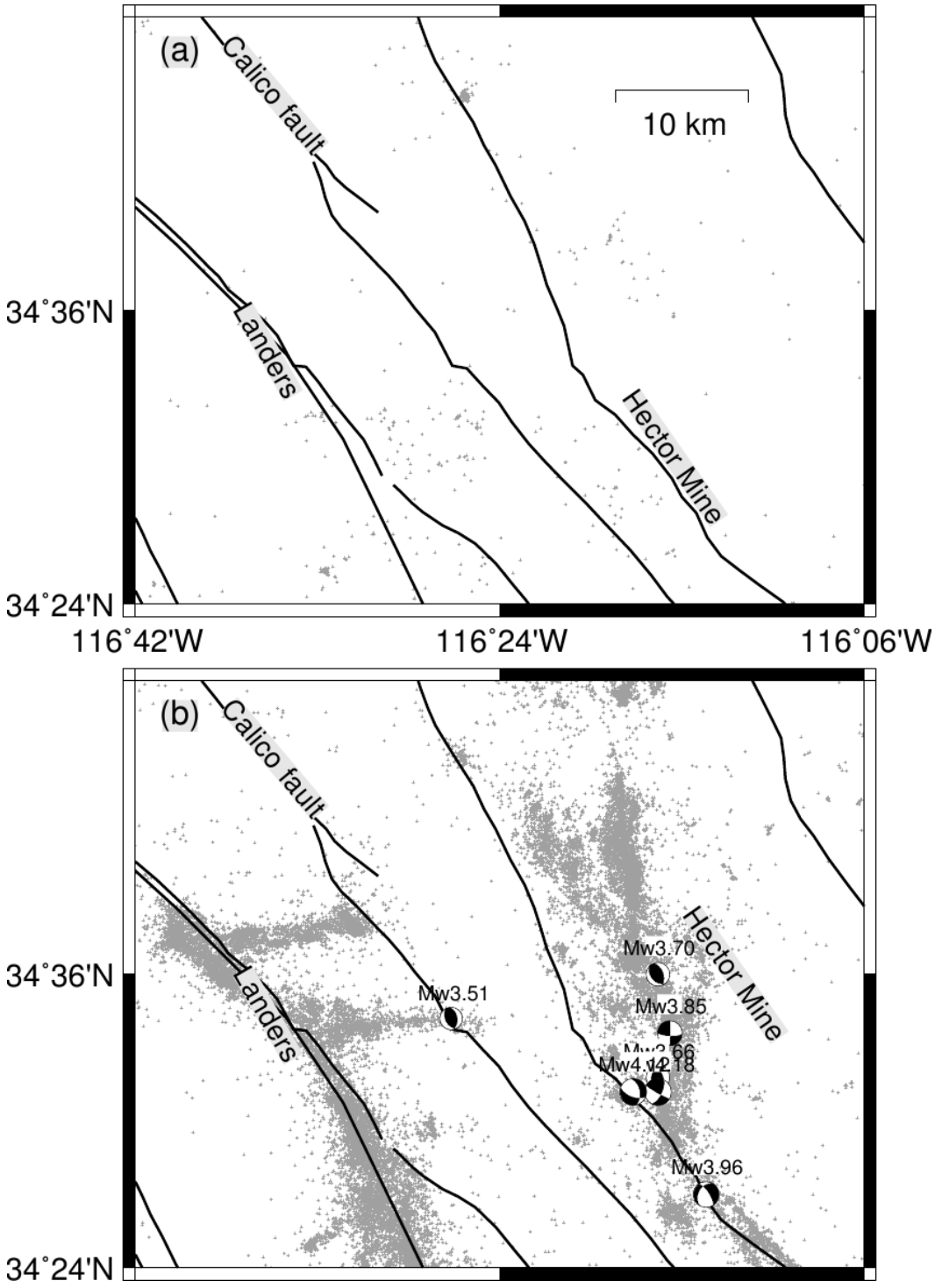

Figure 6.1: Local seismicity before 1992 (a) and after 1992 (b). Mapped faults (lines) and local earthquakes with source parameters are plotted.

three times the number reported by the permanent network with the traditional STA/LTA detector. I relocated 28 events by the double-difference relocation algorithm and found that these events were located on a nearly vertical plane striking WNW-ESE. By combining the relocation results with focal mechanism solutions, I concluded that the fault responsible for the April 18 earthquake is a left-lateral, strike-slip fault with an orientation of 292° and a dip angle of 81°. The fault coincides with one of the proposed left-stepping accommodation zones (Divide) in the La Salle deformation belt and indicates reactivation of old deformation zone by contemporary stresses in the Midcontinent.

To investigate the fine structures of the San Jacinto fault zone and the Calico fault zone in southern California, I used P- and S-wave travel times and waveforms of local earthquakes recorded by temporary arrays across the faults. In the San Jacinto fault zone study, I developed a method to determine depth extent of the LVZ using S-wave precursors. I found that the LVZ of the BRF branch has a width of ∼150 m with a 30–40 per cent reduction in V_p and a 50–60 per cent reduction in V_s. The fault dips 70° to southwest and its LVZ extends only to 2±1 km in depth. The LVZ of the CVF branch has a width of ∼200 m with 40 per cent reduction in V_p and 50 per cent reduction in V_s. The CCF is nearly vertical and has a LVZ of ∼150 m in width and of 25 per cent reduction in V_p and 50 per cent reduction in V_s. The LVZs of these three branches are not centered at the surface fault trace but are located to their northeast, indicating asymmetric damage during earthquakes.

In the Calico fault zone study, I performed a systematic analysis of travel times from earthquakes located on northeastern and southwestern side of the fault. I found a 1.3-km-wide LVZ with a 40 per cent reduction in V_p and 50 per cent reduction in V_s of the Calico fault. The fault dips 70° to northeast and its LVZ extends only to ∼4 km in depth. The LVZ is not centered at the surface fault either, but is shifted to southwest.

References

Aki, K., Characterization of barriers on an earthquak fault, *J. Geophys. Res.*, *84*, 6140–6148, 1979.

Aki, K., and W. H. K. Lee, Determination of three-dimensional velocity anomalies under a seismice array using first P arrival times from local earthquakes. 1. A homogeneous initial model, *J. Geophys. Res.*, *81*, 4381–4399, 1976.

Ault, C. H., and D. M. Sullivan, Faulting in southwest Indiana, U.S. Nuclear Regulatory Commission Report, *Tech. Rep. NUREG/CR-2908*, Indiana Geological Survey, 1982.

Ault, C. H., D. Harper, C. R. Smith, and M. A. Wright, Faulting in jointing in and near surface mines of southwest Indiana, *Tech. Rep. NUREG/CR-4117*, Indiana Geological Survey, 1985.

Becker, T. W., J. L. Hardebeck, and G. Anderson, Constraints on fault slip rates of the southern California plate boundary from GPS velocity and stress inversions, *Geophys. J. Int.*, *160*, 634–650, 2005.

Ben-Zion, Y., Dynamic ruptures in recent models of earthquake faults, *J. Mech. Phys. Sol.*, *49*, 2209–2244, 2001.

Ben-Zion, Y., and K. Aki, Seismic radiation from an SH line source in a laterally heterogeneous planar fault zone, *Bull. Seismol. Soc. Am.*, *80*, 971–994, 1990.

Ben-Zion, Y., and P. Malin, San Andreas fault zone head wave near Parkfield, California, *Science*, *251*, 1592–1594, 1991.

Ben-Zion, Y., and C. Sammis, Mechanics, structure and evolution of fault zones, *Pure Appl. Geophys.*, *166*, 1533–1536, doi:10.1007/s00024-009-0509-y, 2009.

Ben-Zion, Y., and C. G. Sammis, Characterization of fault zones, *Pure Appl. Geophys.*, *160*, 677–715, 2003.

Ben-Zion, Y., and Z. Shi, Dynamic rupture on a material interface with spontaneous generation of plastic strain in the bulk, *Earth Planet. Sci. Lett.*, *236*, 486–496, 2005.

Ben-Zion, Y., S. Katz, and P. Leary, Joint inversion of fault zone head waves and direct P arrivals for crustal structure near major faults, *J. Geophys. Res.*, *97*, 1943–1951, 1992.

Ben-Zion, Y., Z. Peng, D. Okaya, L. Seeber, J. G. Armbruster, N. Ozer, A. J. Michael, S. Baris, and M. Aktar, A shallow fault-zone structure illuminated by trapped waves in the Karadere-Duzce branch of the North Anatolian fault,

western Turkey, *Geophys. J. Int.*, *152*(3), 699–717, doi:10.1046/j.1365-246X.2003.01870.x, 2003.

Bleibinhaus, F., J. A. Hole, T. Ryberg, and G. S. Fuis, Structure of the California Coast Ranges and San Andreas fault at SAFOD from seismic waveform inversion and reflection imaging, *J. Geophys. Res.*, *112*(B06315), doi:10.1029/2006JB004611, 2007.

Chavarria, J. A., P. Malin, R. D. Catchings, and E. Shalev, A look inside the San Andreas fault at Parkfield through vertical seismic profiling, *Science*, *302*, 1746–1748, 2003.

Chester, F. M., and J. S. Chester, Ultracataclasite structure and friction processes of the Punchbowl fault, San Andreas system, California, *Tectonophysics*, *295*, 199–221, 1998.

Chester, F. M., and J. M. Logan, Implications for mechanical properties of brittle faults from observations of the Punchbowl Fault zone, California, *Pure Appl. Geophys.*, *124*, 79–106, 1986.

Chester, F. M., and J. M. Logan, Composite planar fabric of gouge from the Punchbowl fault, California, *J. Structural Geol.*, *9*, 621–634, 1987.

Chester, F. M., J. P. Evans, and R. L. Biegel, Internal structure and weakening mechanisms of the San Andreas fault, *J. Geophys. Res.*, *98*, 771–786, 1993.

Chester, F. M., D. L. Kirschner, and J. S. Chester, Structural and geochemical investigations of the Punchbowl fault, San Andreas system, California, *Tech. Rep. TW7400 98–001*, Japan Nuclear Cycle Development Institute Publication, 1998.

Cochran, E. S., M. Radiguet, P. M. Shearer, Y. Li, Y. Fialko, and J. E. Vidale, Seismic imaging of the damage zone around the Calico fault, *EOS Trans. AGU*, *87*(52), doi:Fall Meet. Suppl., Abstract T23E-03, 2006.

Cochran, E. S., Y. Li, P. M. Shearer, S. Barbot, Y. Fialko, and J. E. Vidale, Seismic and geodetic evidence for extensive, long-lived fault damage zones, *Geology*, *37*, 315–318, doi:10.1130/G25306A.1, 2009.

Dokka, R. K., and C. J. Travis, Late Cenozoic strike-slip faulting in the Mojave desert, California, *Tectonics*, *9*(2), 311–340, 1990.

Dor, O., T. K. Rockwell, and Y. Ben-Zion, Geological observations of damage asymmetry in the structure of San Jacinto, San Andreas and Punchbowl faults in southern California: A possible indicator for preferred rupture propagation direction., *Pure appl. geophys.*, *163*, 301–349, 2006.

Duchek, A. B., J. H. McBride, W. J. Nelson, and H. E. Leetaru, The Cottage Grove fault system (Illinois Basin): late Paleozoic transpression along a Precambrian crustal boundary, *Geol. Soc. Am. Bull.*, *116*, 1465–1484, 2004.

Eagar, K. C., G. L. Pavlis, and M. W. Hamburger, Evidence of possible induced seismicity in the Wabash Valley seismic zone from improved microearthquake locations, *Bull. Seismol. Soc. Am.*, *96*, 1718–1728, 2006.

Eberhart-Phillips, D., and A. J. Michael, Three-dimensional velocity, structure, seismicity, and fault structure in the Parkfield region, Central California, *J. Geophys. Res.*, *98*, 15,737–15,757, 1993.

Eberhart-Phillips, D., W. D. Stanley, B. D. Rodriguez, and W. J. Lutter, Surface seismic and electrical methods to detect fluids related to faulting, *J. Geophys. Res.*, *97*, 12,919–12,936, 1995.

Evans, J. P., and F. M. Chester, Fluid-rock interaction in faults of the San Andreas system: Inferences from San Gabriel fault rock geochemistry and microstructures, *J. Geophys. Res.*, *100, No. B7*, 13,007–13,020, 1995.

Fialko, Y., Probing the mechanical properties of seismically active crust with space geodesy: Study of the coseismic deformation due to the 1992 m_w 7.3 Landers (southern California) earthquake, *J. Geophys. Res.*, *109*, 983–988, doi:doi:10.1029/2003JB002756, 2004.

Fialko, Y., D. Sandwell, D. Agnew, M. Simons, P. Shearer, and B. Minster, Deformation on nearby faults induced by the 1999 Hector Mine earthquake, *Science*, *297*, 1858–1862, doi:10.1126/science.1074671, 2002.

Flodin, E., and A. Aydin, Faults with asymmetric damage zones in sandstone, valley of fire state park, southern nevada, *J. Struc. Geol.*, *26*(5), 983–988, doi:10.1016/j.jsg.2003.07.009, 2004.

Frankel, A., C. Mueller, T. Barnhard, D. Perkins, E. Leyendecker, N. Dickman, S. Hanson, and M. Hopper, National seismic-hazard maps: documentation June 1996, *Tech. Rep. 96-532*, U.S. Geological Survey, 1996.

Frankel, A., et al., Documentation for the 2002 update of the national seismic hazard maps, *Tech. Rep. 02-420*, U.S. Geological Survey, 2002.

Freiberger, W. F., An approximation method in signal detection, *Quart. J. App. Math.*, *20*, 373–378, 1963.

Ganev, P. N., K. Le, J. Dolan, M. E. Oskin, and A. Elliott, Paleoseismology and geomorphology of the northern Calico fault: testing temporally variable slip rate and earthquake clustering, *AGU Fall Meeting Abstracts*, 2007.

Gibbons, S. J., and F. Ringdal, The detection of low magnitude seismic events using array-based waveform correlation, *Geophys. J. Int.*, *165*, 149–166, 2006.

Gomberg, J., and E. Schweig, Earthquake hazard in the heart of the homeland, U.S. Geological Survey Fact Sheet FS-131-02, 2002.

Got, J. L., J. Frechet, and F. W. Klein, Deep fault plane geometry inferred from multiplet relative relocation beneath the south flank of Kilauea, *J. Geophys. Res.*, *99*, 15,375–15,386, 1994.

Grad, M., Reflected-diffracted waves in frature zone models, *Geophys. J. Int.*, *79*, 353–361, 1984.

Graves, R. W., Simulating seismic wave propagation in 3D elastic media using staggered-grid finite differences, *Bull. Seismol. Soc. Am.*, *86*, 1091–1106, 1996.

Hadley, D., and H. Kanamori, Seismic structure of the transverse ranges, California, *Geol. Soc. Am. Bull.*, *88*, 1469–1478, 1977.

Harris, D. B., A waveform correlation method for identifying quarry explosions, *Bull. Seismol. Soc. Am.*, *81*, 2395–2418, 1991.

Harris, R. A., and S. M. Day, Effects of a low-velocity zone on a dynamic rupture, *Bull. Seismol. Soc. Am.*, *87*, 1267–1280, 1997.

Hauksson, E., Earthquake locations in southern California, written communication, 2010.

Hauksson, E., and P. Shearer, Southern California hypocenter relocation with waveform cross-correlation, Part 1: Results using the double-difference method, *Bull. Seismol. Soc. Am.*, *95*, 896–903, doi:10.1785/0120040167, 2005.

Heidbach, O., M. Tingay, A. Barth, J. Reinecker, D. Kurfeß, and B. Muller, The release 2008 of the World Stress Map, available online at www.world-stress-map.org, 2008.

Helmberger, D. V., Theory and application of synthetic seismograms, in *Earthquakes: Observation, Theory and Interpretation*, pp. 174–222, Soc. Italiana di Fisica, Bolgna, Italy, 1983.

Herrmann, R. B., Surface-wave generation by the south central Illinois earthquake of November 9, 1968, *Bull. Seismol. Soc. Am.*, *63*, 2121–2134, 1973.

Herrmann, R. B., Surface wave focal mechanisms for eastern North American earthquake with tectonic implications, *J. Geophys. Res.*, *84*, 3543–3552, 1979.

Herrmann, R. B., M. Withers, and H. Benz, The April 18, 2008 Illinois earthquake: An ANSS monitoring success, *Seismol. Res. Lett.*, *79*, 830–843, 2008.

Hickman, S., M. Zoback, W. Ellsworth, N. Boness, P. Malin, S. Roecker, and C. Thurber, Structure and properties of the San Andreas Fault in central California: recent results from the SAFOD experiment, *Scientific Drilling*, *1*, doi:10.2204/iodp.sd.s01.39.2007, 2007.

Hole, J. A., R. D. Catchings, K. C. S. Clair, M. J. Rymer, D. A. Okaya, and B. J. Carney, Steep-dip seismic imaging of the shallow San Andreas Fault near Parkfield, *Science*, *294*, 1513–1515, 2001.

Hong, T., and W. Menke, Tomographic investigation of the wear along the San Jacinto fault, southern California, *pepi*, *155*, 236–248, 2006.

Horton, S., S. Ayele, H. Deshon, M. Withers, T. Stigall, G. Pavlis, and M. Hamburger, Aftershocks of the Mw 5.2 April 18, 2008, Mt. Carmel, Illinois Earthquake, The Eastern Section of the Seismological Society of America Meeting Abstract, 2008.

Igel, H., G. Jahnke, and Y. Ben-Zion, Numerical simulation of fault zone guided waves: accuracy and 3-D effects, *Pure Appl. Geophys.*, *159*, 2067–2083, 2002.

ISGS, Structural features in Illinois-1995-Faults: ISGS GIS Database, Illinois State Geological Survey, Champaign, Illinois, 1995.

Jahnke, G., H. Igel, and Y. Ben-Zion, Three-dimensional calculations of fault zone guided wave in various irregular structures, *Geophys. J. Int.*, *151*, 416–426, 2002.

Johnson, A. M., R. W. Fleming, and K. M. Cruikshank, Shear zones formed along long, straight traces of fault zones during the 28 June 1992 Landers, California earthquake, *Bull. Seismol. Soc. Am.*, *84*, 499–510, 1994.

Kanamori, H., Mechanics of earthquakes, *Ann. Rev. Earth Planet. Sci.*, *22*, 207–237, 1994.

Kanamori, H., and E. E. Brodsky, The physics of earthquakes, *Rep. Prog. Phys.*, *67*, 1429–1496, 2004.

Kim, W.-Y., The 18 June 2002 Caborn, Indiana, earthquake: Reactivation of ancient rift in the Wabash Valley seismic zone?, *Bull. Seismol. Soc. Am.*, *93*, 2201–2211, 2003.

Korneev, V. A., R. M. Nadeau, and T. V. McEvilly, Seismological studies at Parkfield IX: Fault-zone imaging using guided wave attenuation, *Bull. Seismol. Soc. Am.*, *93*, 1415–1426, 2003.

Langer, C. J., and G. A. Bollinger, The southeastern Illinois earthquake of 10 June 1987: The later aftershocks, *Bull. Seismol. Soc. Am.*, *81*, 423–445, 1991.

Lees, J., and P. E. Malin, Tomographic images of P-wave velocity variation at Parkfield, California, *J. Geophys. Res.*, *95*, 21,793–21,804, 1990.

Lewis, M. A., Z. G. Peng, Y. Ben-Zion, and F. L. Vernon, Shallow seismic trapping structure in the San Jacinto fault zone near Anza, California, *Geophys. J. Int.*, *162*, 867–881, doi:10.1111/j.1365-246X.2005.02684.x, 2005.

Li, H., Fault zone structures inferred from high frequency waveforms of aftershocks of the 1992 Landers earthquake, Ph.D. thesis, Saint Louis University, Saint Louis, MO, 2005.

Li, H., L. Zhu, and H. Yang, High-resolution structures of the Landers fault zone inferred from aftershock waveform data, *Geophys. J. Int.*, *171*, 1295–1307, doi:10.1111/j.1365-246X.2007.03608.x, 2007.

Li, Y., and P. E. Malin, San Andreas Fault damage at SAFOD viewed with fault-guided waves, *Geophys. Res. Lett.*, *35*(L08304), doi:10.1029/2007GL032924, 2008.

Li, Y. G., and F. L. Vernon, Characterization of the San Jacinto fault zone near Anza, California, by fault zone trapped waves, *J. Geophys. Res.*, *106*, 30,671–30,688, 2001.

Li, Y. G., P. G. Leary, K. Aki, and P. Malin, Seismic trapped modes in the Oroville and San Andreas fault zones, *Science*, *249*, 763–766, 1990.

Li, Y. G., K. Aki, D. Adams, A. Hasemi, and W. H. K. Lee, Seismic guided waves trapped in the fault zone of the Landers, California, earthquake of 1992, *J. Geophys. Res.*, *99*, 11,705–11,722, 1994.

Li, Y. G., F. L. Vernon, and K. Aki, San Jacinto fault-zone guided waves: A discrimination for recently active fault strands near Anza, California, *J. Geophys. Res.*, *102*, 11,689–11,701, 1997.

Li, Y. G., J. E. Vidale, K. Aki, F. Xu, and T. Burdette, Evidence of shallow fault zone strengthening after the 1992 M 7.5 Landers, California, earthquake, *Science*, *279*, 217–219, 1998.

Li, Y. G., J. E. Vidale, K. Aki, and F. Xu, Shallow structure of the Landers fault zone from explosion-generated trapped waves, *J. Geophys. Res.*, *104*, 20,257–20,275, 1999.

Li, Y. G., J. E. Vidale, K. Aki, and F. Xu, Depth-dependent structure of the Landers fault zone using fault zone trapped waves generated by aftershocks, *J. Geophys. Res.*, *105*, 6237–6254, 2000.

Li, Y. G., J. E. Vidale, S. M. Day, D. D. Oglesby, and the SCEC Field Working Team, Study of the 1999 M 7.1 Hector Mine, California, earthquake fault plane by trapped waves, *Bull. Seismol. Soc. Am.*, *92*, 1318–1332, 2002.

Li, Y. G., J. E. Vidale, D. D. Oglesby, S. M. Day, and E. Cochran, Multiple-fault rupture of the M7.1 Hector Mine, California, earthquake from fault zone trapped waves, *J. Geophys. Res.*, *108*, doi:10.1029/2001JB001,456, 2003.

Li, Y. G., J. E. Vidale, and E. S. Cochran, Low-velocity damaged structure of the San Andreas Fault at Parkfield from fault zone trapped waves, *Geophys. Res. Lett.*, *31*, L12S06, doi:10.1029/2003GL019,044, 2004.

Lutz, A. T., R. J. Dorsey, B. A. Housen, and S. U. Janecke, Stratigraphic record of Pleistocene faulting and basin evolution in the Borrego Badlands, San Jacinto fault zone, Southern California, *Geol Soc Am Bull*, *118*(11-12), 1377–1397, doi:10.1130/B25946.1, 2006.

Ma, K., H. Tanaka, and Y. Lin, Fault zone behavior observed from crossing fault 7-level TCDP boreholes seismometers, *EOS, Trans., American. Geophysics Union*, doi:abstract S31A-0198, 2007.

Mackie, R. L., D. W. Livelybrooks, T. R. Madden, and J. C. Larsen, A magnetotelluric investigation of the San Andreas fault at Carrizo Plain California, *Geophys. Res. Lett.*, *24*, 1847–1850, 1997.

Maercklin, N., C. Haberland, T. Ryberg, M. Weber, Y. Bartov, and the DESERT Group, Imaging the Dead Sea Transform with scattered seismic waves, *Geophys. J. Int.*, *158*, 179–186, 2004.

Marshak, S., and T. Paulsen, Midcontinent U.S. fault and fold zones; a legacy of Proterozoic intracratonic extensional tectonism?, *Geology*, *24*, 151–154, 1996.

McBride, J. H., T. G. Hildenbrand, W. J. Stephenson, and C. J. Potter, Interpreting the earthquake source of the Wabash Valley Seismic Zone (Illinois, Indiana, and Kentucky) from seismic-reflection, gravity, and magnetic-intensity data, *Seismol. Res. Lett.*, *73*, 660–686, 2002.

McBride, J. H., H. E. Leetaru, R. A. Bauer, B. E. Tingey, and S. E. A. Schmidt, Deep faulting and structural reactivation beneath the southern Illinois basin, *Precambrian Research*, *157*, 289–313, 2007.

McClusky, S. C., S. C. Bjornstad, B. H. Hager, R. W. King, B. J. Meade, M. M. Miller, F. C. Monastero, and B. J. Souter, Present day kinematics of the Eastern California Shear Zone from a geodetically constrained block model, *Geophys. Res. Lett.*, *28*(17), 3369–3372, 2001.

McGuire, J., and Y. Ben-Zion, High-resolution imaging of the Bear Valley section of the San Andreas fault at seismogenic depths with fault-zone head waves and relocated seismicity, *Geophys. J. Int.*, *163*, 152–164, doi:10.1111/j.1365-246X.2005.02703.x, 2005.

Mueller, K., S. E. Hough, and R. Bilham, Analysing the 1811-1812 New Madrid earthquakes with recent instrumentally recorded aftershocks, *Nature*, *429*, 284–289, 2004.

Munson, P. J., C. A. Munson, and E. C. Pond, Paleoliquefaction evidence for a strong holocene earthquake in south-central Indiana, *Geology*, *23*, 325–328, doi:10.1130/0091-7613(1995)023, 1995.

Munson, P. J., S. F. Obermeier, C. A. Munson, and E. R. Hajic, Liquefaction evidence for Holocene and lastest Pleistocene seismicity in the southern halves of Indiana and Illinois: A preliminary review, *Seismol. Res. Lett.*, *68*, 521–536, 1997.

Nuttli, O. W., Seismicity of the central United States, *Rev. Eng. Geol.*, *4*, 67–94, 1979.

Obermeier, S. F., Liquefaction evidence for strong earthquakes of holocene and lastest pleistocene ages in the states of Indiana and Illinois, USA, *Engineering Geology*, *50*, 227–254, 1998.

Obermeier, S. F., et al., Evidence of strong earthquake shaking in the lower Wabash Valley from prehistoric liquefaction features, *Science*, *251*, 1061–1063, 1991.

Oskin, M., L. Peng, D. Blumentritt, S. Mukhopadhyay, and A. Iriondo, Slip rate of the Calico fault: implications for geologic versus geodetic rate discrepancy in the eastern California shear zone, *J. Geophys. Res.*, *112*(B03402), doi:10.1029/2006JB004451, 2007.

Pavlis, G. L., Appraising earthquake hypocenter location errors: a complete practical approach for single-event locations, *Bull. Seismol. Soc. Am.*, *76*, 1699–1717, 1986.

Pavlis, G. L., Appraising relative earthquake location errors, *Bull. Seismol. Soc. Am.*, *82*, 836–859, 1992.

Peng, Z., Y. Ben-Zion, A. J. Michael, and L. P. Zhu, Quantitative analysis of seismic fault zone waves in the rupture zone of the Landers, 1992, California earthquake: evidence for a shallow trapping structure, *Geophys. J. Int.*, *155*, 1021–1041, 2003.

Petersen, M. D., et al., Documentation for the 2008 update of the United States national seismic hazard maps: U.S. Geological Survery open-file report2008-1128, 61 p, 2008.

Pratt, T. L., E. C. Hauser, and K. D. Nelson, Widespread buried Precambrian layered sequences in the U.S. Mid-Continent evidence for large Proterozoic depositional basins, *Am. Assoc. Petrol. Geologists Bull.*, *76*, 1384–1401, 1992.

Prejean, S., W. Ellsworth, M. Zoback, and F. Waldhauser, Fault structure and kinematics of the Long Valley Caldera region, California, revealed by high-accuracy eartqhauke hypocenters and focal mechanism stress inversions, *J. Geophys. Res.*, *107*, 2355, doi:10.1029/2001JB001,168, 2002.

Rene, R. M., and F. L. Stanonis, Reflection seismic profiling of the Wabash Valley fault system in the Illinois basin, *Tech. Rep. 1538-O*, U.S. Geological Survey, investigations of the New Madrid seismic zone, 1995.

Rockwell, T., C. Loughman, and P. Merifield, Late Quaternary rate of slip along the San Jacinto fault zone near Anza, southern California, *J. Geophys. Res.*, *95*(B6), 8593–8605, 1990.

Rovelli, A., A. Caserta, F. Marra, and V. Ruggiero, Can seismic waves be trapped inside an inactive fault zone? The case study of Nocera Umbra, central Italy, *Bull. Seismol. Soc. Am.*, *92*, 2217–2232, 2002.

Sammis, C. G., A. J. Rosakis, and H. S. Bhat, Effects of off-fault damage on earthquake rupture propagation:experimental studies, *Pure Appl. Geophys.*, *166*, 1629–1648, doi:10.1007/s00024-009-0512-3, 2009.

Sanders, C. O., and H. Kanamori, A seismotectonic analysis of the Anza seismic gap, San Jacinto fault zone, southern California, *J. Geophys. Res.*, *89*, 5873–5890, 1984.

Savage, H. M., and E. Brodsky, Collateral damage: the evolution of fracture distibution in fault damage zones, in review, 2010.

Scholz, C. H., *The mechanics of earthquakes and faulting*, Cambridge Univ. Press, New York, 1990.

Schulz, S. E., and J. P. Evans, Spatial variability in microscopic deformation and composition of the Punchbowl fault, southern California: implications for mechanisms, fluid-rock interaction, and fault morphology, *Tectonophysics*, *295*, 223–244, 1998.

Schulz, S. E., and J. P. Evans, Mesoscopic structure of the Punchbowl fault, southern California and the geologic and Geophys. structure of active strike-slip faults, *J. Struct. Geol.*, *22*, 913–930, 2000.

Scott, J. S., T. G. Masters, and F. L. Vernon, 3-d velocity structure of the San Jacinto fault zone near Anza, California-i.*p* waves, *Geophys. J. Int.*, *119*(2), 611–626, doi:10.1111/j.1365-246X.1994.tb00145.x, 1994.

Sharp, R. J., San jacinto fault zone in the peninsular ranges of southern California, *Geol. Soc. Am. Bull.*, *78*, 705–730, 1967.

Shearer, P., E. Hauksson, and G. Lin, Southern California hypocenter relocation with waveform cross-correlation, Part 2: Results using source-specific station terms and cluster analysis, *Bull. Seismol. Soc. Am.*, *95*, 904–915, doi:10.1785/0120040168, 2005.

Shearer, P. M., Improving local earthquake locations using the L1 norm and waveform cross correlation: Application to the Whittier Narrows, California, aftershock sequence, *J. Geophys. Res.*, *102*, 8269–8283, 1997.

Shelly, D. R., G. C. Beroza, and S. Ide, Non-volcanic tremor and low-frequency earthquake swarms, *Nature*, *446*, 305–307, 2007a.

Shelly, D. R., G. C. Beroza, and S. Ide, Complex evolution of transient slip derived from precise tremor locations in western Shikoku, Japan, *Geochem. Geophys. Geosyst.*, *8*, doi:10.1029/2007GC001,640, 2007b.

Sieh, K., et al., Near-field investigations of the Landers earthquake sequence, April to July 1992, *Science*, *260*, 171–176, 1993.

Simons, M., Y. Fialko, and L. Rivera, Coseismic deformation from the 1999 M_w 7.1 Hector Mine, California, earthquake as infferred from InSAR and GPS observations, *Bull. Seismol. Soc. Am.*, *92*, 1390–1402, doi:10.1785/0120000933, 2002.

Stauder, W., and O. Nuttli, Seismic studies: south-central Illinois earthquake of November 9, 1968, *Bull. Seismol. Soc. Am.*, *60*, 973–981, 1970.

Stierman, D. J., Geophysical and geological evidence for fracturing, water circulation, and chemical alteration in granitic rocks adjacent to major strike-slip faults, *J. Geophys. Res.*, *89*, 5849–5857, 1984.

Sykes, L., and S. Nishenko, Probabilities of occurrence of large plate rupturing earthquakes for the San Andreas, San Jacinto and Imperial faults, California, *J. Geophys. Res.*, *89(B7)*, 5905–5928, 1984.

Tan, Y., and D. V. Helmberger, A new method for determinating small earthquake source parameters using short-period P waves, *Bull. Seismol. Soc. Am.*, *97*, 1176–1195, doi:10.1785/0120060251, 2007.

Taylor, K. B., R. B. Herrmann, M. W. Hamburger, G. L. Pavlis, A. Johnston, C. Langer, and C. Lam, The southeastern Illinois earthquake of 10 June 1987, *Seismol. Res. Lett.*, *60*, 101–110, 1989.

Thatcher, W., J. A. Hileman, and T. C. Hanks, Seismic slip distribution along the San Jacinto fault zone, southern California, and its implications, *Geol. Soc. Am. Bull.*, *86*(8), 1140–1146, 1975.

Thurber, C., S. Roecker, H. Zhang, S. Baher, and W. Ellsworth, Fine-scale structure of the San Andreas fault zone and location of the SAFOD target earthquakes, *Geophys. Res. Lett.*, *31*(L12S02), doi:10.1029/2003GL019398, 2004.

Unsworth, M., G. Egbert, and J. Brooker, High-resolution electromagnetic imaging of the San Andreas fault in central California, *J. Geophys. Res.*, *104*, 1131–1150, 1999.

USGS, U.S. Earthquake Poster, accessed November 10, 2009, http://earthquake.usgs.gov/earthquakes/eqarchives/poster/2008/20080418.php, 2008.

USGS, and ISGS, Quaternary fault and fold database for the United States, accessed May 28, 2008, from USGS web site: http//earthquake.usgs.gov/regional/qfaults, U.S. Geological Survey and Illinois State Geological Survey, 2006.

van Trees, H. L., *Detection, Estimation and Modulation Theory*, 249 pp., John Wiley and Sons, Inc., New York, 1968.

Vidale, J. E., and Y. G. Li, Damage to the shallow Landers fault from the nearby Hector Mine earthquake, *Nature*, *421*, 524–526, 2003.

Waldhauser, F., and W. L. Ellsworth, A double-difference earthquake location algorithm: method and application to the northern Hayward fault, California, *Bull. Seismol. Soc. Am.*, *90*, 1353–1368, 2000.

Waldhauser, F., and W. L. Ellsworth, Fault structure and mechanics of the Hayward fault, California, from double-difference earthquake locations, *J. Geophys. Res.*, *107*, 2054, doi:1029/2001JB000,084, 2002.

Wang, C. Y., F. Rui, Z. Yao, and X. Shi, Gravity anomaly and density structure of the San Andreas fault zone, *Pure Appl. Geophys.*, *124*, 127–140, 1986.

Wang, Q., D. D. Jackson, and Y. Y. Kagan, California earthquakes, 1800-2007: A unified catalog with moment magnitudes, uncertainties, and focal mechanisms, *Seismol. Res. Lett.*, *80 (3)*, 2009.

Whalen, A. D., *Detection of signals in noise*, 167-179 pp., Academic Press, New York, 1971.

Wheeler, R. L., and D. Ravat, Introduction: seismicity, quaternary faulting, and seismic hazard, *Seismol. Res. Lett.*, *73*, 590–596, 2002.

Woolery, E. W., Geophysical and geological evidence of neotectonic deformation along the Hovey Lake Fault, Lower Wabash Valley Fault System, central United States, *Bull. Seismol. Soc. Am.*, *95*, 1193–1201, 2005.

Wu, J., J. A. Hole, J. A. Snoke, and M. G. Imhof, Depth extent of the fault-zone seismic waveguide: effects of increasing velocity with depth, *Geophys. J. Int.*, *173*, 611–622, doi:10.1111/j.1365-246X.2008.03755.x, 2008.

Yang, H., and L. Zhu, Shallow low-velocity zone of the San Jacinto fault from local earthquake waveform modelling, *Geophys. J. Int.*, *183*, 421–432, doi:10.1111/j.1365-246X.2010.04744.x, 2010.

Yang, H., L. Zhu, and R. Chu, Fault-plane determination of the 18 April 2008 Mt. Carmel, Illinois, earthquake by detecting and relocating aftershocks, *Bull. Seismol. Soc. Am.*, *99(6)*, 3413–3420, doi:10.1785/0120090038, 2009.

Zhang, H., C. Thurber, Y. Liu, S. Roecker, R. Lu, and N. Toksoz, High-resolution imaging of San Andreas fault at Parkfield, California, using seismic velocity and anisotropy tomography and seismic interferometry, *Eos Trans. AGU*, *88 (52)*, 2007.

Zhang, H., C. Thurber, and P. Bedrosian, Joint inversion for vp, vs, and vp/vs at SAFOD, Parkfield, California, G^3, *10 (Q11002)*, doi:10.1029/2009GC002709, 2009.

Zhao, P., and Z. Peng, Velocity contrast along the Calaveras fault from analysis of fault zone head waves generated by repeating earthquakes, *Geophys. Res. Lett.*, *35*, doi:10.1029/2007GL031810, 2008.

Zhu, L., and D. V. Helmberger, Advancement in source estimation techniques using broadband regional seismograms, *Bull. Seismol. Soc. Am.*, *86*, 1634–1641, 1996.

Zhu, L., and L. A. Rivera, A note on the dynamic and static displacements from a point source in multilayered media, *Seismol. Res. Lett.*, *148*, 619–627, 2002.

Vita Auctoris

Hongfeng Yang was born in Haicheng, China in October 1978. He graduated from Haicheng high school in 1996 and enrolled in University of Science and Technology of China (USTC). From then on he started to study geophysics. In 2000, he obtained his B.S. degree with a thesis studying experimental measurement on Q of sandstone samples.

Then he attended the graduate school of USTC and continued his study in solid Earth geophysics. His study focused on understanding mechanical properties of rock samples, e.g. sandstone and limestone by various experiments. One part of his master thesis was to measure acoustic velocity of sandstone samples under uniaxial pressure. The challenge was to protect the sensors used to measure acoustic velocity of rock samples because they could not tolerate high pressure. He designed a simple system to hold the sensors and wonderfully finished the task. In his master thesis, he studied viscoelastic properties of sandstone samples and the relationship between acoustic velocities and uniaxial pressure. In 2004, he got his M.S. degree in geophysics.

After he graduated with an M.S. degree, he joined in the Shanghai Siemens Mobile Communication Co. and worked for a few months as a mobile communication maintenance engineer. In 2005, he came to Saint Louis University and started to study seismology.